

An Airborne Remote Sensing Perspective on Cloud and Precipitation Properties  
from Southeast Atlantic Stratocumulus Clouds

By

Andrew Michael Dzambo

A dissertation submitted in partial fulfillment of the requirements for the degree of

Doctor of Philosophy

(Atmospheric and Oceanic Sciences)

at the

UNIVERSITY OF WISCONSIN – MADISON

2020

Date of final oral examination: 03/09/2020

The dissertation is approved by the following members of the Final Oral Committee:

Tristan S. L'Ecuyer, Professor, Atmospheric and Oceanic Sciences

Grant W. Petty, Professor, Atmospheric and Oceanic Sciences

Michael C. Morgan, Professor, Atmospheric and Oceanic Sciences

Daniel J. Vimont, Professor, Atmospheric and Oceanic Sciences

Samuel N. Stechmann, Associate Professor, Mathematics

© Copyright by Andrew Michael Dzambo, 2020  
All Rights Reserved

## Table of Contents

<b>Table of Contents.</b> .....	i
<b>Abstract.</b> .....	v
<b>Forward.</b> .....	vii
<b>List of Figures.</b> .....	xiv
<b>List of Tables.</b> .....	xx
1. Introduction. ....	1
1.1. Stratocumulus cloud formation mechanisms. ....	3
1.2. Precipitation processes in stratocumulus clouds. ....	6
1.3. Aerosol influences on stratocumulus cloud and precipitation properties. ....	7
1.4. Observations and retrievals of cloud and precipitation properties. ....	10
1.4.1. Cloud and precipitation observations. ....	10
1.4.2. Retrieving cloud and precipitation properties. ....	15
1.5. The ORACLES field campaign. ....	20
1.6. Hypotheses. ....	21
2. Datasets. ....	23
2.1. The Advanced Precipitation Radar – 3 <sup>rd</sup> Generation (APR-3). ....	23
2.2. The Research Scanning Polarimeter (RSP). ....	25
2.3. The High Spectral Resolution Lidar - 2nd Generation (HSRL-2). ....	27
2.4. Data availability and sampling considerations. ....	29

3. The observed structure and precipitation characteristics of SE Atlantic stratocumulus from airborne radar during ORACLES 2016-17. ....	35
3.1. Introduction. ....	35
3.2. The APR-3 dataset. ....	38
3.3. Methods. ....	43
3.3.1. Gas attenuation correction. ....	46
3.3.2. Adapted 2C-PRECIP-COLUMN overview. ....	46
3.3.3. 2C-RP algorithm description. ....	47
3.3.4. Estimated inversion strength. ....	50
3.4. Summary of clouds and precipitation. ....	51
3.4.1. Summary of ORACLES 2016. ....	53
3.4.2. Summary of ORACLES 2017. ....	58
3.5. Discussion. ....	62
3.6. Conclusions. ....	68
4. Using retrieved cloud and precipitation properties to assess precipitation susceptibility. ....	71
4.1. Multi-measurement retrievals. ....	71
4.2. Datasets. ....	72
4.3. Algorithm mechanics. ....	73
4.3.1. Forward models. ....	73
4.3.2. Observation and model uncertainties. ....	74

4.3.3. A priori estimate. ....	77
4.3.4. Contribution matrices. ....	78
4.3.5. Other updates to the 2C-RAIN algorithm. ....	79
4.4. Algorithm performance. ....	80
4.4.1. Case study #1: trade cumulus scene. ....	81
4.4.2. Case study #2: drizzling stratocumulus scene. ....	88
4.5. Precipitation susceptibility. ....	94
4.5.1. Gap distance definition. ....	95
4.5.2. Assessment of aerosol effects on cloud and precipitation properties. .....	104
4.6. Conclusions. ....	110
5. The role of evaporation in SE Atlantic stratocumulus clouds on Earth's energy budget. ....	112
5.1. Introduction. ....	112
5.2. Datasets. ....	115
5.2.1. APR-3 radar data. ....	115
5.2.2. 2C-RAIN product. ....	116
5.3. Methods. ....	120
5.4. Campaign evaporation. ....	121
5.5. Conclusions. ....	135
6. Future research. ....	138

7. Conclusions. ....	144
8. Acknowledgements. ....	149
9. Bibliography. ....	150

## Abstract

Stratocumulus (StCu) clouds cover a majority of the Earth's subtropical oceanic basins, and play an important role in the global energy balance. Cloud and precipitation processes in StCu are complex, and aerosol effects add further complexity to the cloud-precipitation-climate paradigm, where these interactions are among the most widely uncertain processes in present-day climate models.

The NASA ObseRvations of Aerosols above CLouds and their intEractionS (ORACLES) field campaign between 2016-18 observed cloud-aerosol-precipitation interactions over the Southeast Atlantic Ocean. One of the 20+ instruments deployed during ORACLES was the Airborne Precipitation Radar – 3rd Generation (APR-3). The APR-3 collected over 18 million profiles during the three deployments. A precipitation retrieval algorithm (called 2C-RAIN) was adapted from the CloudSat 2C-RAIN-PROFILE precipitation retrieval algorithm to meet ORACLES science objectives. The majority of 2C-RAIN precipitation rates were under 0.01 mm/hr (0.25 mm/day). The sampling environments were considerably different in 2016 compared to 2017 and 2018, necessitating further investigation accounting for environmental controls.

Cloud water path (CWP) retrievals were added to the 2C-RAIN algorithm. This retrieval expanded the utility of APR-3 measurements by collocating cloud and precipitation properties (namely CWP and RWP) for the investigation of aerosol indirect effects. This work find typical CWP to RWP ratios on the order of 50:1 to 200:1, implying CWP dominates the total liquid water path (LWP) signal. When

partitioning rain rates with CWP and RWP for aerosol contact and non-contact cases, statistically significant differences are found in stable environments for CWP/RWP but not for retrieved rain rates, likely owing to the 100% and larger uncertainties associated with precipitation rate retrievals.

Finally, evaporation processes are investigated between drizzling virga and surface precipitation. Evaporation rates/fluxes and corresponding latent cooling rates, between surface precipitation and virga, are on the order of 2:1 implying that surface precipitation contributes the most latent cooling to the local environment. Evaporating virga, regardless, cannot be ignored when studying latent heating and cooling. The development of the 2C-RAIN database for ORACLES, and analyses presented here, pave the way for additional observation-based studies in an area where satellite measurements have limited viability.

## Forward

One time during the mid 2000's, my mother grounded me from watching The Weather Channel because I could not stop watching the "Tropical Update" clip they aired at 50 minutes past the hour. It was approximately this time that I knew I wanted to become a meteorologist – a TV or forecasting meteorologist that is. Fast forward to the summer of 2010 during an internship I had, under the guidance of then-Chief Meteorologist Stephen Cropper at WTAE-TV Pittsburgh, I realized how much I enjoyed the field of Meteorology but also that a "better fit" was out there for me. Working with Stephen was an amazing experience: he is a kind, hard-working man, made me feel welcome at the news station, and taught me a lot about the news industry. I will remember this experience as a catalyst for where I am at today, and will forever be grateful and appreciative for what many of my colleagues do in the news industry.

I was, and will never be, the best nor greatest student in the world. My hot-and-cold work ethic and occasional lax attitude toward individual details sometimes curtailed my abilities as a student. I learned, however, how much I love asking questions and how much I enjoy the satisfaction of figuring things out on my own. This passion led me to pursue a Ph.D. in Meteorology/Atmospheric Science, and has driven me to overcome my deepest shortcomings as a student of this field. Coming to this realization is only part of the story: I would not be in this position without the patience, selflessness and love of a number of individuals – both personally and professionally – that I am extremely lucky to have crossed paths with. My focus for

this section will focus on the individuals I have met and gotten to know here in Madison who all have played a role into getting where I am today. I hope to give these individuals the most honest and respectful acknowledgement they deserve.

My first acknowledgement goes to three professors I had at Penn State University as an undergraduate student: Jennifer Plasterr, Doug Hogan, and Eugene Clothiaux. All three of them taught programming courses. The semesters immediately following my internship at WTAE-TV involved taking their programming courses successively, and I learned during this time how much I enjoy computer programming and the satisfaction of seeing my own computer programs work. I found out during this time that many Meteorology/Atmospheric Science graduate students spent a majoring of their non-class time working on computer code to generate plots and analyses. Writing efficient, clean and reusable computer code – quite candidly – saved my ass many times in graduate school. Having great, patient instructors like Jen, Doug and Eugene was a great blessing.

I owe a debt of gratitude to the professors who wrote my letter writers to get into my M.S. and Ph.D. programs: Jenni Evans, Jose Fuentes, Eugene Clothiaux, Anne Thompson, Dave Turner (also my M.S. adviser), and Cameron Homeyer. I am still not quite sure what I did to convince them that I would be capable of graduate work, let alone a Ph.D., but I will always be eternally grateful that they took this initiative on my behalf. I hope I am fortunate enough to pay this forward someday.

My next acknowledgement goes to Craig Oswald and Miguel Bernardez. Craig and Miguel are two of the most dependable men I have met in my life. They are very humble, consistently hard working, and incredibly patient. Beginning January 2017,

I made a hard commitment to invest more time into self-care and physical health, centered on a very rigid workout routine. Both Craig and Miguel rarely ever passed up the opportunity to join me for a workout (even the ones pushing over two hours). This lifestyle change at that point in graduate school, I firmly believe, was the stimulus I needed to truly achieve an optimal work-life balance. I feel far more efficient while working, which allows more time during the week to spend investing in my social life and my relationships with friends and family. Craig and Miguel are stalwarts of consistency and humility, and I believe I am a better person through spending time with both of them over the past few years.

I want to acknowledge three of my officemates: James Anheuser, Juliet Pilewskie and Tobiah Steckel, each of whom I spent nearly a year and a half sharing an office with. I think people fail to realize just how much time you spend with co-workers, and especially those who you literally work right next to. As a result of that, they have seen me on some of my best days and also some of my worst days. For how good they were to me during my time as a student at UW-Madison, I sincerely believe James, Juliet and Tobiah are three of God's finest human creations. They are exceedingly kind, hardworking, focused and truly selfless individuals who I think many (if not all) people experience first-hand knowing them. Working with them made coming into my office very stress-free and fun. I am also grateful that they consistently put up with my (often bad) jokes and puns, and that alone warrants a special acknowledgement.

My next acknowledgements go out to the two individuals who went out of their way to make me feel at home when I first moved to Madison in 2016: Elliot

Shiben and Jessica Taheri. Both reached out to me almost immediately, helping me assimilate to the city and branching my horizons in the city (Capriotti's, Student ticket nights at the Marcus, and numerous home-cooked meals to name a few things). I really believe it takes compassionate, outward going persons to help make any newcomer feel welcome in their new surroundings, and I am forever grateful that they left a forever positive impression on me in feeling at home in Madison. I am blessed and honored to regard both of them as two of my best friends.

In addition to Elliot and Jess, I also want to acknowledge the closest friends I made while here in Madison: Luke Tomas, Megan Lipke, Sam Routh, and Anne Sledd. I think it is no coincidence that, by virtue of Luke/Megan and Sam/Anne being "units", they extended the aforementioned welcoming feeling I've always felt living here in Madison. They've been a tremendous amount of fun, constantly and consistently keeping my sanity in check especially during the times I've needed an emotional support crutch. I know I'll continue to stay close with them beyond my time here in Madison, and I am blessed to have them in my life.

Pete "The HEAT" Pokrandt gets my next acknowledgement. Just about everyone who interacts with Pete appreciates what he does, and he has a very welcoming, calming presence. Pete is the best "IT guy" I've ever met, and the Department of Atmospheric and Oceanic Science at UW-Madison is fortunate and blessed to have Pete. I owe him many beers for all the help he's given me; it has made my life much easier and in many ways expedited the amount of time I needed to finish my Ph.D.

I cannot acknowledge Pete without also acknowledging the rest of the amazing office staff at AOS: Sonja Johnson, Sue Foldy, Kathy Kruger, Debbie Weber, Christi Levenson, Chelsea Dahmen, and Dee Van Ruyven. Whether I needed help or had questions regarding course registration, deadlines, conference travel or general questions, every one of them would literally drop what they were doing to assist me. I am eternally thankful for all of their help.

My next acknowledgement goes to Norm Wood. Norm helped me tremendously at the beginning of my project in 2016, effectively taking the operational CloudSat 2C-RAIN-PROFILE algorithm and making it workable on my desktop/laptop computers. His help literally got my project off the ground, and I would have certainly needed an extra year (if not longer) without his help. Norm is also an incredibly nice guy, and one I have been very fortunate to get to work with.

Despite not having too many classes with AOS faculty outside of my committee, I need to acknowledge them as well for making the AOS department a *very* welcoming place. They collectively embraced numerous group activities including the Welcome Picnics, Pi Day Competition, AOS/SSEC Softball Game & Celebration Picnic, and many other smaller events. When I think of a “family” of academics, the UW-AOS faculty will always be my gold standard.

I was also fortunate to join the ORACLES family of academics, especially the NASA JPL/Caltech APR-3 radar team. Simone Tanelli and Steve Durden, my ORACLES “field bosses”, supervised my two-week visit to JPL during the summer of 2016 and taught me how to run the APR-3 for all three ORACLES experiments. If there was a defining moment during my Ph.D. where my worldview of science

changed, it was the first time I turned on the radar during the 02 Sept. 2016 flight and saw the first “curtains” of radar data streaming across my screen, knowing that data would make it into this dissertation. A tremendous amount of hard work from numerous individuals (engineers, physicists, mathematicians, and programmers) goes into building instruments, all for collecting important geophysical variables. I feel, having this experience, I really understand the *process for realizing* the strengths and limitations of data. Simone and Steve are two of the best at what they do, and are two incredibly likeable, personable guys. I am extremely blessed I got to shadow them during ORACLES.

I also need to acknowledge everyone in my research group, past and present: James Anheuser, Juliet Pilewskie, Elin McIlhattan, Ethan Nelson, Dave Henderson, April Hang, Mark Smalley, Kate Sauter, Alex Matus, Josh Weber, Ashtin Massie, Julia Shates, Anne Sledd, Alyson Douglas, Marian Mateling, Anne Sophie Daloz, and Tobiah Steckel. When I speak of UW-AOS faculty being “family”, my research group is a family of its own. I am grateful for all the interactions and help, big or small, over the years from them, and I hope to continue maintaining friendships and collaborations with all of them for as long as I stay in the field of Atmospheric Sciences.

My penultimate acknowledgement goes out to the professors on my Ph.D. committee: Grant Petty, Michael Morgan, Dan Vimont and Sam Stechmann. I cannot overstate my gratitude and thankfulness for their help in finalizing what I have been dreaming to do for the better part of a decade now. I greatly appreciate their willingness to be a part of this final step for me.

My final acknowledgement goes to Tristan. After the completion of my M.S. degree, I was certain of two things: (1) that I wanted to get a Ph.D., but (2) that I would rather work full time on something else if it was not a Ph.D. project tailored to my interests in clouds and climate science. Not only did I get a project that fit the scope of my interests, I was also blessed to take part as an APR-3 radar operator during all three NASA ORACLES field campaigns covering nearly 12 weeks of my Ph.D. Furthermore, Tristan was more than willing to accommodate my interests outside of ORACLES objectives. One of these projects – a radiosonde based study of gravity waves in the tropical western Pacific Ocean – became a publication in the journal *Atmosphere*, and another project – an assessment of the UW-AOS Climate and Climate Change class – is presently under review in the *Bulletin of the American Meteorological Society*. If I ever land in a position where I get to advise and mentor students, Tristan will definitely be my referral role model. I hope to give anyone who may work for me the flexibility and freedom to explore their interests, while also maintaining the awareness to keep others and myself focused on the goals and tasks at-hand. Thank you, Tristan, for your willingness to serve as my Ph.D. adviser these last 4.5 years.

## List of Figures

- Figure 1.1:** A visible satellite image displaying open-cell (top-left) and closed-cell (bottom-right) stratocumulus clouds from 28 October 2018 over the southeast Atlantic Ocean. This image was downloaded from <https://worldview.earthdata.nasa.gov>. ..... 4
- Figure 1.2:** The ORACLES experiment region (enclosed in a dashed black box) for the 2016-18 campaigns, with São Tomé (STP), Walvis Bay (WVB) and Ascension Island (ASI) marked as green stars. .... 21
- Figure 2.1:** A merged radar-lidar curtain from the 27 Sep. 2018 ORACLES research flight. The top panel shows a 3D representation of the outbound (left) and return (right, offset by 12 degrees latitude for plotting purposes) flight leg curtains. The bottom panel shows the full 2D curtain for the entire flight. .... 28
- Figure 2.2:** The probability of true cloud diameters likely sampled by the NASA P-3 aircraft during ORACLES. Data presented in this figure assume that all “clouds” cover a circular area, where the distance between two points on a circle are calculated using a randomly selected angle. This figure shows the result for one million simulated transects across a cloud’s true diameter. .... 32
- Figure 2.3:** Rain probability estimates for all ORACLES research flights. The rain possible (light green), rain probable (medium green) and rain certain (dark green) assume a maximum column radar reflectivity greater than -15 dBZ, -7.5 dBZ and 0.0 dBZ respectively. These classifications follow the same classification scheme as CloudSat (Haynes et al., 2009) and generated using the 2C-RAIN algorithm generated in Dzambo et al. (2019), both of which are described in Chapter 3. *Adapted from Redemann et al., in prep.* ..... 34
- Figure 3.1:** Sensitivity of the Ku-, Ka- and W-band channels as a function of distance from the aircraft for the ORACLES 2016 mission. The radar performance in 2017 was slightly improved due to upgrades in the processing system. Each set of lines represents a sensitivity range, which varied depending on the configuration of each scan. .... 40

**Figure 3.2:** APR-3 Ku-band (top), Ka-band (middle) and W-band (bottom) reflectivity image from 04 September 2016. This transect began at 12:09:53 UTC and lasted for 9 minutes and 55 seconds. Latitude, longitude and ground distance traveled are all shown as separate x-axes. The colorbar for reflectivity is tuned to W-band (-40 to 20 dBZ) and is the same for all three radar images. Surface backscatter observed at W-band ( $\sigma_0$ ) is overlaid on the Ku-band image as a green line. The bottom-left histogram represents categories based on the 2C-PRECIP-COLUMN algorithm and shows clear-sky/thin cloud (far left), virga (percent of cloudy profiles with > -15 dBZ NOT reaching the surface; left), rain possible (surface reflectivity between -15 and -7.5 dBZ; middle), rain probable (surface reflectivity between -7.5 and 0 dBZ; right) and rain certain (surface reflectivity greater than 0 dBZ; far right). The bottom-middle histogram shows the percentage of altitudes where cloud base and cloud top altitude occur (for all cloudy profiles in this scene). The bottom-right plot shows the flight track for this particular leg. .... 41

**Figure 3.3:** As in Figure 3.2, but with W-band reflectivity (top), attenuation-corrected reflectivity (top-middle), liquid water content (bottom-middle) and surface rain rate and path-integrated attenuation (bottom), where the attenuation-corrected reflectivity, LWC, PIA and surface rain rate are derived from 2C-RP. Rain rate and PIA are plotted only where a valid cloud top above 200 meters is found, the retrievals are *high confidence*, and certain rain is present. .... 50

**Figure 3.4:** APR-3 data collection lines from the 2016 (left) and 2017 (right) campaigns. The (R) denotation represents flights that approximately followed the routine flight track for that campaign year and thus overlap one another. .... 53

**Figure 3.5:** Estimated inversion strength (EIS) along the ORACLES 2016 (red) and 2017 (blue) flight tracks. Each dot (2016) or square (2017) represents the average EIS for the beginning 20% of the flight (i.e. starting when the APR-3 was turned on), middle 20% of the flight and ending 20% (i.e. ending when the APR-3 was turned off) of the flight. .... 54

**Figure 3.6:** Mean daytime estimated inversion strength (EIS) for the ORACLES 2016 (left) and 2017 (right) campaigns. EIS is computed from ERA-I reanalysis data following the methodology outlined in Wood and Bretherton (2006). To assure daytime-only data are used, 12 UTC data are used in this figure. .... 63

**Figure 3.7:** APR-3 W-band estimated cloud top altitudes (2016, A; 2017, B), cloud base altitudes (2016, C; 2017, D) and cloud depths (2016, E; 2017, F) in the SE Atlantic basin. Cloud depth is the difference between cloud top altitude and cloud base altitude, with cloud base altitude assumed to be the lowest altitude in the cloud with a valid radar reflectivity measurement. Data are binned according to 1x1 degree latitude/longitude boxes. .... 65

**Figure 3.8:** Normalized frequency by altitude diagram of attenuation-corrected W-band reflectivity measurements for ORACLES 2016 (left) and 2017 (right). .... 66

**Figure 3.9:** ORACLES 2016 and 2017 campaign cloud-only (gray), virga-only (light green) and drizzling/raining profiles (dark green) for *all* cloudy sky profiles (top panel) where the aircraft was flying at nadir. Retrieved rainfall rates for all drizzling or raining profiles for 2016 (green) and 2017 (blue) are binned by intensity (bottom panel). CLOUD represents the fraction of all cloudy sky profiles that did not have virga nor precipitation, and VIRGA represents the fraction of all cloudy profiles with a maximum reflectivity of -15 dBZ or greater anywhere in the column. .... 69

**Figure 4.1:** 2C-RAIN retrieval from a heavily precipitating trade cumulus cloud observed by the APR-3 (top) on 12 Oct. 2018. The model-corrected reflectivity (top-middle) for this scene, along with retrieved RWC (top-center) and rainfall profile (bottom-center), are also shown. The bottom two panels show retrieved water paths (cloud, rain and total; square markers), rainfall rates (surface or evaporation-corrected rainfall rate and near-surface rainfall rate; star markers), attenuation ('PC' or observed and '2C-RAIN' or modeled; square markers) and optical depths (cloud, rain and total; star markers). No quality control flags are applied to the data shown in this figure. .... 83

**Figure 4.2:** Mean contribution matrix (or C-matrix) calculations relative to cloud height for the radar profiles shown in Fig. 4.1. The C-matrix for each retrieved rainfall rate, as well as CWP, was calculated according to Eq. 4.13. Individual C-matrix profiles are normalized to the full length of the reflectivity profile (i.e. 0 = radar echo base, 1 = radar echo top). Data below the dashed line indicates a C-matrix calculation for both the surface (i.e. corrected for evaporation) and near-surface precipitation rates and is exactly the same for both precipitation rate quantities. In the bottom panel, the contributions from reflectivity, optical depth, PIA and a priori uncertainties are respectively shown in black, blue, gray and orange. .... 86

**Figure 4.3:** As in Fig. 4.2, but for profiles where the a priori constraint contributed minimal uncertainty (solid line) and profiles where the PIA contributed minimal uncertainty (dashed lines). ..... 87

**Figure 4.4:** 2C-RAIN retrieval from lightly drizzling stratocumulus cloud observed by the APR-3 (top) on 24 Aug. 2017. The model-corrected reflectivity (top-middle) for this scene, along with retrieved RWC (top-center) and rainfall profile (bottom-center), are also shown. The bottom two panels show retrieved water paths (cloud, rain and total; square markers), rainfall rates (surface or evaporation-corrected rainfall rate and near-surface rainfall rate; star markers), attenuation ('PC' or observed and '2C-RAIN' or modeled; square markers) and optical depths (cloud, rain and total; star markers). No quality control flags are applied to the data shown in this figure. The lower LWP and optical depth values around minute 10.5 correspond to a short period where the RSP was not operating. .... 89

**Figure 4.5:** Mean contribution matrix (or C-matrix) calculations relative to cloud height for the radar profiles shown in Fig. 4.4. The C-matrix for each retrieved rainfall rate, as well as CWP, was calculated according to Eq. 4.13. Individual C-matrix profiles are normalized to the full length of the reflectivity profile (i.e. 0 = radar echo base, 1 = radar echo top). Data below the dashed line indicates a C-matrix calculation for both the surface (i.e. corrected for evaporation) and near-surface precipitation rates and is exactly the same for both precipitation rate quantities. In the bottom panel, the contributions from reflectivity, optical depth, PIA and a priori uncertainties are respectively shown in black, blue, gray and orange. .... 91

**Figure 4.6:** As in Fig. 4.5, but for profiles where the a priori constraint contributed minimal uncertainty (solid line) and profiles where the PIA contributed minimal uncertainty (dashed lines). ..... 94

**Figure 4.7:** A full HSRL-2 curtain from the 15 Aug. 2017 research flight. The top panel shows the cloud-screened aerosol backscatter coefficient in  $\text{Mm}^{-1} \text{Sr}^{-1}$ , which proxies both the mass and volume of aerosol at a given bin and has a resolution of 15 m. The middle panel shows the aerosol classification for this curtain following Burton et al. (2012), and the bottom panel shows the above cloud aerosol optical thickness and has a range resolution of 315 m. Data in the top and bottom panels are from the 532 nm channel. Black lines indicate the cloud top altitude. .... 97

**Figure 4.8:** As in Fig. 4.7, but for the 15 Aug. 2017 research flight. .... 100

- Figure 4.9:** The average aerosol above-cloud optical depth (left) and the change in AOD across two range bins above cloud ( $\sim 630$  m, or two HSRL-2 range bins; right) for the 15 Aug. 2017 research flight. A negative slope corresponds to *increasing* AOD from the HSRL-2 toward the cloud. .... 102
- Figure 4.10:** As in Fig. 4.9 but for the 17 Oct. 2018 research flight. .... 103
- Figure 4.11:** Box-and-whisker plots of CWP to RWP ratio for the ORACLES field campaign. The middle and right box-and-whisker plots correspond to light rain and light drizzle respectively. .... 105
- Figure 4.12:** Retrieved RWP, CWP and maximum column precipitation rate (left to right) as functions of SST (top) and EIS (bottom). The dark lines represent 1<sup>st</sup> order lines of best fit. Pearson correlation coefficients are given in the title of each subplot. Colored pixels represent data where at least 30 points are binned. Each subplot is normalized to the number of points in the entire plot, with the red/gray pixels corresponding to values near 1. .... 107
- Figure 5.1:** An APR-3/2C-RAIN example from the 31 Aug. 2017 research flight, with this particular radar scan beginning at 12:56 UTC and showing uncorrected W-band reflectivity (top), modeled hydrometeor attenuation (top-middle), corrected W-band reflectivity (middle), profiles of rainfall rate (bottom-middle) and rainfall rates representing surface (green) and profile maximum (violet) from nadir APR-3 and 2C-RAIN data. For this case, scanning W-band data were used, which had approximately 10 dB less sensitivity (e.g. minimum detectable signal was about -20 dB). .... 119
- Figure 5.2:** Cumulative distributions of evaporation rates derived from virga and surface precipitation. Results are partitioned by low EIS (i.e.  $EIS < 0$  K) and high EIS (i.e.  $EIS > 2$  K). .... 123
- Figure 5.3:** Median evaporation rate as a function latitude and longitude (in 1 degree bins) for the 2016 (top-left), 2017 (top-right), 2018 (bottom-left) and entire (bottom-right) ORACLES campaign. .... 126
- Figure 5.4:** Median evaporation rate as a function of estimated inversion strength (EIS; x-axis) and sea surface temperature (SST; y-axis). EIS and SST bins are each binned every 1 K. .... 128

**Figure 5.5:** Estimated areal coverage of the SE Atlantic StCu cloud deck on 22 Oct. 2018 (top) and 15 Aug. 2018 (bottom). Both images and estimates were provided courtesy of <https://worldview.earthdata.nasa.gov>. ..... 131

**Figure 5.6:** Estimated surface precipitation fraction as a function of EIS. .... 134

## List of Tables

<b>Table 2.1:</b> Description of data availability for the ORACLES 2016-18 field campaigns. The 27 Sep. 2016 flight was classified a “transit flight” but is included in this analysis because the transit flight took place entirely in the experiment area between Walvis Bay, Namibia and Ascension Island and is denoted by a single asterisk (*). For the 2016 experiment, (**) denotes where instrument data is available, but only from the NASA ER-2 aircraft. No ER-2 data is used. ....	31
<b>Table 3.1:</b> A list of variables required to run the adapted 2C-RAIN-PROFILE algorithm for ORACLES APR-3 data. ....	44
<b>Table 3.2:</b> List of variables in the Level 2 precipitation retrieval dataset. ....	45
<b>Table 3.3:</b> Daily rainfall statistics for ORACLES 2016. The number of cloudy profiles refers to any <i>valid</i> profile where the aircraft was flying a level leg (i.e. a pitch, drift and roll angle of less than 3 degrees) and detected a valid reflectivity profile after noise removal (described in the text). A rejected profile refers to any radar profile that either saw clear skies or was collected during a non-level flight leg. The cloud fraction column includes only APR-3 W-band nadir data. The percent of cloudy profiles with virga or surface rainfall account for <i>valid</i> cloudy-sky profiles only. The five columns from the right account for only profiles where surface rainfall was present. ....	55
<b>Table 4.1:</b> Summary of median CWP, RWP and maximum column precipitation rate for contact and non-contact scenarios, partitioned by stable (EIS > 2 K, or EIS > 4 K in parenthesis) or unstable (EIS < 0 K) environmental conditions. ....	108
<b>Table 5.1:</b> Summary of median campaign evaporation statistics from surface precipitation and virga, partitioned by unstable (EIS < 0 K) and stable (EIS > 2 K) regimes. Positive evaporation fluxes imply a latent cooling. ....	124

## Chapter 1: Introduction

Stratocumulus clouds (StCu hereafter) are one of the most common cloud types found on Earth, covering approximately 20% of the Earth's surface [Warren et al., 2007; Wood 2012] albeit primarily over the world's eastern subtropical oceanic basins [Wood and Hartmann, 2006]. StCu cloud coverage remains a heavily researched topic due to their observational limitations and difficulty to represent in process-level, weather and climate models [e.g. Stevens and Feingold, 2009; Wood 2012; Witte et al., 2017, Witte et al., 2019]. Present day climate models owe much of their lingering uncertainty to cloud-climate feedbacks [Bony and Dufresne, 2005] and especially in situations where atmospheric aerosols further convolute these feedbacks [Zhang et al., 2016]. Precipitation processes add yet another level of complexity to this problem [e.g. Stevens and Feingold, 2009] owing to the fact that precipitation modifies cloud and aerosol properties/distributions within StCu. Aerosol effects on clouds, however, have been theorized to modify precipitation frequency and intensity in StCu [e.g. Albrecht 1989; Wood 2012]. Summarizing these processes should lead one to quickly fathom why cloud-aerosol-precipitation interactions lead to the greatest uncertainties in climate models [IPCC, 2014].

Clouds, aerosols and precipitation synchronously work together to modify the local latent heating (or cooling) of a region. Evaporating drizzle is ubiquitous in every field campaign focusing on shallow marine boundary layer (MBL) clouds [Bretherton et al., 2004; Wood et al., 2011; Zuidema et al., 2016; Redemann et al., *in prep*]. Latent cooling from evaporating drizzle can modify the turbulence structure

of the MBL, which helps control cloud thickness [Bretherton et al., 2004] and variability in LWP across a stratocumulus deck [Matheou 2018]. Yang et al. (2018) found that the frequency of drizzle in North Atlantic StCu clouds occurred in 83% of profiles, but only 31% of those data contained surface precipitation, implying a potentially large amount of sub-cloud evaporative cooling. The vast expanse of StCu cloud cover in the subtropical ocean basins and the frequency of drizzle in these clouds might suggest a large global evaporative (latent) cooling effect, however, such a metric is difficult to formulate due to the observational difficulties of MBL precipitation structure. Only recently have long term, observational-based estimates of latent heating become possible [Nelson et al., 2016; Nelson and L'Ecuyer, 2018]. Quantifying latent heating in a place such as the SE Atlantic becomes further convoluted due to the difficulty of disentangling aerosol effects.

The recent Observations of Aerosols above Clouds and their Interactions (ORACLES) field campaign collected an unprecedented dataset of cloud, aerosol, radiation and precipitation properties, which recently enabled new and ongoing process-level studies of cloud-aerosol-precipitation interactions. The focus of this dissertation is twofold: to develop a combined cloud and precipitation retrieval dataset for the study of cloud-aerosol-precipitation interactions, and to use this dataset to estimate the role of evaporation in the SE Atlantic Ocean on the global climate system. This chapter discusses our present-day understanding of StCu cloud and precipitation processes, aerosol effects, environmental and meteorological controls, observational capabilities (with a focus on airborne and spaceborne

remote sensing), cloud and precipitation retrieval algorithms, and finally, a synthesis of this information that guides the studies presented in this dissertation.

### **1.1: Stratocumulus cloud formation mechanisms**

Stratocumulus clouds ubiquitously form in the eastern oceanic basins by a process called mesoscale cellular convection [Wood and Hartmann, 2006; Zhou and Bretherton, 2019]. StCu are typically characterized as “open-cell” or “closed-cell”, each of which are distinct both in the way they appear in satellite imagery as well as the meteorological conditions by which they form. In the eastern oceanic basins, coastal upwelling results in low sea-surface temperatures (SSTs). Low SSTs, coupled with subsidence aloft, creates environmental conditions conducive for shallow marine boundary layers (MBLs) to form. Clouds forming in these shallow MBLs are often closed-cell. Closed-cell StCu, on average, have a convective depth of  $\sim 1.3$  km which is nearly 1 km less than the typical convective depth of open-cell StCu [Agee and Dowell, 1974]. Warm air advection near the surface is also characteristic for closed-cell StCu. Although near-surface warm air advection would favor thermodynamic instability, very strong thermodynamic inversions aloft generated by subsiding air ultimately inhibit vertical cloud growth. This forces rising air to move horizontally, giving StCu the “sheet-like” structure typically seen in satellite imagery (Fig. 1.1). Klein and Hartmann (1993) found that a  $1^{\circ}\text{C}$  increase in lower tropospheric stability corresponded to a 6% increase in fractional area coverage of StCu. Likewise, increasing SSTs within these environments also lead to increased StCu cloud fraction [Pincus et al., 1997].

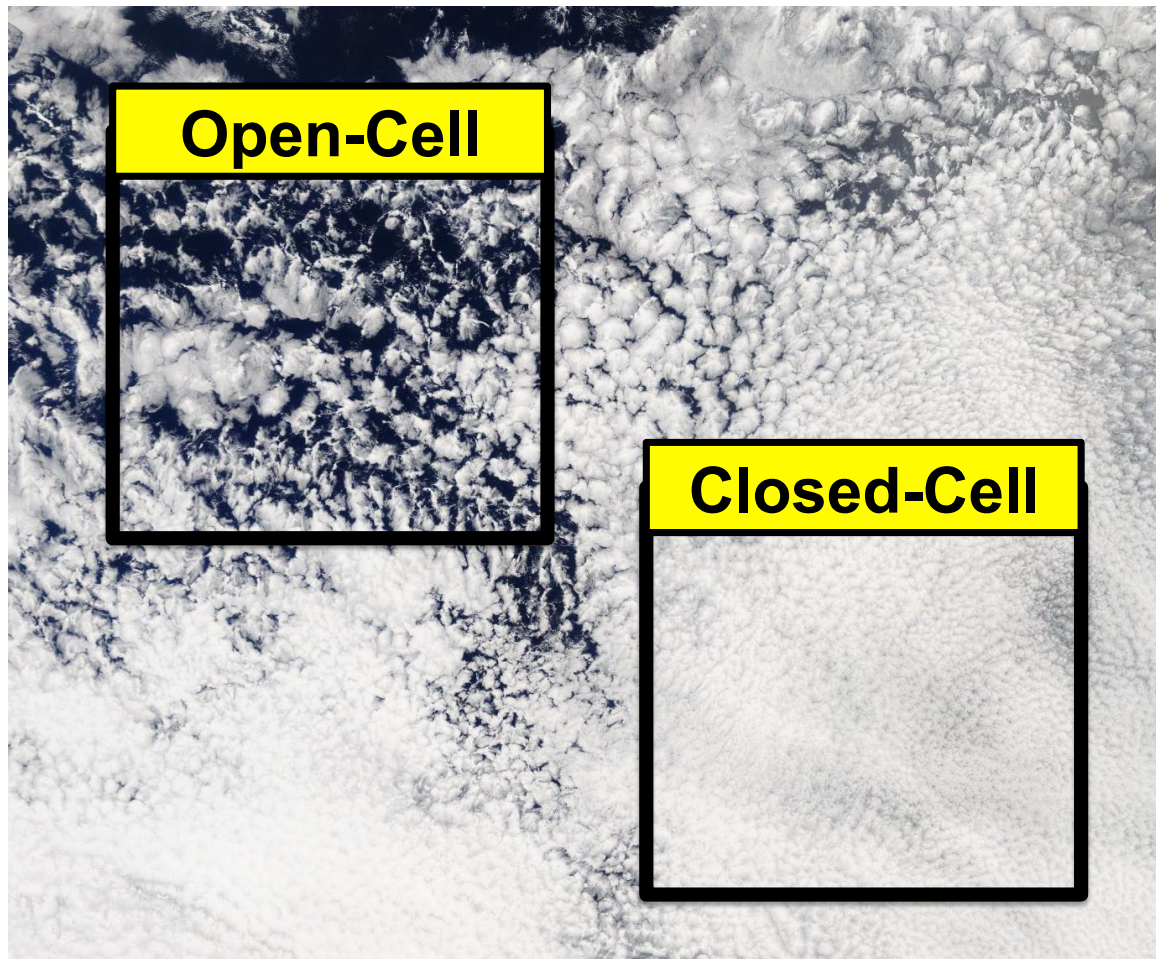


**Figure 1.1:** A visible satellite image displaying open-cell (top-left) and closed-cell (bottom-right) stratocumulus clouds from 28 October 2018 over the southeast Atlantic Ocean. This image was downloaded from <https://worldview.earthdata.nasa.gov>.

StCu tend to remain well organized in shallow MBLs, but as a MBL deepens, StCu gradually transition from closed-cell to open-cell convection. Open-cell StCu, in addition to being convectively deeper than closed-cell StCu, are especially common behind cold-fronts or within cyclonic-rotating synoptic scale weather systems. The deeper MBL and weaker inversions aloft in open-cell StCu result in a scenario where

cloud cover forms at the edges of these convective cells rather than directly overtop of them, giving these StCu a truly “open” character on satellite images. Eventually, these StCu transition entirely into disorganized cellular convection. This mechanism, often referred to as the stratocumulus-to-cumulus (StCu-to-Cu) transition [Sandu and Stevens, 2011; Mohrmann et al., 2019; Sarkar et al., 2020], occurs when StCu transported away from the coasts by trade winds toward the equator into deeper MBLs. Rapidly changing SSTs can also facilitate the StCu-to-Cu transition [Pincus et al., 1997]. The StCu-to-Cu transition is finalized when StCu decouple from the surface, resulting in trade Cu.

Subsidence greatly aids in the maintenance of the Southeast Atlantic StCu deck. Adebisi and Zuidema (2018) showed that increasing subsidence increases low cloud fraction over this region, whereas subsidence reduces cloud coverage elsewhere (i.e. in regions where cumulus are more likely). This is largely the result of the fact that marine boundary layer (MBL) clouds simply do not protrude into the free troposphere. Southeast Atlantic StCu are affected by another co-occurring process: the entrainment of free tropospheric air into the MBL. Entraining dry free-tropospheric air into the MBL initially dries the cloud from the bottom of the cloud upwards, although cloud base heights change little [Deardorff 1980] presumably due to the fact that dry air can help first evaporate smaller drops, which are typical near the cloud top. A stronger inversion above a stratocumulus cloud layer would help extend their lifetime by inhibiting the entrainment of dry air, since buoyant air parcels cannot deeply penetrate into the free troposphere. Having a strong understanding of environmental processes and their effect on StCu is becoming

increasingly important, since the characteristic mesoscale structure of StCu is likely to change as Earth's climate changes [Bony et al., 2020]. Subsidence and entrainment also play a critical role in supplying aerosols into the MBL; these processes will be described in greater detail later in this chapter.

## **1.2: Precipitation Processes in Stratocumulus Clouds**

Precipitation processes within stratocumulus clouds play an important role in an StCu cloud's lifetime. Available liquid water path (LWP), or the vertically integrated liquid water content (LWC) in a cloud, is first sequestered onto hygroscopic cloud condensation nuclei (CCN) forming cloud droplets. For droplet sizes less than  $\sim 40 \mu\text{m}$ , further droplet growth via diffusion (i.e. condensational growth) of water vapor occurs. From this point, the primary drop growth mode switches from water vapor diffusion to collision-coalescence. Many studies have pointed to  $\sim 40 \mu\text{m}$  as a critical value at which collision-coalescence (or autoconversion) can more efficiently grow cloud droplets into drizzle droplets [Wood 2012; Glienke et al., 2017]. Autoconversion increases with increasing cloud LWP [Feingold et al., 1996b].

Understanding the global distribution of precipitation, including frequency and magnitude in the horizontal and vertical, is necessary to understand the global energy budget. Convective and stratiform rain (for example) develop from different meteorological and environmental drivers, contain varying drop size distributions, distribute incoming shortwave radiation differently, and contain differing latent

heating structures [e.g. Schumacher and Houze, 2003; Nelson et al., 2016; Nuijens et al., 2017; Nelson and L'Ecuyer, 2018].

The representation of droplet growth and drizzle processes in global climate models has proven challenging. Several studies have found that warm clouds precipitate too frequently and too often [Stephens et al., 2010; Trenberth 2011; Kay et al., 2018]. It has been suggested that this could be due to a misrepresentation of precipitation efficiency for a given liquid water path [Jing et al., 2017]. Precipitating StCu clouds could also act as a pathway toward cleansing the PBL of aerosol and, if the StCu deck is primarily open-cell (i.e. forming in less-stable environments) as opposed to closed-cell (i.e. typically forming in regions of strong subsidence), these precipitating cells could suppress new cloud formation later in the diurnal cycle due to significant aerosol depletion [Wang et al., 2010]. It is clear that precipitation processes play a critical role in StCu cloud morphology and lifetime, yet deconvolving these processes from aerosol effects and resultant radiative effects remains open for scientific debate [Stevens and Feingold, 2009]. This enigma manifests itself across nearly every climate model, where the liquid water path (LWP) response to aerosol loading and dynamical regimes varies widely from model-to-model [Zhang et al., 2016].

### **1.3: Aerosol Influences on StCu Cloud and Precipitation Properties**

The interaction between clouds and aerosols remains one of the most poorly constrained processes in climate models [Lohmann and Lesins, 2002; Zuidema et al., 2016]. The aerosol indirect effect, first recognized by Twomey (1977), stipulates

that increasing aerosol concentrations in clouds act as CCN that affect cloud albedo, cloud lifetime, precipitation processes and cloud droplet number concentrations. There are two indirect effects: the cloud albedo effect (or the Twomey Effect), and the cloud lifetime effect. The first indirect effect requires that, for a fixed liquid water path, increasing CCN reduce the size of cloud droplets thereby increasing the cloud's albedo. For the second indirect effect, increasing the number of small cloud droplets or shifting the cloud drop size distribution toward smaller droplets acts to suppress drizzle, increasing the cloud's lifetime [Albrecht 1987]. Many studies since the Albrecht (1987) study have presented evidence for aerosol-induced precipitation suppression across many regions of the world [e.g. Saleeby et al., 2010; Douglas and L'Ecuyer, 2019]. Measuring the second indirect effect becomes complicated by the idea that, in environments of lower environmental stability, smaller drops evaporate more quickly thus acting to reduce the cloud's lifetime [Wood 2007]. Measuring the second indirect effect also becomes further complicated by cloud thickness [Wood 2007].

As mentioned in Section 1.1, subsidence and entrainment represent the two most important dynamical processes by which aerosols reach the MBL. Large (i.e. coarse mode) aerosols generally subside more quickly than small (i.e. fine mode; less than  $\sim 0.1$  microns in diameter) aerosols. Stronger subsidence will lead to increased aerosol concentrations near the MBL over time. The amount of aerosol in the free troposphere arriving near the MBL becomes moot if no entrainment occurs. For this reason, it is unsurprising that the amount of free tropospheric aerosol poorly correlates with the amount of aerosol in the MBL [Diamond et al., 2018].

Increased entrainment rates, when in contact with an aerosol layer, results in increased aerosol number concentrations in the MBL [Diamond et al., 2018]. The absorption of shortwave radiation creates localized heating, which could reduce cloud LWP (if in cloud) or enhance cloud LWP (if above cloud); this process is known as the aerosol semi-direct effect [Johnson et al., 2004]. Cloud fraction is particularly sensitive to the altitude of the absorbing aerosol, where decreased cloud fraction is observed when the aerosol layer is closer to the MBL [Das et al., 2020]. Quantifying the effects of increased aerosol on cloud albedo and lifetime, despite this knowledge, remains limited even though the majority of evidence suggests this to be true. A study by Small et al. (2009) suggested that, for non-precipitating cumulus cloud, aerosol loading could actually *decrease* a cloud's lifetime due to an evaporation/entrainment feedback. Different aerosol species could also affect cloud lifetime. For example, sea salt mixed into the lower MBL has been linked to increased precipitation and decreased cloud lifetime whereas pollution aerosol above the MBL could lead to decreased precipitation rates and increased cloud lifetime [L'Ecuyer et al., 2009]. Precipitation processes are perhaps the "key that links" the aforementioned dynamical processes to the amount of aerosol and cloud matter ultimately describing the aerosol indirect effect.

In addition to aerosol effects on StCu adding considerable uncertainty to future climate model projections, StCu sensitivity to changing atmospheric conditions in these same climate model projections may be the primary source of cloud feedback uncertainty [Bony and Dufresne, 2005; Zhang et al., 2016]. This fact alone necessitates controlling for environmental conditions to lend confidence in

any study examining aerosol-cloud-precipitation interactions [Douglas and L'Ecuyer, 2019; Dzambo et al., 2019], or when possible, the co-variability of aerosol and environmental effects on StCu [Mülmenstädt and Feingold, 2018].

#### **1.4: Observations and Retrievals of Cloud and Precipitation Properties**

Seemingly countless numbers of instruments and techniques have been developed over the past century to aid our ability to measure and quantify cloud and precipitation processes. Widger and Touart (1957) were among the first to theorize that satellites could leaven the atmospheric sciences to countless significant advances, and suggested that airborne field missions would “simulate” the expected data from a satellite. For a climate scientist or a general forecaster, satellites provide data and information about regions where observations are otherwise sparse or non-existent. Fast forward to the year 2020, scientists across the globe can now study weather and climate processes in Earth’s most remote locations. Our collective knowledge of weather and climate processes across the global subtropical oceans has benefitted tremendously with the advent of satellite measurements, and numerous field campaigns have supplemented our process-level knowledge that guides planning for future satellite missions. The following two subsections narrow this focus down to airborne and spaceborne observations (1.4.1) and cloud/rainfall retrieval techniques and algorithms (1.4.2).

##### *1.4.1: Cloud and Precipitation Observations*

Explorer 6, the brainchild of the legendary Dr. Verner Suomi, was the first satellite to collect measurements of Earth's radiation budget and laid the groundwork for spaceborne remote sensing of Earth's weather and climate systems [Vaughan and Johnson, 1994]. The Television Infrared Observation Satellite (TIROS-1) collected the first low-earth orbit spaceborne images of Earth's weather systems (an earlier weather satellite, Vanguard II, was launched on 17 Feb. 1959 but never successfully captured any images). Satellite-based weather and climate developed over the next several decades, gradually resulting in a long-term collection of global cloud properties (e.g. cloud fraction, albedo, and structure). Spaceborne lidars such as CALIPSO and CALIOP offer the ability to detect clouds and aerosols from space. Their high spatial resolution has enabled improved global estimates of cloud fraction and horizontal cloud gaps [Kiemle et al., 2015], helping to bridge observational gaps in cloud coverage where high frequency radar lacks sensitivity to optically thin clouds. However, lidars quickly attenuate in atmospheric layers containing modest liquid water content thus rendering them "blind" through and below clouds. Precipitation measurements, to this point, were nearly impossible to observe with these instruments given their lack of sensitivity [e.g. Stenz et al., 2016]. Any precipitation estimate from passive satellite remote sensing instrumentation often required an inversion technique (i.e. retrieval; see next subsection) with several approximations and still resulted in estimates with very large uncertainties. The largest precipitation uncertainties, unsurprisingly, resulted from scenes containing drizzle or light rain [e.g. Berg et al., 2010].

The TRMM Precipitation Radar (TRMM PR), a dual frequency Ku-band and Ka-band radar, was developed to provide continuous coverage of rainfall in the tropics [Schumacher and Houze, 2003]. The TRMM PR's sensitivity of 17 dBZ (i.e. rain rates greater than a few mm/hr), however, meant most stratiform precipitation would go undetected. The advent of the CloudSat Cloud Profiling Radar (CPR), a W-band (94 GHz) radar, dramatically improved our ability to simultaneously measure clouds and light precipitation [Tanelli et al., 2008]. Both TRMM PR and CloudSat CPR data contain some uncertainty due to the effects of non-uniform beamfilling: or contamination of a measurement due to multiple targets-of-interest "filling" a scanning volume [Durdin et al., 1998]. Non-uniform beamfilling is purely a consequence of the long distance between the satellite and atmosphere, resulting in a large scanning volume (or put another way, the radar "sees" a large horizontal swath). The largest uncertainties from non-uniform beamfilling result from inhomogeneous rainfall, such as scattered trade cumulus or deep tropical convection [Tanelli et al., 2004]. Multiple scattering (MS hereafter) adds additional uncertainty to the observed reflectivity from these spaceborne radars. Deep convection, on top of introducing non-uniform beamfilling uncertainties, almost always results in MS of a radar pulse due to large hydrometeors and high ice water content aloft [Battaglia et al., 2011]. MS can occur to a lesser degree in precipitating trade cumulus.

CloudSat measurements have improved our understanding of StCu clouds and warm rain processes [Lebsock et al, 2008; Haynes et al., 2009; L'Ecuyer et al, 2009; Sorooshian et al, 2009; Lebsock and L'Ecuyer, 2011]. With a sensitivity of

around -29 dBZ, CloudSat can observe cloud and light precipitation events previously missed by lower-frequency precipitation radars. For example, Berg et al. (2010) studied retrieved precipitable water content between the CloudSat CPR and TRMM PR and found that the TRMM PR missed an estimated 10% of all precipitable (rain) water content. This estimate could be higher, since CloudSat's "blind zone" below ~750 meters and its 240 meter range resolution introduce limitations across the world's subtropical oceanic basins where StCu clouds can be much thinner than 240 meters in depth and have cloud top altitudes below 1 km. In such regimes, airborne remote sensing and in-situ observations remain essential for process studies and validating satellite climatologies, especially over the remote ocean regions where ground-based validation studies are not possible.

While satellite-based measurements of clouds and precipitation offer the most spatial and temporal coverage, field experiments became increasingly necessary to validate these spaceborne measurements and their resulting retrieval products. Houze et al. (1981) was among the first studies to show that airborne radar could closely match land-based radars at the same frequency. This study, using data from the International Monsoon Experiment (MONEX), found that a land-based and airborne 5 cm radar measurements agreed to within 1-2 dB when simultaneously sampling the same volume. The First ISCCP Regional Experiment (FIRE) campaign was among the earliest to collect observations of both cirrus and marine stratocumulus cloud systems [Cox et al., 1987]. Though no radars were deployed during FIRE, radiometric and lidar datasets were used to characterize and validate cloud properties [Starr 1987] and have been staples to many cloud-focused

field experiments since then. The Dynamics and Chemistry of the Marine Stratocumulus (DYCOMS) experiments (Lenschow et al., 1988; Stevens et al., 2003) brought new insights on marine stratocumulus life cycle in the East Pacific Ocean near California, while also studying how atmospheric ozone interacts with these clouds. The Rain in Shallow Cumulus Over the Ocean (RICO) experiment [Rauber et al., 2007] provided one of the most comprehensive datasets on warm rain processes. The continuous ground and ship-based measurements, combined with measurements from 57 research flights, have aided in the validation of cloud processes and cloud fraction [vanZanten et al., 2011] as well as sensitivity to rain microphysics [Abel and Shipway, 2007] in large eddy model simulations. These early studies provided an important framework for future airborne-based validation studies of cloud and/or aerosol studies.

StCu clouds, particularly those observed in the SE Atlantic, are usually homogeneous but especially challenging to observe for a number of reasons. Modern passive radiometers such as the Moderate Resolution Imaging Spectroradiometer (MODIS) or Geostationary Operational Environmental Satellite (GOES) can accurately measure cloud fraction and other macrophysical properties, yet (again) require numerous assumptions for precipitation rate retrievals that remain biased [Stenz et al., 2016]. Multi-layered clouds, cloud inhomogeneity and overlying aerosol are all obstacles that complicate StCu cloud and precipitation observations. Precipitation rate products utilizing satellite microwave and infrared data have improved [Salio et al., 2015], but the precipitation retrieval quality is regime dependent [e.g. Berg et al., 2006] and these products do not provide the

sensitivity to drizzle and rain required to study precipitation and microphysical processes [e.g. Berg et al., 2010]. This is especially true for precipitation techniques relying on microwave emission (brightness temperature) data because inferred precipitation rates are derived from data sensitive to both cloud and precipitable liquid water [Lebsock et al., 2011], and partitioning the signal from cloud and precipitable water requires an assumption based on (for example) climatological data [Hilburn and Wentz, 2008]. Other techniques bridging passive radiometry with airborne in-situ measurements have to assume spatial homogeneity for any meaningful comparison [e.g. Glienke et al., 2017] and account for variable spatial averaging between in-situ airborne and satellite observations [Sorooshian et al., 2010].

Airborne radar offers a critical bridge toward mitigating uncertainties in our knowledge of precipitation. High frequency W-band (94-95 GHz), Ka-band (34-35 GHz) and Ku-band (~13 GHz) radars have been used extensively to gather high-resolution cloud and precipitation datasets. The next subsection describes retrieval algorithms and processes using airborne (or spaceborne) radar and appropriate ancillary datasets.

#### *1.4.2: Retrieving Cloud and Precipitation Properties*

Perhaps the most frustrating aspect of cloud and precipitation retrieval science lies in the fact that many problems are “ill posed”: there are often more unknown quantities than there are measurements, or a set of input measurements does not guarantee a unique solution. Many inversion techniques, or the process of

inferring a desired variable “X” from some observation “Y”, have been developed for a vast array of applications because such techniques require fully characterized uncertainties [Rodgers 1976]. Understanding cloud and precipitation knowledge requires an understanding of, among other quantities, the number of droplets, the size of those droplets, their terminal fall speeds, and the rate of autoconversion (or accretion). Many airborne and spaceborne remote-sensing instruments can infer the liquid water path, cloud top effective radius and cloud optical depth within a prescribed volume of air from known quantities such as brightness temperature ( $T_b$ ), reflectance, radar reflectivity, and even two-way path integrated extinction (attenuation). Retrieving precipitation is much harder, however, given that we can never truly know the exact distribution and sizes of drops in a volume.

Parameterizing drop size distributions (DSDs) from reflectivity data and estimating corresponding rain rates from those data remains the primary method for retrieving a rainfall rate from a reflectivity measurement. A typical DSD used in many applications is the gamma DSD [e.g. Marshall and Palmer, 1948; Abel and Boutle, 2012] and is written as:

$$N(D) = N_0 D^\mu \exp(-\lambda D) \quad (1.1)$$

In equation (1),  $N_0$ ,  $\mu$  and  $\lambda$  are the intercept parameter, shape factor and slope factor respectively. If the shape factor of 0 is assumed, the gamma distribution reduces to an exponential size distribution such as the Marshall-Palmer DSD:

$$N(D) = N_0 \exp(-\lambda D) \quad (1.2)$$

For given terminal fall speeds  $V(D)$  of given drop sizes [e.g. Gunn and Kinzler, 1949; Beard 1976], the rainfall rate can be computed as:

$$R = \frac{\pi}{6} \rho_L \int_0^{\infty} D^3 N(D) V(D) dD \quad (1.3)$$

The ill posed nature of the retrieval problem becomes immediately apparent when one realizes either two or three unknown quantities rest in the rainfall rate equation via equations 1.1 and 1.2.

Z-R relationships (i.e. reflectivity to rain rate) represent simplest methods equating a radar reflectivity to a given rainfall rate. Many relationships take the form:

$$Z = aR^b \quad (1.4)$$

The constants  $a$  and  $b$  in (4) are fit parameters, akin to Marshall and Palmer (1948) and many others. Such relationships are very computationally inexpensive thus offering a quick method for estimating rainfall from a given radar reflectivity, which is often estimated as:

$$Z = \int_0^{\infty} D^6 N(D) dD \quad (1.5)$$

Where  $D$  is the diameter (typically in millimeters or mm) and  $N(D)$  is the number of drops at a given range of diameters denoted by  $dD$ . For most weather radars (X band through L band), reflectivity estimated using (4) is acceptable given that the Rayleigh assumption holds for large raindrops (i.e. greater than 2-3 mm). This assumption breaks down for most spaceborne radars, which operate at Ku-band (~13-14 GHz), Ka-band (35 GHz) and W-band (94-95 GHz), due to the ratio of the radar pulse's frequency to the size of the target hydrometeors. L'Ecuyer and Stephens (2002) demonstrated that the Raleigh assumption only held for Ku-band radar if the rain rates throughout the radar profile were under 2.5 mm/hr, meaning

Ka-band and W-band radars must account for Mie scattering effects. To circumvent the issue of Mie scattering effects and the uncertainties introduced by assuming a DSD, a robust radar forward model was introduced in L'Ecuyer and Stephens (2002; equation 5):

$$Z_{eff} = \exp \left[ -2 \int_0^r k_{ext}(s) ds \right] \times \frac{\lambda^4}{4\pi^5 |K|^2} \int Q_{sca} P(\Theta = 180) \pi D^2 N(D) dD \quad (1.6)$$

In Eq. 1.6,  $k_{ext}$  is the extinction or attenuation coefficient,  $K$  is the dielectric constant of water or ice,  $Q_{sca}$  is the scattering efficiency (i.e. the ratio of a hydrometeor's scattering cross section to its geometric cross section), and  $P(\Theta = 180)$  is the scattering phase function in the backscatter direction. This modeled reflectivity accounts for both 2-way attenuation effects and the radar backscatter from a target volume. The equations presented in this subsection provide the basis for the radar forward models used throughout the remainder of this work.

Passive radiometer and imager data, in conjunction with radar reflectivity data, can be used as input to accurately retrieve both cloud and precipitation properties. Ramanujam et al. (2012) used TRMM's Microwave Imager (TMI) and precipitation radar (TRMM PR) data along with a Bayesian retrieval technique that used model generated cloud water content and precipitable (rain) water content to improve the accuracy of retrieved rain rates. The Ramanujam et al. (2012) study also demonstrates how a reasonably accurate a priori constraint (CWC and RWC in their case) can reduce the uncertainty in a final retrieved rain rate product. Another

application of a joint retrieval by Eastman et al. (2019) showed that using CloudSat data as a training dataset increased the accuracy and detection of light precipitation by the Advanced Microwave Radiometer for EOS (AMSR-E).

The concept of using multiple radar frequencies to better estimate rainfall properties has existed for several decades [Weinman et al., 1990], yet studies to this point remain very limited. Weinman et al. (1990) used X- and Ka-band radar reflectivity to derive rainfall rate profiles in maritime clouds. Their study found that rainfall rates retrieved from a separate radiometer plus radar retrieval, using path integrated extinction (attenuation) as an integral constraint, yielded retrieved rainfall rates that agreed to within 25% of those retrieved using the collocated X-band and Ka-band radars. Munchak and Tokay (2008) demonstrated that, by using simulated radar data from two frequencies, the natural variability in DSD slope and shape parameters could be reasonably replicated while also correlating highly with reflectivity. Many of these studies noted the utility of higher frequency (e.g. W-band) radar measurements as a means to better measure light precipitation [e.g. Weinman et al., 1990]. The Advanced Precipitation Radar – 2<sup>nd</sup> Generation (the precursor to the APR-3 radar) was developed as a means to validate TRMM PR radar measurements [Tanelli et al., 2006]. In addition to providing Ku-band and Ka-band measurements, the surface backscatter ( $\sigma_0$  or  $\sigma_0$ ) data from those two channels serve as a reference for calibrating W-band  $\sigma_0$  [Dzambo et al., 2019].

The primary reference for this work follows Lebsock and L'Ecuyer (2011; LL11 hereafter), which implemented the optimal estimation retrieval algorithm from L'Ecuyer and Stephens (2002) for CloudSat's W-band radar but included both a

path integrated attenuation (PIA) and cloud optical depth (COD) integral constraint. The LL11 approach will be expanded upon more thoroughly in Chapters 3 and 4.

### **1.5: The ORACLES Field Campaign**

All results and conclusions in this dissertation are primarily culled from data collected during the ObseRvations of Aerosols above CLouds and their intEractionS (ORACLES) campaign [Redemann et al., *in prep*]. The ORACLES campaign, a three-year field campaign over the Southeast Atlantic Ocean, collected a “first-of-its-kind” dataset specifically for the study of cloud-aerosol-precipitation interactions. A related experiment, the Southern Africa Regional Science Initiative (SAFARI) 2000 experiment, collected in-situ cloud and biomass burning aerosol measurements [Haywood et al., 2003] but lacked the remote sensing capabilities of ORACLES. The ORACLES campaign was based out of Walvis Bay, Namibia (22.9584°S, 14.5058°E) in 2016 and out of São Tomé, São Tomé and Príncipe (0.1864°N, 6.6131°E) in 2017 and 2018. For 2016 and 2017, select research flights transited to and from Ascension Island (7.9467°S, 14.3559°W). Flying to/from Ascension Island allowed for longitudinal variations in cloud and aerosol properties to be studied, otherwise, acquiring measurements in the westernmost regions of the StCu deck and biomass burning layer would have been logistically challenging. Observations collected in the westernmost regions, especially around Ascension Island, sometimes contained ultra-clean layer akin to those observed during CSET [Pennypacker et al., 2019]. Figure 1.2 highlights these locations along with the experiment area.

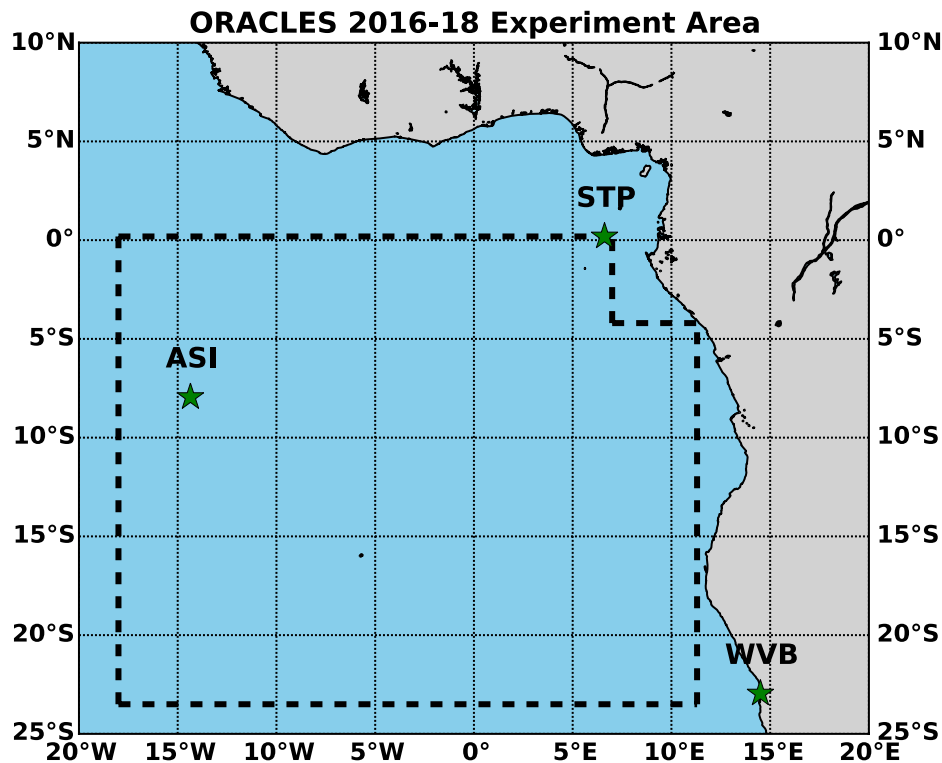


**Figure 1.2:** The ORACLES experiment region (enclosed in a dashed black box) for the 2016-18 campaigns, with São Tomé (STP), Walvis Bay (WVB) and Ascension Island (ASI) marked as green stars.

### 1.6: Hypotheses

While macrophysical and microphysical processes controlling StCu formation and lifetime are reasonably well understood, accurately capturing these processes in climate models remains a critical challenge. Assessing the magnitude of changes to precipitation frequency and rate from aerosol effects, and their subsequent influences on the local energy budget, have become possible with the ORACLES field campaign. The remainder of this dissertation will focus on three related subject areas, each of which are guided by the following science questions:

1. (SQ1) What are the retrieved precipitation rates from airborne radar, and how do environmental controls explain variations in these precipitation rates?
2. (SQ2) Using multiple airborne remote sensing datasets, is the presence of aerosol-induced precipitation suppression observed during ORACLES?
3. (SQ3) What are the relative roles of virga and surface precipitation on the local energy budget?

To answer the above science questions, three hypotheses are tested using available ORACLES data. Each hypothesis bears in mind the numerous studies dissecting the cloud-aerosol-precipitation interplay and the role of precipitation processes in driving local latent heating budgets. The hypotheses are as follows:

1. The majority of retrieved precipitation rates from clouds observed during ORACLES will be less than 2 mm/day ( $\sim 0.1$  mm/hr) reflecting expected drizzling stratocumulus clouds, and with variability due to varying environmental conditions.
2. The presence of fine-mode aerosols produces a statistically-significant reduction in precipitation frequency and magnitude, given the large number of radar observations available in regions of the SE Atlantic Ocean that exhibit consistent (or relatively stagnant) environmental and meteorological conditions.
3. Latent cooling from evaporating virga is greater than the latent cooling from evaporation by surface precipitation, given that virga occurs more frequently in these clouds.

## **Chapter 2: Datasets**

Unless otherwise stated, all datasets used for this research were collected during the ORACLES field campaign. Over 20 instruments flew aboard the NASA P-3 (2016-18) and ER-2 aircraft (2016 only). Three of these instruments provide the necessary data to address all hypotheses. The ORACLES campaign took place entirely during daylight conditions, therefore no results presented throughout this work account for diurnal variability though the effects of diurnal variability on any results will be noted and addressed in future works. The remaining subsections in this chapter highlight all datasets used in the remaining chapters.

### **2.1: The Advanced Precipitation Radar – 3<sup>rd</sup> Generation (APR-3)**

The Advanced Precipitation Radar – 3<sup>rd</sup> Generation (APR-3) provides the main dataset used throughout this dissertation. The APR-3 measured profiles of collocated Ku- (13 GHz), Ka- (35 GHz) and W- (95 GHz) band reflectivity and Doppler velocity, revealing cloud vertical structure and in-cloud precipitation processes in unprecedented detail. Given the radar's narrow beamwidth of 0.9 degrees and the aircraft's maximum altitude of ~7 km, the effects of non-uniform beamfilling and multiple scattering are minimal. Over the course of the three ORACLES campaigns, the APR-3 collected over 18 million reflectivity profiles with vertical resolutions ranging from 35 meters to 8.6 meters. Surface noise or "ground clutter" is limited to about 200 meters (sometimes less) in the W-band observations,

enabling the study of near-surface precipitation (more information is provided in sections 3.2 and 3.3).

The ORACLES experiment is the second field campaign to offer triple-frequency, simultaneously collocated radar data from the APR-3. The APR-3 was first deployed in the Olympic Mountains Field Experiment (OLYMPEX) in 2015 to study cold-cloud precipitation processes [Houze et al., 2017]. Recent studies from the OLYMPEX campaign have demonstrated the utility of multiple radar channels in retrieving snowfall properties [Leinonen et al., 2018] that compare well with derived in-situ quantities [Chase et al., 2018]. The APR-3 was also deployed for the recent NASA CAMP2Ex field campaign (summer 2019), which aimed to study aerosol effects on deep tropical convection. For ORACLES, the W-band reflectivity channel is used exclusively because minimal data from the Ka-band and Ku-band frequencies exist in the main StCu deck, although trade cumulus near the equator and in the StCu-to-Cu transition zones supply data to develop and investigate multi-frequency warm rain retrievals.

During ORACLES 2016, over 3 million reflectivity profiles at each frequency were collected primarily in very stable, non- or lightly-precipitating regions off the coast of Namibia while close to 7 million profiles were collected in 2017 in less stable, more inhomogeneous clouds with both convective and stratiform warm rain south of Saõ Tomé. In 2018, nearly 8 million reflectivity profiles were collected. The 2018 dataset was not yet available for the study containing Chapter 3 (Chapters 4 and 5 contain 2018 APR-3 data). Comparisons of APR-3 data (and any retrieved quantity from the APR-3 data) to in-situ measurements are presently an active

research topic by other investigators affiliated with ORACLES, and will be the topic of future collaborative research efforts.

Data from the APR-3 are used in all remaining chapters. Tables of variables used, including retrieved quantities, are part of the Methods section of each science chapter.

## **2.2: The Research Scanning Polarimeter (RSP)**

The Research Scanning Polarimeter (RSP), also flying aboard the NASA P-3 aircraft during ORACLES, is an airborne version of the Earth Observing Scanning Polarimeter (EOSP) [Travis 1993; Cairns et al., 2003]. The RSP provides complimentary cloud optical depth (COD) and effective radius ( $r_e$ ) data via multi-angle, high precision polarization measurements from clouds [Chowdhary et al., 2001]. Both COD and  $r_e$  are retrieved using either the shortwave infrared channels [Elias et al., 2004] or polarization measurements from multiple scanning and viewing angles [Nakajima and King, 1990]. For this work, the multi-angle polarimetry retrieval is advantageous over the shortwave infrared channels because multi-angle polarimetry measurements are more robust for broken cloud and precipitating thin cloud [Bastiaan van Diedenhoven, personal communication].

A summary of the multi-angle polarimetry retrieval is presented here for completeness. Cloud droplet size retrievals from the RSP use polarized reflectances from 135 to 165 degrees (known as the cloud-bow or rain-bow). The single scattering properties of cloud (or rain) droplets directly determines the shape of the cloud- (or rain-) bow, which enables both a simplified retrieval of cloud properties

and mitigates uncertainties from aerosol loading or undetectable thin clouds [Alexandrov et al., 2012].

For the ORACLES experiment, RSP measurements offer the most reliable data to constrain retrieved cloud water path for a few reasons:

1. Bias in cloud optical depth estimates from aerosols is small, given that most optical depths observed are generally small [Brian Cairns, personal communication].
2. The AMPR instrument would have provided the most ideal integral constraint: a precipitable water path (PWP) constraint. This data was only available in 2016, nor was a PWP constraint available at the time of this writing.
3. COD and  $r_e$  estimates from SSFR instrument have large uncertainties from high-altitude legs due to the fact the instrument averages measurements over a large footprint. SSFR retrieval biases are presently being investigated [Sebastian Schmidt, personal communication].

For this study, COD and  $r_e$  data (0.865  $\mu\text{m}$  channel) are employed. Their use, including the uncertainty associated with each instrument, is more rigorously described in Chapter 4. Finally, the RSP team offered a few notes of caution regarding interpretation of the optical depth and effective radius data.

1. Optical depth retrievals for very bright clouds have low accuracy because reflectance is almost saturated at its semi-infinite value [Brian Cairns, personal communication].

2. Regardless, optical depth spikes are indicative of an extremely optically thick clouds and a very bright reflectance. Bright reflectances reduce the accuracy of estimated LWP because they exceed the limits of the look-up table. In general, values greater than  $150 \text{ g m}^{-2}$  should be interpreted with caution.
3. A calibration issue may have affected some data from 2018, and potential biases between 2017 and 2018 are presently under investigation [Bastiaan van Diedenhoven, personal communication].

### **2.3: The High Spectral Resolution Lidar – 2<sup>nd</sup> Generation (HSRL-2)**

High-resolution data of aerosol layers were detected and characterized by the High Spectral Resolution Lidar [HSRL-2, Hair et al., 2008]. The airborne-based HSRL-2 can easily detect the bottom of aerosol layers, representing a critical advantage over satellite lidars such as CALIPSO [Zuidema et al., 2016]. The HSRL-2 independently retrieves aerosol backscatter and extinction coefficients, meaning a comparison between extensive properties (e.g. aerosol backscatter coefficient and aerosol optical depth) can be done without a host of other assumptions [Burton et al., 2012; Burton et al., 2018]. The HSRL-2 also compliments the APR-3 by providing an independent measure of cloud top height, although the HSRL-2 quickly attenuates in atmospheric layers containing high liquid (or ice) water content or mid to high altitude cloud cover.

An example of a radar-lidar “curtain” is shown in Fig. 2.1. On 27 Sept. 2018, drizzling stratocumulus were frequently observed especially on the outbound flight leg. Aerosol clearly contacts the top of the MBL for the entire flight. The clouds

detected on the outbound flight leg were not present at the time of the return flight leg, meaning these clouds either advected away from this flight track or dissipated. This is visible in the lidar curtain as a  $\sim 3^\circ$  latitudinal swath of lidar profiles to the surface, meaning no clouds or high LWC are present.

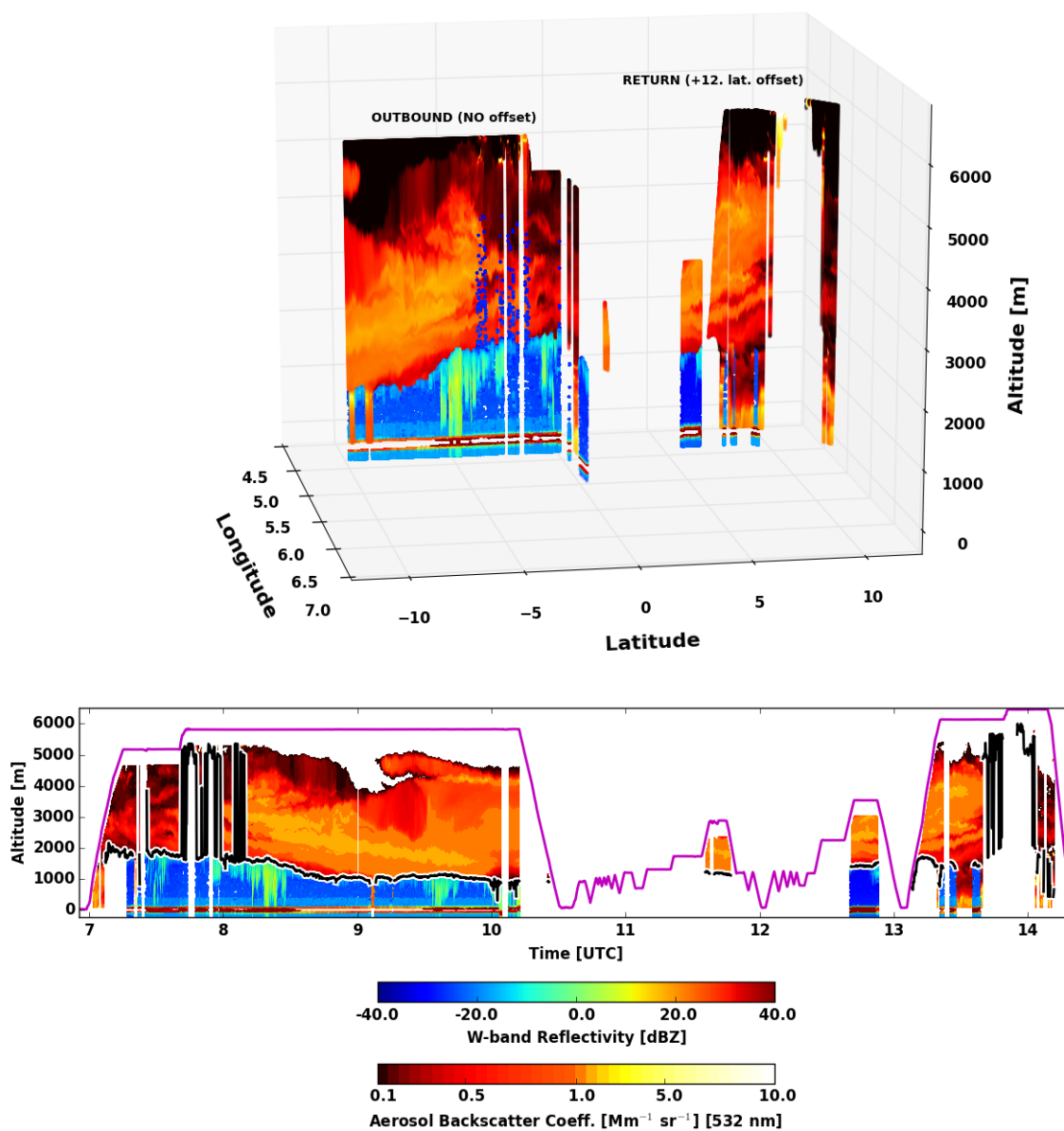


**Figure 2.1:** A merged radar-lidar curtain from the 27 Sep. 2018 ORACLES research flight. The top panel shows a 3D representation of the outbound (left) and return (right, offset by 12 degrees latitude for plotting purposes) flight leg curtains. The bottom panel shows the full 2D curtain for the entire flight.

In addition to elucidating when aerosols are in contact with underlying StCu, the HSRL-2 can also determine aerosol type (e.g. dust vs. smoke) and character (i.e. fine mode vs. coarse mode). This is especially important given that increasing fine mode aerosol concentrations lead to increasing cloud coverage regardless of meteorological or environmental controls [Adebiyi and Zuidema, 2018]. The aerosol classification scheme is based entirely on intensive measurements (i.e. depolarization, extinction-to-backscatter ratio, backscatter color ratio, and ratio of aerosol depolarization ratios), meaning a classification can be made independently of the aerosol type or amount (the use of specific variables and datasets are covered more thoroughly in Chapter 4). The primary aerosols characterizing the biomass burning layer observed during ORACLES, following the Burton et al. (2012) algorithm, was either fresh smoke, smoke, or dusty mix. In the absence of attenuation, the HSRL also frequently revealed marine boundary layer (e.g. sea salt) and polluted marine (e.g. mix of smoke and sea salt) aerosols.

#### **2.4: Data Availability and Sampling Considerations**

While the quantity of data available from ORACLES is vast, the amount of data available from successive campaigns varies quite a bit. The logistical challenge of stationing the experiment in Namibia in 2016 was especially complicated, coupled with the fact that a handful of instruments (namely a second RSP as well as

the HSRL-2) flew on the NASA ER-2 aircraft. The ER-2 did not partake in ORACLES 2017 or 2018, and given the challenges arising from “quasi”-collocating APR-3 and ER-2 based measurements, no ER-2 based data are used anywhere throughout this dissertation. The 2017 experiment, the first ORACLES campaign stationed in São Tomé, was initially mired by aircraft mechanical issues and rendered RF01 void of data. Aside from an aborted flight on 19 Aug. 2017 and 30-31 Aug. 2017 where HSRL-2 were unavailable, data collection for the 2017 campaign was successful. Finally, with an upgraded APR-3 computer system and no aircraft mechanical issues, no data collection issues occurred from any of the APR-3, RSP and HSRL-2 during the 2018 campaign. Table 2.1 highlights the availability of data for each flight.

**Table 2.1:** Description of data availability for the ORACLES 2016-18 field campaigns. The 27 Sep. 2016 flight was classified a “transit flight” but is included in this analysis because the transit flight took place entirely in the experiment area between Walvis Bay, Namibia and Ascension Island and is denoted by a single asterisk (\*). For the 2016 experiment, (\*\*) denotes where instrument data is available, but only from the NASA ER-2 aircraft. No ER-2 data is used.

	APR-3 2016	HSRL-2 2016	RSP 2016		APR-3 2017	HSRL 2017	RSP 2017		APR-3 2018	HSRL-2 2018	RSP 2018
08-30-16				08-12-17				09-27-18	Y	Y	Y
08-31-16	Y		Y	08-13-17	Y	Y	Y	09-30-18	Y	Y	Y
09-02-16	Y		N	08-15-17	Y	Y	Y	10-02-18	Y	Y	Y
09-04-16	Y		N	08-17-17	Y	Y	Y	10-03-18	Y	Y	Y
09-06-16	Y		N	08-18-17	Y	Y	Y	10-05-18	Y	Y	Y
09-08-16	Y		N	08-19-17	N	N	N	10-07-18	Y	Y	Y
09-10-16	Y		Y	08-21-17	Y	Y	Y	10-10-18	Y	Y	Y
09-12-16	Y	Y**	N	08-24-17	Y	Y	Y	10-12-18	Y	Y	Y
09-14-16	Y	N	Y	08-26-17	Y	Y	Y	10-15-18	Y	Y	Y
09-18-16	Y	Y**	Y	08-28-17	Y	Y	Y	10-17-18	Y	Y	Y
09-20-16	Y	Y**	Y	08-30-17	Y	N	Y	10-19-18	Y	Y	Y
09-24-16	Y	Y**	N	08-31-17	Y	N	Y	10-21-18	Y	Y	Y
09-25-16	Y	Y**	N					10-23-18	Y	Y	Y
09-27-16*	Y	Y**	N								

A key consideration for all results presented in this dissertation lies in the sampling of the StCu deck. For most research flights, the NASA P-3 aircraft flew “routine” flight tracks along straight lines, which never guaranteed that every StCu cloud sample would span its true diameter. The StCu cloud deck across the SE Atlantic Ocean (for every flight) was generally homogeneous, thus any transect of a cloud could be characterized by some probability function if the areal shapes of all StCu clouds are circular. Figure 2.2 shows the cumulative probability of the normalized distance sampled for one million arbitrary, circular clouds. Over 50% of all transects sample 70% or more of a cloud’s true diameter and 25% of all transects

sample 85% of the same diameter. The probability that the aircraft sampled the outer edge of a stratocumulus cloud happened frequently, and any result implies this caveat. The major implication of this concept follows that, if the full diameter is not fully sampled, the centers of any cloud (where brightness/reflectance or droplet growth might be maximized) or rain shaft (where precipitation rates are most likely maximized) are most likely under-sampled. Regardless, the majority of all transects are likely to sample at least 70% of any cloud's true diameter.

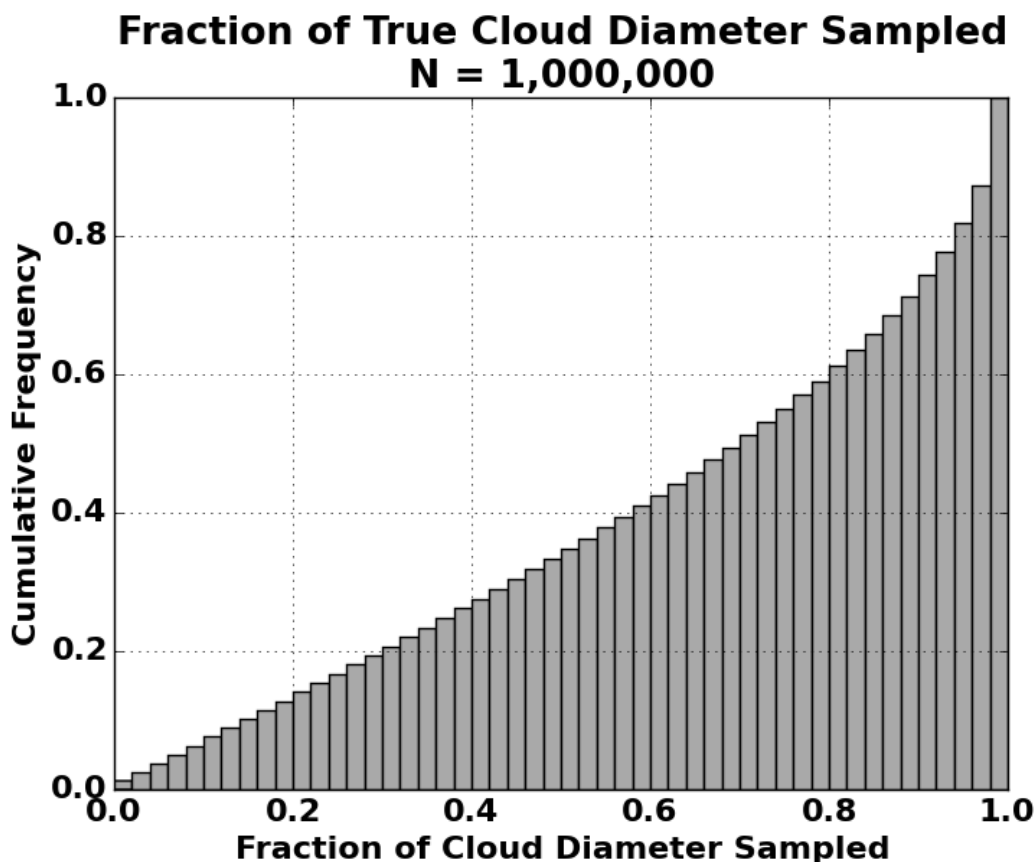


**Figure 2.2:** The probability of true cloud diameters likely sampled by the NASA P-3 aircraft during ORACLES. Data presented in this figure assume that all “clouds” cover a circular area, where the distance between two points on a circle are calculated using a randomly selected angle. This figure shows the result for one million simulated transects across a cloud's true diameter.

Given that this dissertation focuses primarily on StCu precipitation processes, a brief summary of campaign precipitation is shown in Fig. 2.3. One of the key ORACLES science objectives was to observe cloud-aerosol-precipitation interactions over a full biomass burning seasonal cycle. ORACLES 2016 (Sep., or mid-season), 2017 (Aug., or early-season) and 2018 (Oct., or late-season) accomplished exactly that. The frequency of light precipitation was highest during the 2016 season, with higher frequencies of moderate and heavy precipitation occurring in 2017 and especially 2018. Statistics in Fig. 2.3 do not exclude the frequent trade cumulus observed during the 2017 and 2018 campaigns, though the fraction of data relative to the observed StCu deck is relatively small. It is worth mentioning again that the 2016 campaign was stationed in Namibia, thus most flights were devoid of any trade cumulus or any cloud undergoing the StCu-to-Cu transition. Chapter 3 delves into the precipitation statistics more thoroughly, while Chapter 4 expands upon cloud properties and uncertainties arising from these statistics. Finally, Chapter 5 contains an assessment of evaporation processes in the SE Atlantic Ocean.

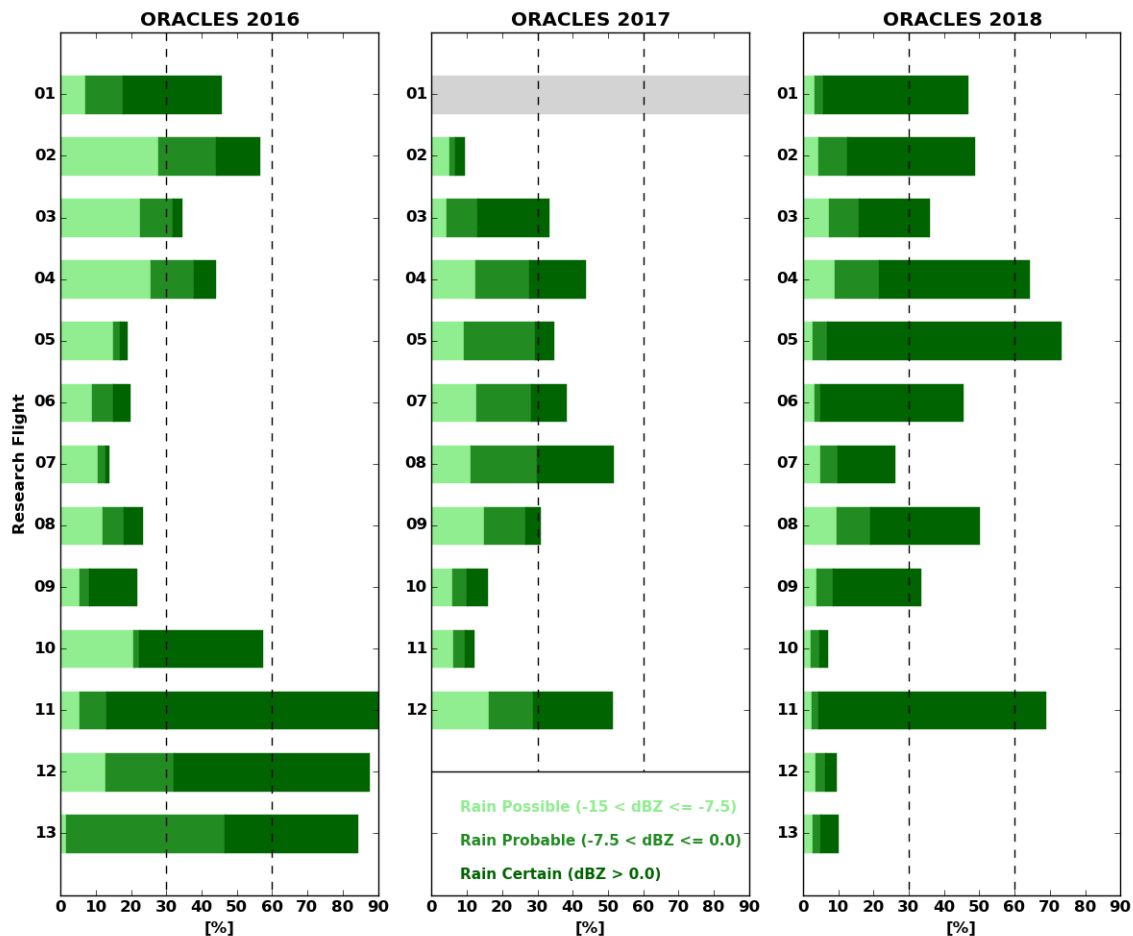


**Figure 2.3:** Rain probability estimates for all ORACLES research flights. The rain possible (light green), rain probable (medium green) and rain certain (dark green) assume a maximum column radar reflectivity greater than  $-15$  dBZ,  $-7.5$  dBZ and  $0.0$  dBZ respectively. These classifications follow the same classification scheme as CloudSat (Haynes et al., 2009) and generated using the 2C-RAIN algorithm generated in Dzambo et al. (2019), both of which are described in Chapter 3. Adapted from Redemann et al., in prep.

### **Chapter 3: The observed structure and precipitation characteristics of southeast Atlantic stratocumulus from airborne radar during ORACLES 2016-17**

The following chapter was published in the *Journal of Applied Meteorology and Climatology* on 7 October 2019, titled “The Observed Structure and Precipitation Characteristics of Southeast Atlantic Stratocumulus from Airborne Radar during ORACLES 2016-17.” This paper is adapted here to fit this dissertation and acknowledges the copyright owned by the American Meteorological Society.

#### **3.1: Introduction**

Stratocumulus clouds are the dominant cloud cover type over the world’s oceans [Warren et al., 2007] and have a pronounced influence on Earth’s energy balance [e.g. Wood 2012]. Stratocumulus cloud properties, formation, and maintenance depend on a number of complex processes including entrainment between the planetary boundary layer (PBL) and free atmosphere [Gerber 1996], cloud condensation nuclei (CCN) concentration [Zhang et al., 2004], regional large-scale dynamics [Wood et al., 2002], and warm cloud microphysical processes such as condensation and collision-coalescence [Bennartz 2007]. Precipitation processes affect StCu lifetime in a number of ways such as, for example, modulating number concentration [Mohrmann et al., 2018] and scavenging cloud condensation nuclei (CCN) from the PBL [Albrecht, 1989; Wood 2006]. If a CCN can be activated and grow via coalescence to a sufficiently large size, drizzle can “wash out” aerosol

particulates and other CCN from the PBL toward the ocean surface [Wood 2006] or, if the drizzle drop evaporates before reaching the ocean surface, the number of available CCN is still depleted from the cloud layer but redistributed through the PBL [Diamond et al., 2018]. Precipitation processes are further complicated by environmental processes in which StCu reside and depend on local stability, relative humidity, liquid water path (LWP) and boundary layer decoupling [Wood 2012; Wood et al., 2018]. Unsurprisingly, the diurnal variability of these processes and environmental variables adds yet another layer of complexity toward understanding precipitation processes in StCu clouds [Wood et al., 2002].

Ideally, studies focused on cloud-aerosol-precipitation processes would take place in the northeast Pacific Ocean, southeast Pacific Ocean, and southeast Atlantic Ocean, where stratocumulus clouds are commonly observed. In the SE Atlantic Ocean, the presence of a southern-hemisphere wintertime biomass-burning (BB) layer over this region's StCu deck complicates cloud evolution and associated precipitation processes. Uncertainties in aerosol properties [Meyer et al., 2015; Peers et al., 2016; Sayer et al., 2016], radiative effects [Matus et al., 2015] and cloud morphology responses to these aerosols [Yamaguchi et al., 2015] have made the SE Atlantic Ocean among the most challenging regions of the globe to model [Zuidema et al., 2016].

A number of recent field campaigns have specifically targeted subtropical clouds and their precipitation processes. In 2008, results utilizing data from the VAMOS Ocean-Cloud-Atmosphere-Land (VOCALS) improved our understanding of the land-ocean-atmosphere system [Wood et al., 2011]. Data from VOCALS, at that

time, was among the most robust to use for studying how cloud and precipitation processes in affect regional climate in the southeast Pacific. The Atlantic Stratocumulus experiment [ASTEX; Albrecht et al., 1995] and the Clouds, Aerosol, and Precipitation in the Marine Boundary Layer [CAP-MBL; Wood et al., 2015] focused on StCu in the northeast Atlantic. Recently, the Cloud System Evolution in the Trades (CSET) experiment utilized the HIAPER Cloud Radar and High Spectral Resolution Lidar, complimented with a variety of in-situ measurements, to study clouds in ultra-clean boundary layers over the northeast Pacific Ocean [Albrecht et al., 2018]. Until recently, however, all such experiments have sampled clouds in the northeast Pacific, southeast Pacific, west Pacific, and northeast Atlantic. In these regions, StCu cloud decks are not influenced by a seasonal biomass-burning layer such as the one in the southeast Atlantic.

The ObseRvations of Aerosols above CLouds and their intEractionS (ORACLES) campaign, taking place over the southeast Atlantic Ocean from 2016-2018, has provided new and unique observations for assessing cloud and aerosol interactions. Over the course of the first two years of the experiment, 18 different instruments have flown on the NASA ER-2 and P-3 aircrafts documenting aerosols, clouds, and precipitation and their interactions. The observational domain was extensive: measurements were collected from São Tomé ( $\sim 0.2^\circ\text{N}$ ) to approximately  $25^\circ\text{S}$  and from Ascension Island to the Western African coast.

We utilize the APR-3 radar data (with emphasis on the W-band) and an adapted optimal estimation technique to estimate precipitation probability and rate, cloud fraction, and cloud top height of StCu over the SE Atlantic Ocean during both

the ORACLES 2016 and 2017 deployments. This work utilizes this new APR-3 W-band precipitation dataset to document the characteristics of warm rain in two broad domains over the SE Atlantic observed during ORACLES 2016 and 2017. A preliminary analysis of the observed precipitation characteristics, supplemented with the European Centre for Medium-Range Weather Forecasts (ECMWF) Re-Analysis (ERA) Interim reanalysis dataset (ERA-I hereafter; Dee et al., 2011), emphasizes the strong meteorological controls on cloud cover and warm rain in the SE Atlantic, reinforcing the need to account for such controls when addressing the aerosol-cloud-precipitation interactions objectives targeted by ORACLES.

### **3.2: The APR-3 dataset**

The APR-3 dataset described in Chapter 2 are utilized throughout this study. We emphasize W-band reflectivity measurements for this study due to their high sensitivity and ability to detect very thin StCu clouds (see Fig. 3.1). In this cloud regime, the utility of the Ku-band channel lies primarily in its measurements of ocean backscatter (a standard for radar calibration). The Ka-band channel role is primarily to provide an additional constraint for retrievals of light precipitation, and as transfer of the calibration reference from Ku- to W-band (through the comparison of observed reflectivity in regions where the Rayleigh assumption holds for a pair of radar bands). During high altitude flight legs (typically around 6 to 7 km above ground level), the APR-3 W-band measurements were acquired with a long pulse (1  $\mu$ s), whereas for flight legs taking place directly above the StCu cloud deck (typically 100 to 300 m above the cloud top), a shorter pulse was sometimes

adopted (typically 500 ns) since the sensitivity is greatly improved by the relatively short range. Furthermore, two products are routinely generated: a low horizontal resolution product (where pulses are integrated for approximately 1 s, resulting in an along track resolution of more than 100 m, depending on the aircraft ground speed) and a high horizontal resolution product (where integration spans only approximately 50 ms and the horizontal resolution is therefore mainly determined by the  $0.9^\circ$  antenna beamwidth, though this comes at the expense of about 10 dB in sensitivity due to the reduction in available independent samples in the process of noise estimation and subtraction). For comparison, the W-band high-resolution short pulses have sensitivity between -26 and -32 dBZ at 1 km away from the radar, while the long pulses have sensitivity between -35 and -38 dBZ at the same distance away from the aircraft. Overall, more than 10 million W-band radar profiles are available for 2016 and 2017, and additional W-band radar observations will be available from ORACLES once the 2018 dataset is processed, quality controlled and distributed.

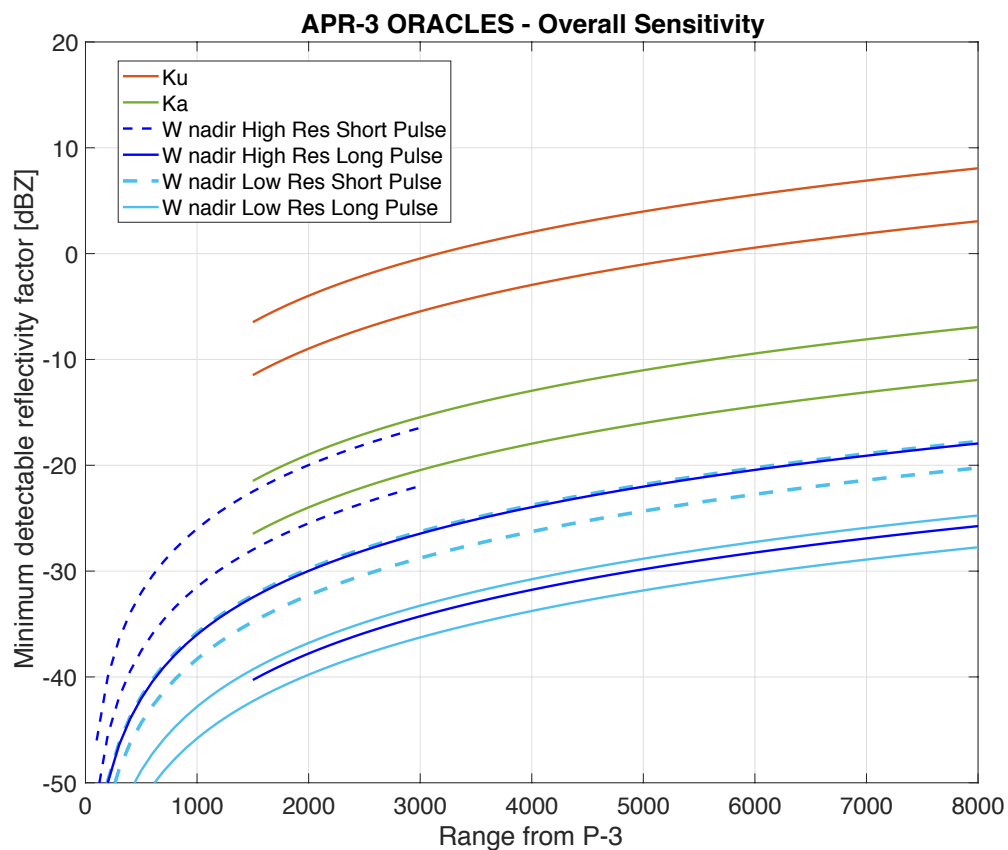


**Figure 3.1:** Sensitivity of the Ku-, Ka- and W-band channels as a function of distance from the aircraft for the ORACLES 2016 mission. The radar performance in 2017 was slightly improved due to upgrades in the processing system. Each set of lines represents a sensitivity range, which varied depending on the configuration of each scan.

A triple frequency radar scan from the 04 September 2016 research flight is shown in Fig. 3.2. StCu clouds are evident throughout this scan, and a pronounced shallow convective cell occurred between 21 km and 28 km along this flight leg and is clearly evident in the Ka-band and W-band radar scans. The cloud top height of this convective cell is approximately 1.4 km altitude in the W-band channel and below 1.3 km in the Ka-band channel demonstrating the enhanced sensitivity of the W-band radar to small liquid droplets near cloud top. Fig. 3.2 also illustrates

attenuation in the W-band channel: at 26 km, reflectivities between -2 dBZ and 0 dBZ are between 3 and 6 dBZ in the Ka-band channel (between 0.5 and 1.0 km). The surface backscatter or  $\sigma_0$  data (overlaid on the top panel of Fig. 3.2) corroborate this by showing path-integrated attenuation (PIA) of 3-4 dB in this convective cell.

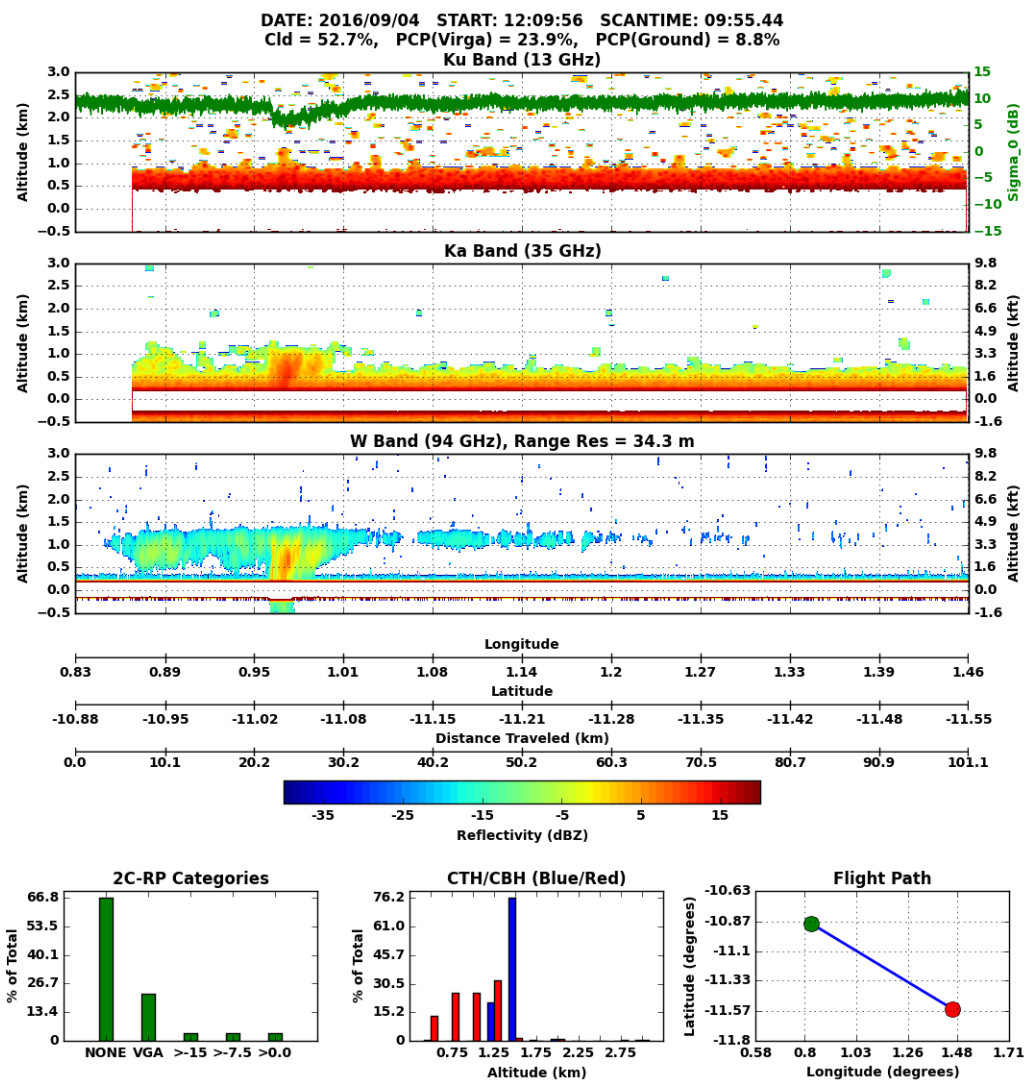


**Figure 3.2:** APR-3 Ku-band (top), Ka-band (middle) and W-band (bottom) reflectivity image from 04 September 2016. This transect began at 12:09:53 UTC and lasted for 9 minutes and 55 seconds. Latitude, longitude and ground distance

traveled are all shown as separate x-axes. The colorbar for reflectivity is tuned to W-band (-40 to 20 dBZ) and is the same for all three radar images. Surface backscatter observed at W-band ( $\sigma_0$ ) is overlaid on the Ku-band image as a green line. The bottom-left histogram represents categories based on the 2C-PRECIP-COLUMN algorithm and shows clear-sky/thin cloud (far left), virga (percent of cloudy profiles with > -15 dBZ NOT reaching the surface; left), rain possible (surface reflectivity between -15 and -7.5 dBZ; middle), rain probable (surface reflectivity between -7.5 and 0 dBZ; right) and rain certain (surface reflectivity greater than 0 dBZ; far right). The bottom-middle histogram shows the percentage of altitudes where cloud base and cloud top altitude occur (for all cloudy profiles in this scene). The bottom-right plot shows the flight track for this particular leg.

Surface clutter and background noise are removed from every W-band radar scene. Surface clutter in the APR-3 W-band dataset is typically present in the lowest six range bins (i.e. ~210 meters above the surface). In order to avoid misinterpreting clutter as clouds or precipitation we mask all radar pixels below 200 m and compute an effective “surface” precipitation rate at this altitude. Background noise is first identified and removed following Marchand (2008), which assigns values based on the likelihood of a radar return being a cloud. We remove background noise (certain cloud is assigned 40, etc.). This procedure eliminates most ground clutter and excludes surface returns, however, an extra step must be taken to eliminate noise that passed this initial screening. We removed remaining background noise by iteratively searching a 7x7 bin square and establishing the number of reflectivity values exceeding the minimum sensitivity at that range (see Fig. 3.1). If at least half of the reflectivity values in the 7x7 search square are valid the data are kept in this scene otherwise the pixel is considered noise and all reflectivities in the box are masked. This methodology for removing background noise, adapted from Clothiaux et al. (1995) and Marchand (2008), provides a

compromise between removing obvious noise in the data without inadvertently removing legitimate cloud scenes, although some very thin, isolated cloud scenes may be screened. Removing noise and ground clutter in these scenes helps us more accurately quantify W-band detected cloud top and base heights improving our confidence in the resulting mean cloud top and echo base statistics while also providing unambiguous estimates of precipitation intensity.

### **3.3: Methods**

Precipitation in StCu clouds is retrieved using an adapted version of the CloudSat 2C-RAIN-PROFILE (2C-RP hereafter) algorithm that has been adapted to airborne W-band radar observations [L'Ecuyer and Stephens, 2002; Haynes et al., 2009; Mitrescu et al., 2010; Lebsock and L'Ecuyer, 2011]. 2C-RP was developed for CloudSat as a means to retrieve rainfall from space using a constrained iterative estimation technique. 2C-RP combines a reflectivity profile of any depth, a surface backscatter measurement (i.e.  $\sigma_0$  or  $\sigma_0$ ), a profile of gas attenuation derived from background atmospheric state variables, and surface state variables to retrieve profiles of size distribution parameters and associated liquid water contents and surface rainfall rates (Table 3.1). Cloud structure and retrieved rainfall rates are described in the context of estimated inversion strength (EIS, described in section 3.3.4) in sections 4 and 5. The dataset generated by this adapted algorithm can be found online (Lebsock 2011), and Table 3.2 describes the variables in this dataset.

**Table 3.1:** A list of variables required to run the adapted 2C-RAIN-PROFILE algorithm for ORACLES APR-3 data.

<b>Variable</b>	<b>Data Source or Algorithm</b>	<b>Units</b>	<b>Data Type/Comments</b>
<b>W-Band Reflectivity</b>	APR-3	dBZ	Profile
<b>Surface Backscatter (<math>\sigma_0</math>)</b>	APR-3	dBZ	Point measurement
<b>Temperature</b>	ERA-I	Kelvin	Profile
<b>Specific Humidity</b>	ERA-I	kg/kg	Profile
<b>Altitude</b>	ERA-I	meters	Profile; derived from ERA-I Pressure using $p = p_0 e^{-z/H}$
<b>Cloud Mask</b>	N/A	Unitless	Estimated from reflectivity profile following the CloudSat classification criteria.
<b>Gas Attenuation</b>	ERA-I	dB	Estimated from ERA-I data following Matrosov et al. (2004).
<b>Rain Rate Estimate</b>	2C-PRECIP-COLUMN	mm/hr	Estimated from the adapted 2C-PRECIP-COLUMN algorithm.
<b>Rain Rate Uncertainty</b>	2C-PRECIP-COLUMN	%	Estimated from the adapted 2C-PRECIP-COLUMN algorithm.

**Table 3.2:** List of variables in the Level 2 precipitation retrieval dataset.

Full Name	Units	Dimensions	Comments/Information
<b>Precipitation Flag</b>	unitless	[time]	Precipitation occurrence flag
<b>Quality Flag</b>	unitless	[time]	Precipitation quality flag (0 = no confidence, 4 = high confidence)
<b>Status Flag</b>	unitless	[time]	Algorithm status (0 = computed from 2C-RP, 1 = passed through from 2C-PC)
<b>Surface Rain Rate</b>	mm/hr	[time]	Surface rainfall rate, see text for data quality requirements.
<b>Surface Rain Rate Uncertainty</b>	%	[time]	Uncertainty in the retrieved surface rainfall rate.
<b>Path Integrated Attenuation</b>	dB	[time]	Path integrated attenuation estimated from 2C-RP.
<b>Liquid Water Path</b>	g/m <sup>2</sup>	[time]	Liquid water path through the depth of the cloud.
<b>Evaporation</b>	kg/kg	[time]	Modeled evaporation from cloud base to surface based on Feingold (1993).
<b>Attenuation-corrected Reflectivity</b>	dBZ	[time, height]	W-band reflectivity corrected for hydrometeor attenuation and multiple scattering.
<b>Hydrometeor Attenuation</b>	dB	[time, height]	Profile of hydrometeor attenuation computed by 2C-RP.
<b>Liquid Water Content</b>	g/m <sup>3</sup>	[time, height]	Profile of liquid water content estimated by 2C-RP using the AB13 DSD.
<b>Rain Rate Profile</b>	mm/hr	[time, height]	Profile of rainfall rate estimated from liquid water content.

### *3.3.1: Gas attenuation correction*

Airborne and spaceborne high frequency radar measurements are susceptible to attenuation from water vapor. In the tropical oceans, W-band reflectivity can be attenuated as much as 2-4 dB (sometimes more). To account for this, APR-3 W-band reflectivity profiles are corrected for gas attenuation following Matrosov et al. (2004). We use profiles of temperature, specific humidity and total column water vapor from the ERA-I dataset [Dee et al., 2011] to derive appropriate gas attenuation profiles from both oxygen and water vapor.

### *3.3.2: Adapted 2C-PRECIP-COLUMN overview*

Rainfall and drizzle are identified using an adapted version of CloudSat's 2C-PRECIP-COLUMN algorithm [2C-PC, Haynes et al., 2009]. Reflectivity profiles are tagged as rain possible, rain probable or rain certain if near-surface (200 m) reflectivities exceed -15, -7.5 and 0.0 dBZ respectively. These categories can be loosely interpreted as light drizzle, drizzle, and rain though it should be noted that these terms correspond to precise reflectivity thresholds in subsequent discussion. An initial rain rate intensity estimate and uncertainty is derived for all reflectivity profiles that contain drizzle or rain using the path-integrated attenuation (PIA) and assuming a Marshall-Palmer drop size distribution [Marshall and Palmer, 1948]. PIA is estimated by subtracting the W-band observed  $\sigma_0$  from a climatological clear-sky  $\sigma_0$ , which is determined from a lookup table constructed by matching CloudSat clear-sky data to Advanced Microwave Sounding Radiometer (AMS-R-E) sea surface temperature and wind speed observations for a wide range of scenes [Tanelli et al.,

2008]. The retrieved rainfall rate and PIA are used as the initial guess rainfall rate and an integral constraint, respectively, in 2C-RP.

### 3.3.3: 2C-RP algorithm description

Precipitation rate and liquid water content throughout the column is retrieved using an optimal estimation technique used to derive the CloudSat 2C-RP product [Mitrescu et al., 2010; Lebsock and L'Ecuyer, 2011]. The adapted algorithm seeks to minimize the cost function:

$$\Phi = [Z_{sim} - Z]^T S_Z [Z_{sim} - Z] + [x - x_a]^T S_a [x - x_a] + \frac{(PIA_{sim} - PIA)^2}{\sigma_{PIA}^2} \quad (3.1)$$

where  $Z_{sim}$  and  $PIA_{sim}$  are the simulated reflectivity profile and simulated path-integrated attenuation (determined using a multiple-scattering model, described later in this section),  $Z$  is the observed reflectivity profile,  $x_a$  is an a priori estimate of the background state,  $S_Z$  is the observational error covariance matrix,  $S_a$  is the a priori error covariance matrix,  $\sigma_{PIA}$  is the uncertainty in the PIA estimate. This cost function is minimized through Newtonian iteration to derive the precipitation rate estimate that matches the observations given the a priori and PIA constraints as well as their characteristics. Further details on the retrieval framework are covered extensively in Lebsock and L'Ecuyer (2011).

Simulated reflectivities are generated by assuming Mie scattering (for W-band reflectivity) to an assumed drop-size distribution (DSD), where reflectivity is related to liquid water content (LWC) and precipitation rate. We assume a DSD following Abel and Boutle (2012). The Abel and Boutle (2012) DSD is represented

by an exponential function; and, when compared to other DSD parameterizations, results in more realistic rainfall rates typically observed in StCu clouds. We acknowledge that, given the high vertical resolution of this data, considerable DSD variability will exist in individual profiles. Though we do not address the sensitivity of this method to the assumed DSD in this study, the availability of multiple collocated radar frequencies will make the direct retrieval of DSDs possible and will be the topic of future studies. Unlike approaches that utilize Z-R relationships, 2C-RP accounts for non-Rayleigh scattering, models multiple scattering, and mitigates non-uniqueness caused by strong attenuation at W-band through the a priori and PIA terms [L'Ecuyer and Stephens, 2002].

It is possible for W-band radar observations to be entirely attenuated in heavy rainfall, but this generally only occurs when the precipitation rate exceeds 5 mm/hr [Battaglia and Simmer, 2008]. These conditions rarely occurred during the ORACLES field deployment but were observed frequently in trade cumulus on the transit flights and in cumulus observed near the equator during ORACLES 2017. Multiple scattering (MS) is modeled following Hogan and Battaglia (2008). Though multiple scattering is often insignificant for airborne radar observations of warm rain systems, some heavily precipitating shallow cumulus observed during ORACLES 2017 generated large attenuation and MS may have occasionally occurred. However, MS is generally negligible for the vast majority of APR-3 profiles due to the radar's much narrower field of view compared to CloudSat. Evaporation below cloud base is modeled following Comstock et al. (2004) and Feingold (1993). The

algorithm typically iterates 5-10 times before converging on a solution (i.e. a LWC profile).

Finally, surface and profile precipitation rate are computed from LWC assuming the fall-speed relationship according to Gunn and Kinzer (1949). Following this algorithm, typical uncertainties in instantaneous single-pixel precipitation rate are usually on the order of 100 to 150% for precipitation rates more than 0.1 mm/hr, with higher uncertainty (often above 200%) for much lower rates. Fig. 3.3 presents an example of an APR-3 W-band rainfall retrieval for the convective cell shown in Fig. 3.2. Between 40 km and 60 km from the beginning of the scan, where thin StCu is present, measured reflectivities of -20 dBZ to -10 dBZ correspond to retrieved liquid water content (LWC) values between 0.005 and 0.01 g/m<sup>3</sup>. Light precipitation is occurring between 21 and 28 km, with surface rainfall rates peaking at around 0.1 mm hr<sup>-1</sup>. The maximum attenuation corrected profiles in these columns peak at between 20-25 dBZ, which closely matches the reflectivity measured at Ka-band in Fig. 3.2. In some profiles, the corresponding LWC values become very large due to the magnification of errors as the algorithm corrects reflectivity lower in the profile [Hitschfield and Borden, 1954]. Regardless, the retrieved surface rainfall rates remain reasonable given that the surface attenuation-corrected reflectivities are typically between -10 and 5 dBZ.

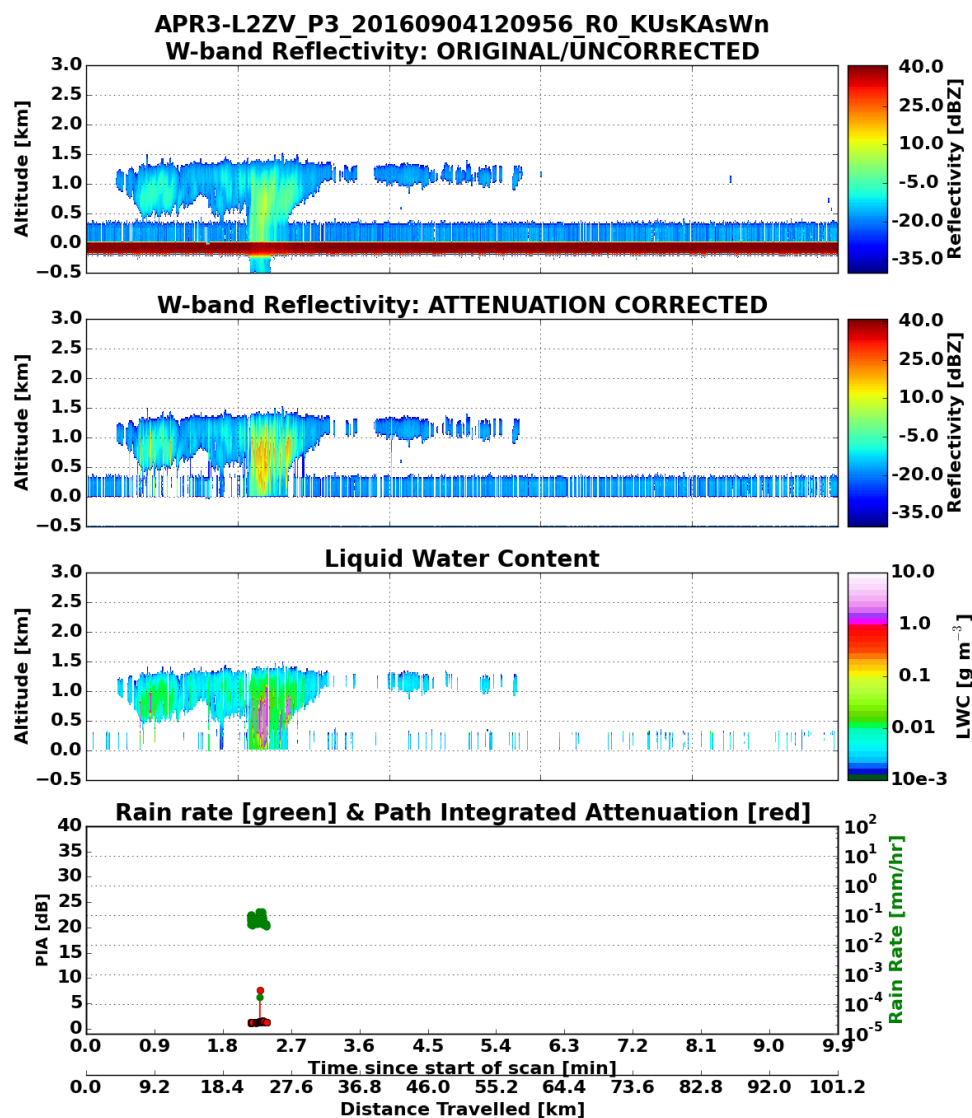


**Figure 3.3:** As in Figure 3.2, but with W-band reflectivity (top), attenuation-corrected reflectivity (top-middle), liquid water content (bottom-middle) and surface rain rate and path-integrated attenuation (bottom), where the attenuation-corrected reflectivity, LWC, PIA and surface rain rate are derived from 2C-RP. Rain rate and PIA are plotted only where a valid cloud top above 200 meters is found, the retrievals are *high confidence*, and certain rain is present.

#### 3.3.4: Estimated inversion strength

A large number of metrics could be implemented to account for meteorological controls and context, and will be the topic of other ORACLES related

studies. For this work, we adopt Estimated Inversion Strength (EIS), which describes the strength of the inversion above the PBL by accounting for temperatures at 700 hPa and the surface [Wood and Bretherton, 2006]. EIS is computed as:

$$EIS = LTS - \Gamma_m^{850}(z_{700} - LCL) \quad (3.2)$$

Where LTS is the lower tropospheric stability or the difference in potential temperature between 700 hPa and the surface,  $\Gamma_m^{850}$  is the moist adiabatic lapse rate at 850 hPa, and LCL is the lifting condensation level. We use ERA-I data to compute EIS. A table of both EIS and LTS, averaged over the first, third and fifth quintiles (i.e. beginning 20%, middle 20%, and last 20%) of each flight are provided in the Appendix.

### 3.4: Summary of Clouds and Precipitation

APR-3 data collected during ORACLES 2016 and 2017 reveal unique cloud and precipitation characteristics with respect to each campaign. An exhaustive summary of cloud and precipitation data collected by the APR-3 and featured in the 2C-RAIN dataset can be found in Tables 3.3 and 3.4 (2016 and 2017 respectively). For all analysis in the remaining sections, we use only valid radar profiles, where a valid radar profile is defined as:

- I. Occurring during a *level* flight leg, where a level flight leg is defined as a time when the aircraft pitch, drift and roll angles are all less than 3 degrees.

- II. Cloud top altitude is greater than 200 meters, which is approximately the lowest altitude before ground clutter contamination becomes an issue.

For all analysis involving estimates of precipitation intensity, we further restrict our analysis using the following flags, which follow the descriptions found in the CloudSat 2C-RAIN-PROFILE product manual [Lebsock 2011]:

- I. Precipitation flag of 1 (i.e. certain rain or drizzle, lower uncertainty) or 3 (i.e. likely drizzle, higher uncertainty, see below).
- II. Status flag of 0 (i.e. rain rate estimates from 2C-RP only).
- III. Quality flag of 4 (i.e. high quality retrieval).

Retrieved rain rates from profiles with a precipitation flag of 3 typically have much higher uncertainties than those with a precipitation flag of 1. Profiles with a precipitation flag of 3 are included because excluding them would result in grossly underestimated rain fraction statistics due to the vast number of weakly drizzling profiles collected during both experiments.

The next two subsections highlight interesting cloud and precipitation characteristics for specific research flights, as well as similarities among selected research flights from each campaign. A *routine flight* in 2016 references any flight track between Walvis Bay, Namibia and approximately 0 degrees longitude and 10 degrees south latitude (0°E, 10°S), while any *routine flight* in 2017 implies a flight from São Tomé along the 5°E longitude line. A *circuit* or “*suitcase*” flight refers to any series of flights between Namibia/ São Tomé and Ascension Island (the latter being located at 14.35°W and 7.94°S), respective to the campaign year, where the first

flight ends at Ascension Island and the last flight ends at Namibia/ São Tomé. The aforementioned coordinates will be referred to as the “turnaround point” with respect to each campaign hereafter. A summary of the APR-3 data collected (i.e. when the APR-3 was operating) along each flight track for 2016 and 2017 is shown in Fig. 3.4.

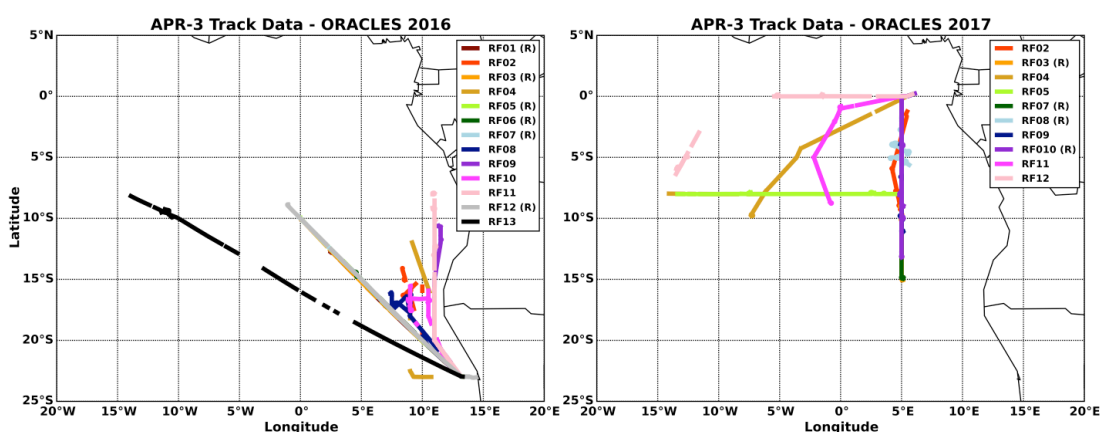


**Figure 3.4:** APR-3 data collection lines from the 2016 (left) and 2017 (right) campaigns. The (R) denotation represents flights that approximately followed the routine flight track for that campaign year and thus overlap one another.

#### 3.4.1: Summary of ORACLES 2016

The first research flight (RF hereafter) of ORACLES 2016 took place on 31 August 2016. Stratocumulus clouds persisted from the coast to the turnaround point with some StCu exhibiting a more distinct cellular structure closer to the target point. Near the coast during the beginning of the flight, EIS exceeded 11 K but decreased to 6.4 K out at the turnaround point [Fig. 3.5]. Clouds were observed in 85% of all W-band radar measurements (Table 3.3) and most precipitation rates



**Table 3.3:** Daily rainfall statistics for ORACLES 2016. The number of cloudy profiles refers to any *valid* profile where the aircraft was flying a level leg (i.e. a pitch, drift and roll angle of less than 3 degrees) and detected a valid reflectivity profile after noise removal (described in the text). A rejected profile refers to any radar profile that either saw clear skies or was collected during a non-level flight leg. The cloud fraction column includes only APR-3 W-band nadir data. The percent of cloudy profiles with virga or surface rainfall account for *valid* cloudy-sky profiles only. The five columns from the right account for only profiles where surface rainfall was present.

	Date	Cloud Top Height (mean +/- std)	# Cloudy Profiles (# Rejected Profiles)	Overall Cloud Fraction (%)	% of Cloudy Profiles w/ Virga	% of Cloudy Profiles w/ Surface Rainfall	Light Drizzle (<0.01 mm/hr)	Moderate Drizzle (0.01 to 0.1 mm/hr)	Heavy Drizzle (0.1 to 1.0 mm/hr)	Rain (1.0 to 5.0 mm/hr)	Heavy Rain (>5.0 mm/hr)
RF01	31-Aug-16	0.94 +/- 0.39 km	9733 (159392)	84.61%	16.74%	21.46%	52.99%	32.17%	11.54%	1.48%	0.62%
RF02	02-Sep-16	0.99 +/- 0.18 km	40702 (105610)	99.16%	4.08%	71.93%	37.87%	55.21%	4.56%	0.52%	1.23%
RF03	04-Sep-16	0.95 +/- 0.22 km	110793 (198645)	79.50%	21.26%	47.99%	66.59%	32.04%	1.34%	0.02%	0.01%
RF04	06-Sep-16	0.86 +/- 0.16 km	14504 (166717)	77.10%	3.41%	67.75%	64.46%	30.01%	5.29%	0.17%	0.06%
RF05	08-Sep-16	0.84 +/- 0.42 km	16269 (342208)	44.65%	17.17%	34.54%	93.29%	5.64%	1.01%	0.05%	0.00%
RF06	10-Sep-16	1.21 +/- 0.23 km	5382 (214132)	44.08%	44.00%	25.49%	62.39%	33.16%	9.48%	1.75%	1.38%
RF07	12-Sep-16	1.13 +/- 0.27 km	66542 (250391)	77.00%	30.23%	18.27%	76.46%	21.39%	2.07%	0.04%	0.03%
RF08	14-Sep-16	0.86 +/- 0.09 km	7347 (339770)	81.90%	8.09%	29.21%	88.44%	9.74%	1.21%	0.61%	0.00%
RF09	18-Sep-16	0.86 +/- 0.27 km	1596 (183456)	67.06%	4.74%	7.39%	66.95%	15.25%	0.85%	6.78%	5.93%
RF10	20-Sep-16	0.57 +/- 0.07 km	8869 (231713)	82.44%	3.51%	41.99%	86.11%	11.41%	0.67%	0.19%	0.26%
RF11	24-Sep-16	0.98 +/- 0.21 km	20374 (400020)	68.50%	25.86%	51.30%	47.21%	51.47%	1.22%	0.01%	0.04%
RF12	25-Sep-16	1.03 +/- 0.17 km	100211 (443338)	96.80%	50.03%	7.40%	59.48%	28.30%	10.81%	0.70%	0.36%
RF13	27-Sep-16	1.11 +/- 0.18 km	7673 (230505)	59.11%	49.16%	44.12%	21.77%	27.83%	17.93%	19.97%	11.31%
TOTAL			409995 (3265897)		30.55%	34.33%	60.05%	35.00%	3.43%	0.71%	0.59%

The second RF, taking place 02 September 2016, featured over 99% cloud fraction estimated by the W-band – the highest for the campaign. Nearly 72% of all cloudy profiles were observed to be precipitating. A distinct upper level low over the central South Atlantic, which formed on 01 September 2016, began building north and east on this day. Although RF02 took place mostly near the coast, a transition from a mostly homogeneous StCu deck (i.e. a cloud deck with no distinct open- or closed- cell structure apparent) to a closed-cell StCu deck became more apparent. By 04 September 2016 (RF03), the aforementioned low had begun to weaken but moved east of the prime meridian, resulting in the least dynamically stable day of the entire campaign. This is evident in satellite imagery (not shown) showing that the StCu deck did not extend further than about 8E on 04 September 2016. The turnaround point was mostly devoid of cloud, which is manifested in the APR-3 lower observed cloud fraction relative to RF01 four days prior. The combined virga and rain fraction for RF03 was also much higher than that of RF01.

By 06 September 2016 (RF04), the StCu deck recovered over much of the SE Atlantic basin. Much of the StCu present this day was closed-cell with a similar cloud fraction as RF03 but with a higher rain fraction. Interestingly, precipitation rates (Table 3.3, columns 7-9) are quite similar between these two flights, though greater percentages of heavy drizzle, light rain, and heavy rain are noted for RF04.

Research flights 05, 06 and 07 followed the routine flight track, observing nearly the same curtain in the SE Atlantic Ocean over a period of five days. For RF05 on 08 September 2016, the StCu deck thinned out under very stable conditions with EIS exceeding 9 K for the entire flight (see Table 1 in the Appendix section). Cloud

fraction, rain fraction and overall intensity dramatically decreased between this flight and RF04 two days earlier. RF06 had similar stability conditions, although open-cell StCu was more apparent on this day. RF07 also had similar EIS, with values of 8.5 K or higher frequently occurring. This flight was different from RFs 05 and 06 in that 77% of profiles from RF07 had observable cloud cover, compared to around 44% for RFs 05 and 06. The frequency of virga was highest for RF06, but the fraction of precipitating profiles gradually decreased from 34.5% on RF05 to 18.3% on RF07.

The next series of flights, RFs 08, 09 and 10, all took place near the coast. Despite the APR-3 collecting at least 180,000 profiles from each of these flights, fewer than 10,000 profiles satisfied the filtering criteria. On 14 September 2016 (RF08), the APR-3 observed perhaps the most homogeneous StCu cloud deck of the entire campaign: the standard deviation of cloud top altitudes was only 0.09 km. Between RFs 09 and 10, the mean cloud top altitude decreased from 0.86 km to 0.57 km between the two days with the standard deviation of cloud top altitudes decreasing from 0.27 km to 0.07 km. This was likely due to most of the measurements being collected south of 15°S, where SSTs were cooler (not shown) and thus more conducive for a shallower PBL. All three flights had virga fractions of less than 9%, and the majority of surface precipitation intensities were less than 0.01 mm/hr.

A suitcase flight took place 24-25 September 2016 (RFs 11 and 12). These two flights were among the most successful for APR-3 data collection, with the 25 September 2016 flight featuring the highest collection of valid 2C-RP surface

precipitation data. Cloud top altitudes were very similar to the mean, varying by only 0.05 km between the two days. W-band derived cloud fraction increased substantially from RF11 to RF12 (69% to 97%) but precipitation frequency dramatically decreased from 51% to 7%. Given the decrease in moderate drizzle from RF11 to larger percentages of light drizzle and heavy drizzle in RF12, and noting that many clouds were observed in the same portion of the basin, we suspect StCu cloud dissipation was occurring. This idea will be the topic of future research, since we do not fully investigate temporal changes in cloud and precipitation processes during either experiment.

The final research flight of the 2016 campaign (RF13) featured the largest percentages of heavy drizzle and rain – evidenced by frequent W-band attenuation (not shown) and significant radar returns in the Ka- and sometimes the Ku- band. Most of these cases are from convective cumulus near Ascension Island.

#### *3.4.2: Summary of ORACLES 2017*

APR-3 data collection for the ORACLES 2017 campaign began with research flights 02 and 03 (15 and 17 August 2017). RF02 featured one of the lowest rain fractions of the campaign with only 6.6% of cloudy, level legs precipitating. RF03 had a very similar cloud fraction (45.6% compared to 46.7% from RF02) yet only 2.5% of all profiles were precipitating. Nearly all of the precipitating profiles collected during this day contain either light or moderate drizzle (Table 3.4). A comparison of satellite imagery from between these two days shows a slight

southward retreat of the StCu deck, with many more instances of open-cell StCu observed during RF03.

**Table 3.4:** As in Table 3, but for ORACLES 2017.

	Date	Cloud Top Height (mean +/- std)	# Cloudy Profiles (# Rejected Profiles)	Overall Cloud Fraction (%)	% of Cloudy Profiles w/ Virga	% of Cloudy Profiles w/ Surface Rainfall	Light Drizzle (<0.01 mm/hr)	Moderate Drizzle (0.01 to 0.1 mm/hr)	Heavy Drizzle (0.1 to 1.0 mm/hr)	Rain (1.0 to 5.0 mm/hr)	Heavy Rain (>5.0 to mm/hr)
RF01	12-Aug-17	N/A	N/A	N/A	N/A	N/A	N/A	N/A	N/A	N/A	N/A
RF02	13-Aug-17	1.32 +/- 0.24 km	61961 (490216)	46.74%	69.71%	6.60%	50.41%	29.88%	3.91%	9.39%	6.38%
RF03	15-Aug-17	1.12 +/- 0.12 km	57890 (426529)	45.60%	34.70%	2.45%	72.99%	26.38%	0.63%	0.00%	0.00%
RF04	17-Aug-17	1.63 +/- 0.31 km	36857 (602037)	23.08%	60.19%	9.21%	69.00%	23.78%	3.04%	2.03%	1.52%
RF05	18-Aug-17	1.45 +/- 0.47 km	4419 (319207)	11.77%	38.59%	27.36%	49.88%	38.13%	5.71%	1.82%	3.48%
RF06	19-Aug-17	N/A	N/A	N/A	N/A	N/A	N/A	N/A	N/A	N/A	N/A
RF07	21-Aug-17	1.13 +/- 0.26 km	53230 (521967)	40.17%	45.32%	12.27%	58.08%	35.85%	3.93%	1.52%	0.53%
RF08	24-Aug-17	1.60 +/- 0.67 km	73071 (376320)	55.27%	43.69%	5.85%	27.80%	8.57%	12.77%	6.86%	41.72%
RF09	26-Aug-17	1.28 +/- 0.38 km	16695 (631397)	25.12%	42.48%	29.68%	52.19%	25.45%	7.04%	5.37%	9.88%
RF10	28-Aug-17	1.36 +/- 0.36 km	82104 (833139)	53.55%	38.43%	26.37%	46.53%	47.17%	5.94%	0.27%	0.05%
RF11	30-Aug-17	1.28 +/- 0.17 km	174202 (762926)	61.36%	59.28%	15.77%	42.17%	39.93%	14.28%	1.81%	1.60%
RF12	31-Aug-17	1.49 +/- 0.18 km	10708 (617743)	46.41%	50.63%	7.96%	34.98%	44.60%	19.01%	0.59%	0.82%
<b>TOTAL</b>			604822 (5581481)		51.38%	13.28%	46.89%	37.44%	9.05%	2.23%	4.11%

The next three flights (RF04, RF05 and RF07, 17 Aug. 2017, 18 Aug. 2017 and 21 Aug 2017) were a series of flights taking place from São Tomé to Ascension Island and back, with RF05 beginning and ending at Ascension Island. The flight path for RF04 skirted along the northwestern flank of the cloud deck and StCu to Cu transition zone (Fig. 3.4), which is likely why the APR-3 only estimated a 23.1% cloud fraction. Cloud top heights during RF04 were also the highest of the 2017 campaign, with a mean cloud top altitude of 1.63 km. Overall, 9.2% of the valid profiles were precipitating with many of these profiles being light drizzle with precipitation rates under 0.01 mm/hr. The StCu deck expanded northward in time for RF05, however, only about 4400 out of the approximately 319,000 collected profiles (or ~1%) were valid. RF05 featured the lowest cloud fraction estimate (11.8%) observed by the APR-3 during the 2017 campaign. RF07 saw both an increase in estimated cloud fraction (40.2%) and rain fraction (12.3%) with the second lowest mean cloud top altitude (1.13 km) for the 2017 campaign. The majority of the measurements were taken in the StCu deck along 8°S and the northern part of the routine flight track along 5°E. Even though the StCu deck on this day appeared to contain more open-cell StCu compared to the other days, close to 94% of the precipitation rate estimates fell in the light/moderate drizzle categories rather than in the heavy drizzle or rain categories.

RF08, taking place on 24 August 2017, contained arguably the most diverse range of cloud and precipitation characteristics. The APR-3 estimated a mean cloud top altitude of 1.6 km and a cloud top standard deviation of approximately 0.7 km. The observed rain fraction on this day was especially diverse, with 28%, 13% and

42% of surface precipitation rates in the light drizzle, heavy drizzle and heavy rain categories, respectively. RF09, by comparison, was a target of opportunity flight that only reached about 6°S. The cloud deck was fairly expansive and homogeneous on this day, but similar to RF05, the aircraft only flew into the northernmost portion of the cloud deck and hence the APR-3 estimated a lower cloud fraction of 25.1%. A notable number of profiles were collected near the equator that measured heavy drizzle or rain, accounting for about 22% of precipitating profiles for RF09.

The final routine flight of the 2017 campaign took place on 28 August 2017. RF10 had a similar rain fraction as RF08 but had over double the cloud fraction. Most of the profiles collected during this day were in a mostly closed-cell StCu deck, with a mean cloud top altitude around 1.36 km. Close to 26.4% of level, cloudy-sky profiles were precipitating and over 93% of these profiles were either in the light or moderate drizzle categories.

The final two flights, RFs 11 and 12 on 30 and 31 August 2017 respectively, were a pair of target of opportunity flights designed such that RF12 would re-sample clouds and aerosols from RF11. The APR-3 observed over 170,000 valid cloudy sky profiles during RF11, which was the most of the 2017 campaign. Over 80% of surface precipitation rates were in the light or moderate categories, yet a large number of heavy drizzle cases (14.3%) were collected too. The next flight, RF12, followed a track further north and west compared to RF11. The StCu deck slightly retreated to the south and east, with much of the deck appearing more open-cell in character. Both cloud and rain fractions were much lower in RF12 than RF11 although a larger percentage of moderate and heavy drizzle cases were taken.

### 3.5: Discussion

Addressing ORACLES primary science objectives, which include assessing cloud morphology and precipitation trends in the SE Atlantic StCu deck, requires accurate knowledge of the *environmental* regimes sampled during each research flight. Using EIS as a crude proxy for local thermodynamic conditions, significantly different conditions prevailed during the 2016 and 2017 campaigns.

Throughout the 2016 campaign, EIS was strong near the coast (east of 10°E), often exceeding 11 K from the central Namibian coast through the Namibia/Angola border [Fig. 3.6]. EIS decreased to about 6 K at the turnaround point for routine flights. By comparison, only the middle portions of RF04 and RF10 had an EIS  $\geq 5$  K during the entire 2017 campaign. West of 0°E during 2016, EIS sometimes decreased below 4 K during certain flights where a larger number of light to heavy rain scenes were observed (e.g. RF13 with the largest percentage of rain or heavy rain cases, see Table 3.3). The middle of RF11, as well as the end of RFs 12 and 13, occurred when EIS was near its lowest values for the campaign (Fig. 3.5). In contrast, the entirety of research flights 2, 4, 6, 7 and 8 (for 2016) occurred in regimes where EIS exceeded 8 K, representing a very stable lower troposphere and strong inversion. While this analysis suggests clear geographic variability in EIS during each year, we again cannot make conclusions at this time that *temporal* variability in EIS was primarily responsible for the observed differences in cloud and precipitation characteristics.

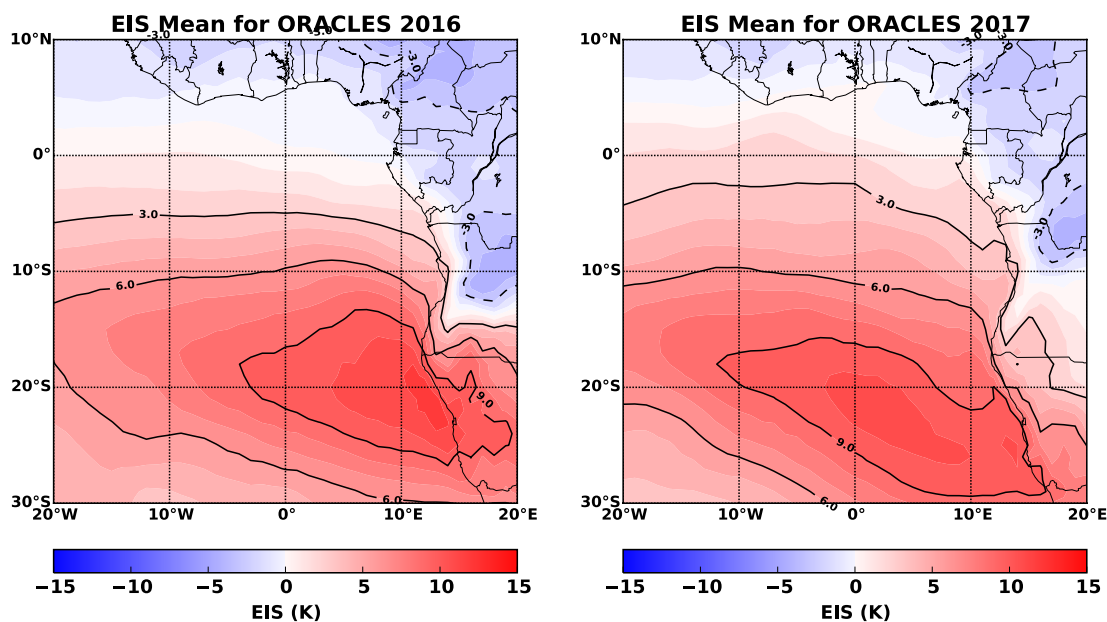


**Figure 3.6:** Mean daytime estimated inversion strength (EIS) for the ORACLES 2016 (left) and 2017 (right) campaigns. EIS is computed from ERA-I reanalysis data following the methodology outlined in Wood and Bretherton (2006). To assure daytime-only data are used, 12 UTC data are used in this figure.

Differences in cloud fraction and structure were noted during both campaigns. During the 2016 campaign, cloud top altitudes varied from approximately 0.80 to 0.90 km near the Namibian coast to higher than 1.30 km at the turnaround point (Fig. 3.7A). Many cloud top altitudes exceeded 1 km altitude (sometimes higher than 1.4 km) in 2017. The increase in cloud top altitude is associated with an increase in PBL depth west of the African coast, which is in turn associated with a gradient in sea surface temperatures (PBL depth is especially shallow near the African coast due to coastal upwelling). Cloud depths (Fig. 3.7) estimated from the APR-3 (with cloud base being defined as the lowest altitude with a valid reflectivity measurement) were typically a few hundred meters. The cloud

fraction from each flight in 2016 typically agreed with climatological values of cloud fraction over the primary experiment area [e.g. Fig. 5 in Adebisi et al., 2015]. Cloud fraction estimates during 2017, by contrast, were lower than climatology for most flights. The most common reflectivity measurements taken by the W-band radar were between -20 and -10 dBZ and typically occurred below 1 km (Fig. 3.8), further showing that many of the observed StCu clouds were typically a couple hundred meters thick. Only trade cumulus observed near Ascension Island and close to the equator account for any cloud top altitudes above 2 km. The results shown in Fig. 3.8 corroborate previous findings [e.g. Liu et al. 2015] that many StCu measurements occur in CloudSat's blind zone, which is about 720 meters above ground level.

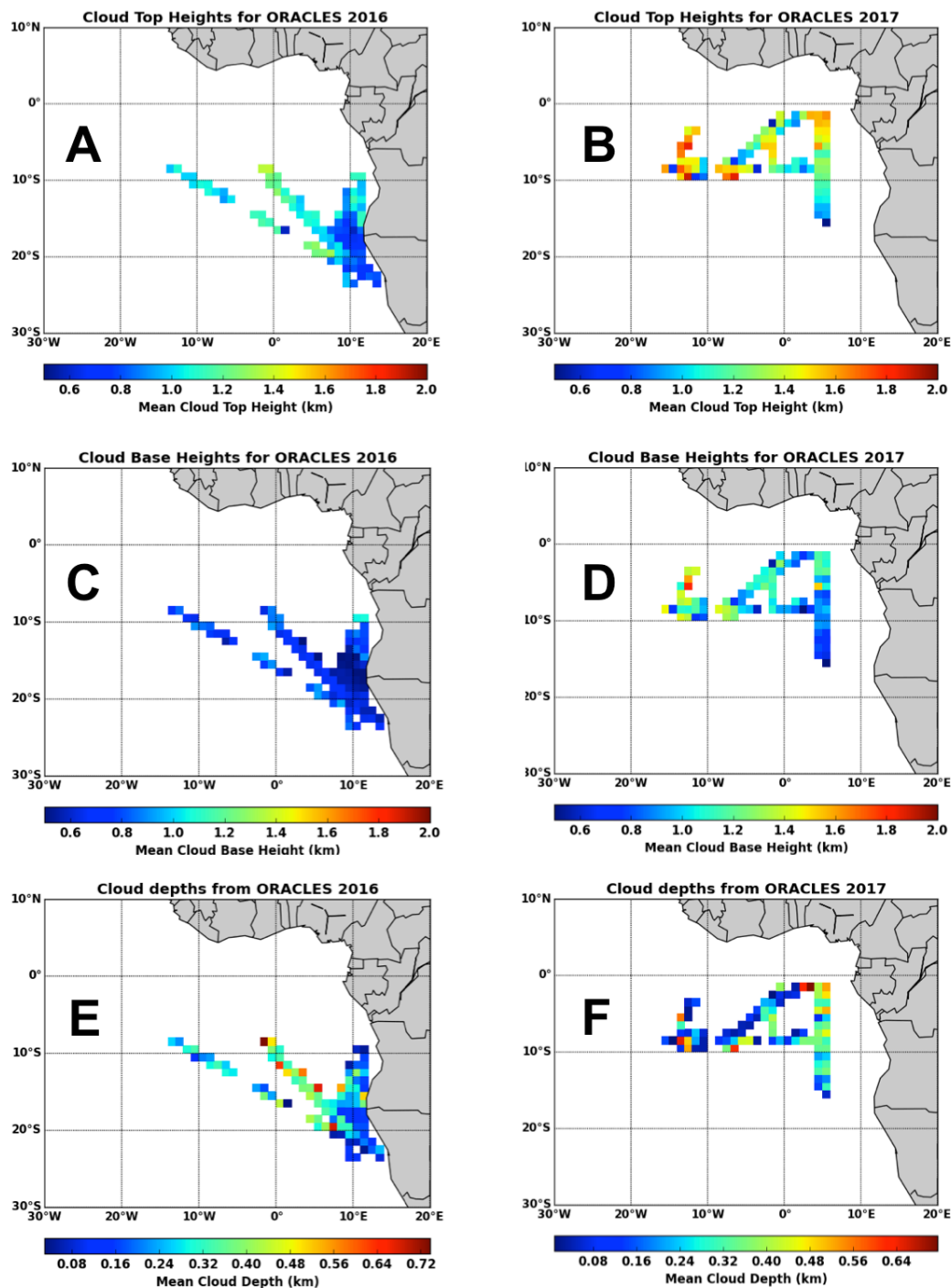


**Figure 3.7:** APR-3 W-band estimated cloud top altitudes (2016, A; 2017, B), cloud base altitudes (2016, C; 2017, D) and cloud depths (2016, E; 2017, F) in the SE Atlantic basin. Cloud depth is the difference between cloud top altitude and cloud base altitude, with cloud base altitude assumed to be the lowest altitude in the cloud

with a valid radar reflectivity measurement. Data are binned according to 1x1 degree latitude/longitude boxes.

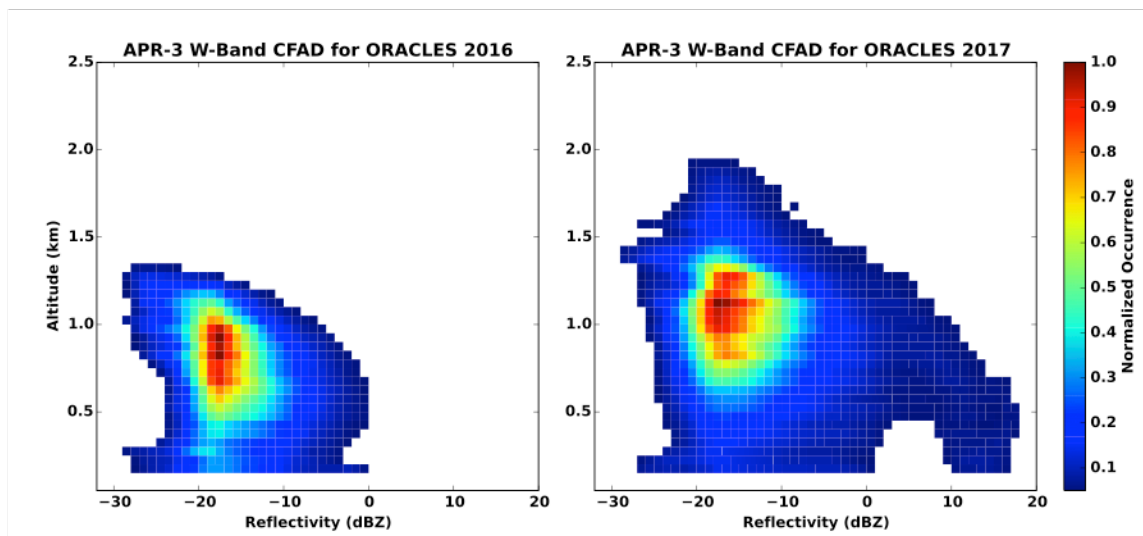


**Figure 3.8:** Normalized frequency by altitude diagram of attenuation-corrected W-band reflectivity measurements for ORACLES 2016 (left) and 2017 (right).

Precipitation statistics for the ORACLES 2016 and 2017 campaigns are summarized in Fig. 3.9. For all valid cloudy profiles, approximately 35% of all profiles are not precipitating for both campaigns, and over 98% (2016) and 93% (2017) of precipitating profiles have surface precipitation rates of less than 1.0 mm/hr (Fig. 3.9). The mode of observed precipitation rates of less than 0.1 mm/hr are consistent with estimates found in other observational [e.g. Austin et al., 1995] and modeling [e.g. Stevens et al., 1998] studies. In general, we find approximately 34% of all observed cloudy profiles contained surface precipitation in 2016, whereas only 13% of profiles included surface precipitation in 2017. Rain fraction estimates for both years are somewhat higher than those found in previous climatological studies utilizing CloudSat (e.g. Fig. 3 in Ellis et al., 2009; Fig. 4 in Kay

et al., 2018), where these studies found observed rain fraction estimates between 0.04 to 0.12. Given that most observations in 2017 were taken further north and west in the SE Atlantic Ocean and in environments where EIS was (on average) several degrees less, and noting that more rain rates above 1 mm/hr were also observed, we suspect the APR-3 observed more open-cell StCu during this year.

Temporal variability is more difficult to evaluate using ORACLES observations and is not addressed in this study. During ORACLES 2016 and 2017, clouds and precipitation are observed throughout the morning and afternoon portions of the diurnal cycle. One avenue to potentially address the temporal evolution of clouds and precipitation would involve the analysis of “square spiral” flight pattern data, which exist for most research flights. In these flight legs, the APR-3 collected data along four distinct descending but level “walls” and was measured over the course of about 10 minutes. In-cloud observations in at least one of these walls often succeeded the conclusion of the square spiral descent further presenting a possible avenue for validating retrieved water contents and rainfall rates against in-situ derived rainfall rates from cloud probe data. The opportunities for such analyses are, however, quite limited since the clouds sampled earlier in a flight will not necessarily represent conditions observed later in a flight. The assessment of temporal variability in clouds and precipitation during the ORACLES experiment, validation of the retrieval products, and subsequent analysis on cloud-aerosol-precipitation interactions are beyond the scope of the present study but will be the topic of future investigation.

### 3.6: Conclusions

This paper summarizes the macrophysical character of clouds and precipitation observed during ORACLES 2016 and 2017 based on rainfall rate retrievals from APR-3 W-band radar observations. With vertical resolution as high as 8.3 meters and over 10 million profiles taken between the two campaigns, this dataset offers an extensive airborne radar dataset for studying StCu clouds and warm precipitation processes over the southeast Atlantic Ocean. The high sensitivity of the APR-3 W-band provides accurate depictions of rainfall frequency and cloud fraction. Utilizing an optimal estimation algorithm – with robust physics and accounting of all relevant sources of uncertainty – mitigates a number of challenges associated with quantifying precipitation rates from attenuating radars though uncertainties in the precipitation *intensity* estimates can be large owing to the single-frequency nature of the retrieval.

Even though the rain fraction for 2016 was more than twice that observed in 2017, the combined virga plus conditional rain rates between both campaigns are strikingly similar (Fig. 3.9) at approximately 65%. This number may be biased a bit high due to the fact that the APR-3 W-band lacked sensitivity to the thinnest clouds observed by other collocated remote sensors, and will be explored in future work. In general, we find no obvious trends when comparing cloud fraction with rain and virga fraction between the two campaigns. Surface rainfall intensity, however, generally increases west of the African coast. APR-3 estimated cloud fraction also generally decreases away from the coast for both years, and given how rainfall intensity changes away from the coast as well, this finding is consistent with the

presence of more open-cell StCu forming in a deeper planetary boundary layer. Of the 10 million profiles collected between the two campaigns, over one million of these profiles satisfied our validation criteria.

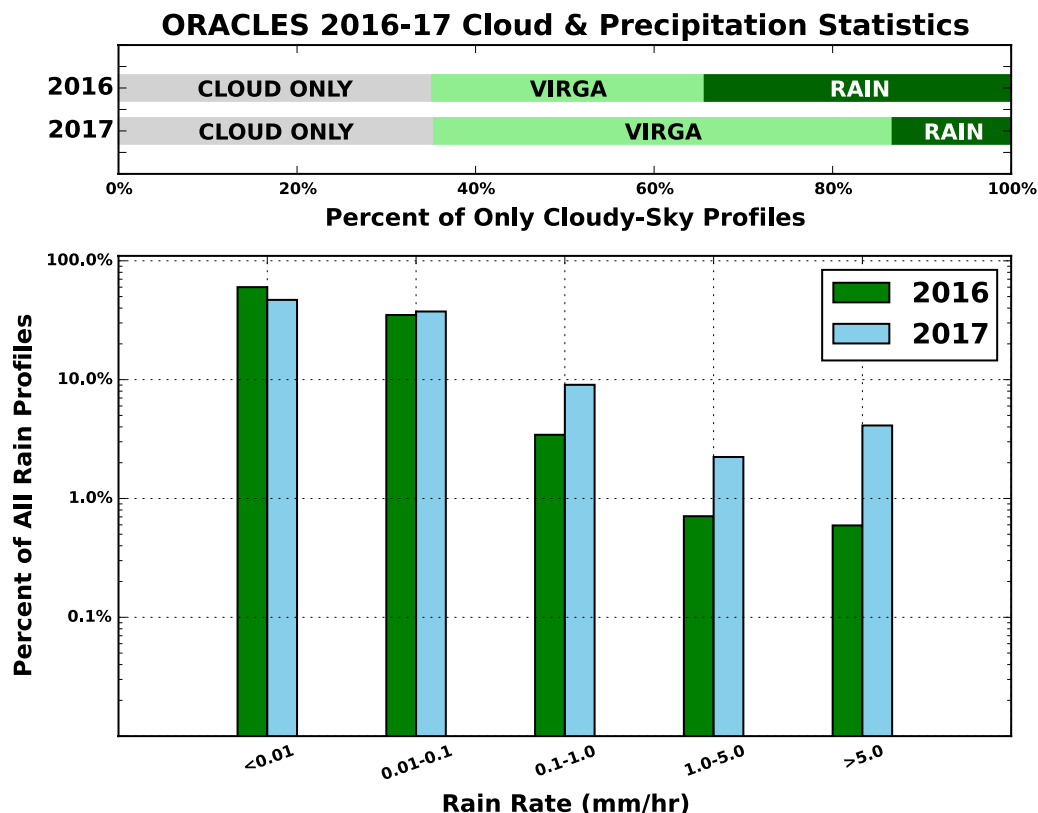


**Figure 3.9:** ORACLES 2016 and 2017 campaign cloud-only (gray), virga-only (light green) and drizzling/raining profiles (dark green) for *all* cloudy sky profiles (top panel) where the aircraft was flying at nadir. Retrieved rainfall rates for all drizzling or raining profiles for 2016 (green) and 2017 (blue) are binned by intensity (bottom panel). CLOUD represents the fraction of all cloudy sky profiles that did not have virga nor precipitation, and VIRGA represents the fraction of all cloudy profiles with a maximum reflectivity of -15 dBZ or greater anywhere in the column.

EIS was high (exceeding 8-10 K) near the Namibian coast throughout much of the ORACLES 2016 campaign and decreased by, on average, 4 K at the routine flight turnaround marker. Most of the research flights in 2017 flew in environments where EIS was, on average, 5 K or less. This results in lower mean cloud top altitudes near the coast in 2016 (0.8-0.9 km) compared to upwards of 1.3 km further west in 2016 and for most cases in 2017. For 2017, EIS generally increased from near 1-2 K to above 4 K at the routine flight turnaround point as well as the turnaround point for various target of opportunity flights. We note that SST and LTS variability in the SE Atlantic, especially in the StCu to Cu transition region, are important controls on cloud top altitude and will require further investigation. Given the environmental stability differences between the two campaigns as well as the geographical differences in cloud top altitudes and structure, the vast quantity of data available will enable extensive study of cloud-aerosol-precipitation interactions in distinct environments.

These results highlight only a fraction of the interesting data collected during ORACLES 2016 and 2017. In addition to providing valuable insights into cloud-aerosol interactions in this unique environment, in-situ data collected during both campaigns can be used to define instrument requirements for future satellite missions, validate retrieval algorithm assumptions and evaluate their impact on liquid water content and above-surface precipitation rate retrievals. These analyses will be critical toward ensuring accurate assessments of cloud-aerosol interactions as they relate to cloud and precipitation processes, and toward improving future spaceborne satellite radar missions.

## **Chapter 4: Using retrieved cloud and precipitation properties to assess precipitation susceptibility**

The retrieval product used for this study is a W-band plus cloud optical depth algorithm (referred to as WCOD hereafter), employing APR-3 W-band data and RSP cloud data from their polarimetric retrievals [Alexandrov et al., 2011]. A CWP retrieval for the ORACLES dataset stems from a need to synergize the cloud and precipitation datasets for studying aerosol indirect effects. Cloud water path retrievals via an optical depth constraint have been successfully done before using collocated passive radiometric and cloud/precipitation radar data [e.g. Lebsock and L'Ecuyer, 2011; Mace et al., 2016; Leinonen et al., 2018]. The joint retrieval of CWP and RWP, along with precipitation rate, and data from the HSRL-2 enable a comprehensive remote sensing-based study of precipitation suppression in SE Atlantic StCu clouds. This chapter expands upon the framework presented in Chapter 3 by rigorously evaluating the new (and updated) uncertainties with this updated technique, and then uses this newly created dataset in an attempt to quantify the magnitude of precipitation suppression via the presence of aerosols.

### **4.1: Multi-measurement retrievals**

Following the results and conclusions discussed in Chapter 3, the 2C-RAIN product [Dzambo et al., 2019] highlights the utility of the APR-3 toward investigating cloud-aerosol-precipitation interactions. To fully assess the aerosol indirect effect, especially as related to the level 3 ORACLES science objectives

(discussed in Chapter 1), a synergy between measurement platforms remains necessary due to the complexity of the indirect effect problem [Zuidema et al., 2016] and the promise such algorithms have toward retrieving simultaneous cloud and precipitation properties [Mace et al., 2016]. Field campaigns such as ORACLES mitigate uncertainties that were otherwise impossible to avoid in spaceborne-data based studies. For example, limited observations of shallow marine StCu by CloudSat led the Mace et al. (2016) study to study mostly shallow convection with their highest LWC above  $\sim 1$  km in altitude. Simultaneous retrievals of cloud and precipitation properties, however, have been challenging. Another study by Mace et al. (2016) found that, in CloudSat profiles with significant precipitation, the uncertainties in their assumptions led to forward model uncertainties greater than that of the a priori constraint.

It is worth re-emphasizing that the APR-3 was designed to validate spaceborne radar (i.e. the TRMM PR and the CloudSat CPR). Multi-measurement retrievals from airborne platforms, such as the NASA P-3 during ORACLES, allow for robust analyses using adapted cloud and precipitation retrieval algorithms. This concept is expanded upon in this chapter by employing RSP passive radiometric cloud measurements with APR-3 high-resolution profiles of rain water content, allowing for robust joint cloud-precipitation property retrievals.

## **4.2: Datasets**

This study synergizes the APR-3, RSP and HSRL-2 datasets. In Section 4.3, the 2C-RAIN algorithm is updated to include an optical depth constraint for the retrieval

of cloud water path. A comprehensive analysis of retrieval performance will include only retrievals from collocated APR-3 and RSP measurements: a total of 28 flights corresponding to 5 (2016), 10 (2017) and 13 (2018) flights during the respective campaign years (see Chapter 2, Table 2.1). Any valid W-band radar data has a corresponding 2C-RAIN retrieval data product even in the absence of a COD estimate. As stated earlier, precipitation rates are insensitive to CWP (this will be shown later) thus remain useful provided the user abides to the flagging procedure outlined in Chapter 3. Finally, this analysis focuses on retrievals where collocated APR-3, RSP and HSRL-2 measurements exist. For all cases, RSP and HSRL-2 data are interpolated in time to match the time resolution of the APR-3.

### 4.3: Algorithm mechanics

#### 4.3.1: Forward models

The WCOD algorithm (i.e. version 2.0 of 2C-RAIN from Chapter 3) estimates both cloud and precipitation properties from available ORACLES data. The mechanics very closely follow those outlined in Lebsock and L'Ecuyer (2011), which used CloudSat W-band radar reflectivity measurements and a cloud optical depth constraint from MODIS to solve for precipitation rate and cloud water path. As such, The WCOD algorithm uses a profile of reflectivity measurements ( $Z$ ), a COD ( $\tau$ ) and PIA constraints:

$$Y = [Z_1, Z_2, \dots, Z_N, \tau, PIA] \quad (4.1)$$

To solve for a profile rainfall rates ( $R$ ) and a cloud water path ( $CWP$ ):

$$X = [R_1, R_2, \dots, R_N, CWP] \quad (4.2)$$

Where the subscript N represents the total number of reflectivity measurements, and  $R_N$  is the rainfall rate at the surface. The algorithm attempts to minimize a cost function:

$$\begin{aligned} \Phi(X, X_a, Z) = & [F(R) - Z]^T S_Z^{-1} [F(R) - Z] + \\ & [(X - X_a)^T S_a^{-1} (X - X_a)] + \\ & \frac{(\tau_{mod} - \tau)^2}{\sigma_\tau^2} + \frac{(PIA_{mod} - PIA)^2}{\sigma_{PIA}^2} \end{aligned} \quad (4.3)$$

Where X represents the retrieved precipitation rates and CWP while  $X_a$  represent the a priori precipitation rates and CWP. The last two terms on the right hand side of Eq. 4.3 are the integral constraints from the observed COD and PIA. If the visible optical depth observed by the RSP includes contributions from CWC and RWC, i.e.:

$$\tau_{mod} = \frac{3Q_{ext}}{4\rho_w} \int_{H_{bot}}^{H_{top}} \left( \frac{CWC}{r_{e,cld}} + \frac{RWC}{r_{e,pcp}} \right) dz \quad (4.4)$$

On the right hand side of Eq. 4.3,  $\rho_w$  is the density of liquid water,  $Q_{ext}$  is the extinction efficiency (set to 2) and  $r_{e,cld}$  and  $r_{e,pcp}$  are the effective radii corresponding to the cloud and rain water contents. Equation 4.4 supplies the physical model for the optical depth constraint in Eq. 4.3.

#### 4.3.2: Observation and model uncertainties

The data availability from ORACLES enables finer tuning of several key assumptions made in the initial 2C-RAIN product. First, PIA is estimated by taking the difference between  $\sigma_0$  in a given radar profile and the observed  $\sigma_0$  in a nearby clear-sky profile. Enabling such a change eliminates the need for the look-up table

(LUT) of clear-sky  $\sigma_0$  and also has the added benefit of fixing the measurement uncertainty to that of the APR-3 measurement uncertainty (1 dB). For most radar data, clear sky estimates are possible using the aforementioned technique; however, the LUT approach is employed for estimating PIA and PIA uncertainty for scenes where cloud cover exists everywhere. Second, the vertical resolution of the radar and the added  $\tau$  constraint allow CWP to be appropriately distributed through the observed cloud. In LL11 and Dzambo et al. (2019), cloud water content was parameterized following Equation 10 in LL11 and assumed CWC was homogeneous with altitude. This algorithm instead assumes that the cloud base altitude occurs at the altitude of maximum reflectivity, and all CWP is distributed from the top of the cloud down to this altitude. During ORACLES, the maximum radar reflectivity sometimes occurs at or near cloud top, meaning the entire CWP would be distributed into the top 1-3 radar bins and result in unreasonably large CWCs. To circumvent this potential problem, the following logic is applied to ensure a reasonable distribution of CWC through the cloud:

1. If the depth of the cloud spans 6 or fewer radar bins, the entire CWP is distributed through the cloud regardless of what the maximum reflectivity is.
2. If the maximum reflectivity occurs near cloud top, but the cloud spans 6 or more radar bins, the CWP is distributed through the top 6 radar bins.
3. If the reflectivity profile spans more than 6 bins, and the maximum reflectivity occurs below the 6<sup>th</sup> bin, CWP is distributed from the cloud top to the altitude of maximum reflectivity.

Once the above logic is satisfied, the distribution of CWP follows Bennartz (2007) and other studies which suggested that cloud water content (CWC) increases by a factor of 1/3 vertically, i.e.:

$$CWC \propto H^{\frac{1}{3}} \quad (4.5)$$

$$CWP = \int_{H_{bot}}^{H_{top}} CWC(z) dz \quad (4.6)$$

Where H is the in-cloud altitude. Preliminary results from ORACLES show that CWC increases height approximately following Eq. 4.5, though entrainment near the cloud top can result in CWC becoming constant or decreasing with altitude at the top of the cloud [Siddhant Gupta, personal communication]. With this in mind, and noting that it cannot be fully determined whether CWC is always constant (despite not being true most of the time), this source of uncertainty is accounted for in the CWP retrieval. In other words, CWP could be modeled as either:

$$CWP = \gamma_{ad} \tau_c \rho_w r_e \quad (4.7)$$

$$CWP = \gamma_{mono} \tau_c \rho_w r_e \quad (4.8)$$

Where  $\gamma_{ad}$  in Eq. 4.7 is valid for cases when CWC increases with altitude in cloud (i.e. the adiabatic assumption), whereas  $\gamma_{mono}$  is valid if the cloud has a monodisperse drop distribution. Lebsock et al. (2011) solved for  $\gamma$  explicitly. The source of uncertainty from using the CWP assumption following Eq. 4.7 is 20%. Finally, uncertainty in the RSP effective radius (5%) accounts for the remaining uncertainty in the CWP retrieval. Uncertainty estimates of COD in regimes with LWPs due to high reflectance are unknown at this time, and not accounted for in this version of the algorithm.

To summarize, the resulting diagonal elements along the observational error covariance matrix,  $S_y$ , follows:

$$S_y(Z) = \sigma_{Z\_meas}^2 + \sigma_{att}^2 + \sigma_{Z\_DSD}^2 \quad (4.9)$$

$$S_y(\tau) = \sigma_{\tau\_meas}^2 + \sigma_{cwp}^2 + \sigma_{re}^2 \quad (4.10)$$

$$S_y(PIA) = \sigma_{PIA\_meas}^2 \quad (4.11)$$

Despite the fact that only the AB11 DSD is used (compared to two different DSDs as in LL11), the uncertainty in reflectivity remains set to 2 dB to allow for potential overestimation of the error from the DSD. Given that the APR-3 radar has collocated Ka-band and Ku-band radar channels, future versions of this algorithm could use this information as a constraint on attenuation at each level, allowing (for example) the changes in DSD parameters (e.g. slope and shape parameters) to account for  $\sigma_{Z\_DSD}^2$  instead of a constant value.

#### 4.3.3: A priori estimate

The a priori constraint, or the “first guess”, serves to keep the algorithm from retrieving unrealistic precipitation rates and CWP. As in LL11, the full profile of rainfall rates is set to a first guess of 0.1 mm/hr with a variance that extends 3 orders of magnitude around this value. The minimum and maximum retrievable precipitation rates therefore fall between  $10^{-4}$  and  $10^2$  mm/hr. Even with the suite of observations available from ORACLES, it is nearly impossible to know for sure what the a priori state might be given unknowns such as the DSD variability. The a priori constraint for CWP is somewhat easier to quantify. For this work, an adjusted adiabatic water model is used to estimate the a priori CWP constraint:

$$CWP_a = \int_{0.8H}^H z f_{ad} \Gamma_{ad} dz \quad (4.12)$$

The terms  $z$ ,  $f_{ad}$  and  $\Gamma_{ad}(T, p)$  represent the altitude in-cloud, the degree of adiabacity (1 = fully adiabatic, anything less is sub-adiabatic) and the adiabatic increase of liquid water content with height. The a priori uncertainty is set to 500 g m<sup>-2</sup> to cover the entire range of possible CWP values. The caveat of using the full radar profile for the a priori CWP estimate would result in extremely large and unrealistic CWPs, thus, the assumption is made that the a priori CWP is distributed over the top 20% of the cloud (CWP is distributed following the aforementioned logic in section 4.3.2 beginning with the 1<sup>st</sup> full retrieval iteration). Following Merk et al. (2016) the terms  $f_{ad}$  and  $\Gamma_{ad}$  are set to 0.8 (unitless) and 2.0 (g m<sup>-4</sup>) respectively. The  $\Gamma_{ad}$  term is a function of both pressure and temperature [Albrecht et al., 1990; Merk et al., 2016]; however, computing this to an exact value offers no additional value to the algorithm given the large uncertainty associated with this constraint. Lebsock et al. (2011) computed the ratio of CWP to RWP using MODIS and CloudSat data in an attempt to provide a priori boundaries for similar remote sensing retrievals. Finally, the a priori estimate of CWP in the absence of RSP cloud data does not affect any precipitation retrieval due to the precipitation retrieval's insensitivity to cloud water content (not shown).

#### 4.3.4: Contribution matrices

With any inversion technique, sources of uncertainty affect the final retrieved quantity. To assess the relative contribution of each source of uncertainty

to the retrieved rainfall rates at each level, along with the sources of uncertainty to the CWP, the contribution matrix or C-matrix to the total retrieval error covariance  $S_x$  (following L11):

$$S_x = C_{apr} + C_Z + C_\tau + C_{PIA} \quad (4.13)$$

$$C_{apr} = S_a^{-1} \quad (4.14)$$

$$C_Z = K^T S_Z^{-1} K \quad (4.15)$$

$$C_\tau = \frac{L^T L}{\sigma_\tau^2} \quad (4.16)$$

$$C_{PIA} = \frac{M^T M}{\sigma_{PIA}^2} \quad (4.17)$$

Where K, L and M are partial derivatives of reflectivity, optical depth and PIA (respectively) with respect to some perturbation. Each C-matrix is not truly a “matrix”, but rather a fractional value (between 0 and 1) derived from the error covariance matrices. A value of 1 from any of Eq. 4.14-17 implies that the entire source of uncertainty stems from that representative quantity. The improved uncertainty characterization by virtue of having high-resolution data from ORACLES offers a unique opportunity to assess the impact of each C-matrix on the final retrieved quantities and their respective uncertainties. A similar method was employed in Leinonen et al. (2018), where a multi-frequency radar technique was developed for snowfall and demonstrated the utility of ensuring their retrieved quantities were well constrained to the observations.

#### *4.3.5: Other updates to the 2C-RAIN algorithm*

One difference between the 2C-RAIN dataset discussed in Chapter 3 and the new dataset discussed here is that both the *near surface* rainfall rate and the surface rainfall rate are reported. After evaluating near-surface (i.e. at the lowest radar bin unaffected by ground clutter) rain rates compared to evaporation-corrected rain rates, very light precipitation of less than  $\sim 10^{-2}$  almost always fully evaporates in the  $\sim 200$  meters between the surface and the lowest radar bin. Figure 5 in Kalmus and Lebsock (2017) shows that the change in reflectivity drops off exponentially (i.e. much more than 3 dB) for mean drop sizes of less than 40 microns. Many W-band reflectivity profiles extended to the “blind zone” where the reflectivity at the lowest bin would often be less than -15 dBZ. The evaporation model, as a result, typically reduces the near-surface rain rate by several orders of magnitude. The exact reduction is also predicated on the other retrieval mechanics (e.g. attenuation effects on R, correlation of errors, etc.).

#### **4.4: Algorithm performance**

A total of 1.28 million collocated RSP and APR-3 profiles containing valid RSP COD and  $r_e$  and APR-3 detected cloud cover span all 3 ORACLES deployments. Retrieved precipitation rates greater than 1 mm/hr (or 24 mm/day) make up a small fraction of the total dataset, however, trade cumulus near the Equator and cumulus in the StCu-to-Cu transition region around Ascension Island often contained surface precipitation rates greater than 1 mm/hr. For the sake of demonstrating the algorithm’s performance across *all* conditions observed during ORACLES, two representative case studies are selected and presented here.

#### 4.4.1: Case study #1: trade cumulus scene

On 12 Oct. 2018, heavily precipitating trade cumulus was observed by the APR-3 along a NW-to-SE flight track just south of the Equator (Fig. 4.1). The observed W-band reflectivity exceeded 20 dBZ through many of the profiles, and experienced heavy attenuation exceeding 20 dB during the first minute of the scan. During this time, the 2C-RAIN algorithm corrects the near-surface reflectivity (from the lowest resolvable bin up to ~700 meters) by 15-25 dB. For several profiles, the propagation of errors by the algorithm results in non-retrievable solutions and are indicated by white “stripes” in the middle panels of Fig. 4.1. Also worth noting are the lack of retrieval data in the first ~10 seconds of the scan where cloud and light precipitation are present but the profile of reflectivity indicates a combination of weak “rain-out” near the surface and broken, non-contiguous vertical cloud. The modeled PIA (gray line) is also much less than the observed PIA (black line), which indicates either minimal precipitation was present or the cloud was (again) vertically incongruent.

In Fig. 4.1, five “white streaks” appear in the plots containing modeled reflectivity and RWP/RR where the algorithm did not converge on a valid precipitation rate profile. While continuous non-retrieved profiles are a small fraction of the total number of available reflectivity profiles, a non-retrieval most often occurs when there is (1) appreciable PIA greater than a few dB and (2) “virga” characteristics, or a continuous reflectivity profile far above the surface.

Optical depths observed by the RSP for this scene, with few exceptions, exceeded 20 units (of optical depth). The heaviest precipitation within the first

minute of the scan, evident in the modeled reflectivity plot and corroborated by the RWP/RR retrieved quantities, results in rain optical depths approaching 5 units. Corresponding RWP retrievals fall in the  $\sim 300\text{-}500\text{ g m}^{-2}$  range with the heaviest rain containing nearly  $800\text{ g m}^{-2}$  of RWP. The CWP associated with these heaviest rain cells are below  $\sim 100\text{ g m}^{-2}$ . Qualitatively, noting the  $20+$  dB PIA and large RWP, it is unsurprising to see the largest LWP exceed  $1000\text{ g m}^{-2}$ . Data contained in the 2<sup>nd</sup> minute of the scene showed in Fig. 4.1 tell a much different story. Total optical depths in this range generally vary between 5 and 10 units, but the much lower RWC and less than 1 dB of PIA contained in these profiles results in the total LWP being dominated by CWP. Broken cloud is evident between minutes 1.4 and 1.6, which introduce a potential source of uncertainty in the RSP COD via 3-D effects.

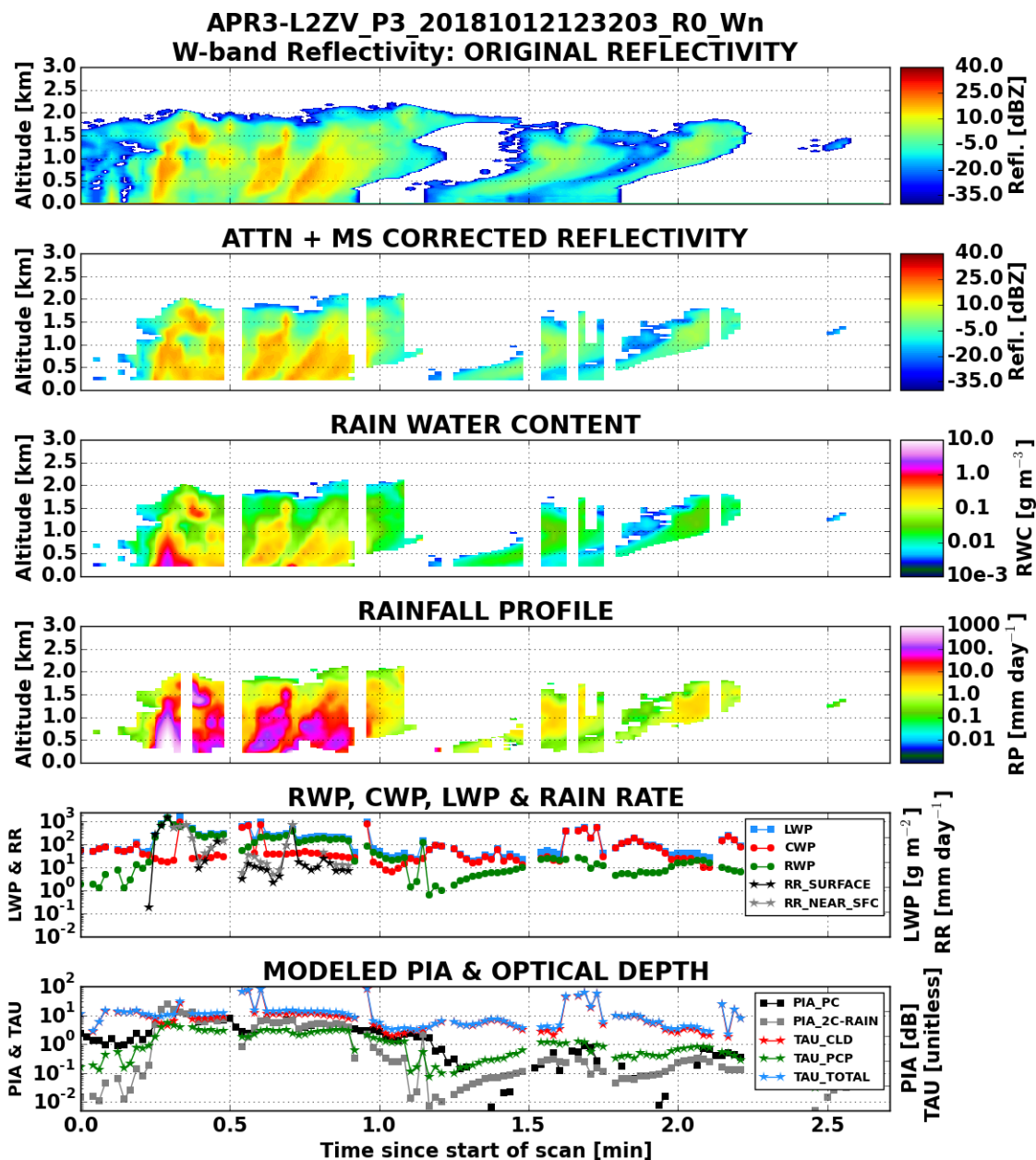


**Figure 4.1:** 2C-RAIN retrieval from a heavily precipitating trade cumulus cloud observed by the APR-3 (top) on 12 Oct. 2018. The model-corrected reflectivity (top-middle) for this scene, along with retrieved RWC (top-center) and rainfall profile (bottom-center), are also shown. The bottom two panels show retrieved water paths (cloud, rain and total; square markers), rainfall rates (surface or evaporation-corrected rainfall rate and near-surface rainfall rate; star markers), attenuation ('PC' or observed and '2C-RAIN' or modeled; square markers) and optical depths (cloud, rain and total; star markers). No quality control flags are applied to the data shown in this figure.

The mean profile of measurement contributions and a priori contributions to the retrieved rainfall rate at each level, along with the measurement and a priori contributions to the retrieved CWP, are shown in Fig. 4.2. From the main panel of Fig. 4.2, the reflectivity profile contributes the most to the final retrieved precipitation profile, with the a priori constraint contributing ~10-20% of the uncertainty in the bottom half of the profile. PIA contributes a small but non-negligible amount of uncertainty in the lowest bins (consistent with results shown in LL11). The PIA contribution often exceeds 5-10% for the largest rainfall rates (not shown) and, unsurprisingly, adds further uncertainty to near-surface rainfall rates. The bottom half of all profiles in scene have a mean precipitation rate uncertainty anywhere between 300-1000%. Near the top of the cloud, where reflectivity exclusively contributes uncertainty, the retrieved precipitation rate uncertainties hover closer to 100%.

The C-matrix allows an extra layer of quality control by filtering out profiles where 2C-RAIN relied too heavily on one component. For example, Fig 4.2 clearly shows that the a priori constraint contributed heavily to a significant number of retrieved rainfall rates, and eliminating profiles where the retrieval relied heavily on the a priori constraint would leave remaining only profiles where the final uncertainty were determined by the PIA, reflectivity and optical depth. Figure 4.3 shows how the profile of mean precipitation rate uncertainty changes when the PIA and a priori constraints are eliminated from the pool of available profiles. The mean contribution from the a priori constraint is  $< 0.05$  at all levels in this scene, however, removing profiles with the a priori constraint (any profile with an a priori

contribution  $> 0.01$ ) results in a reduction of uncertainty by factors of 2-5. Eliminating the contributions of PIA to the total uncertainty yields a minor reduction to the mean uncertainty profile but is not nearly as dramatic as when the a priori contribution is removed. Although very few heavily precipitating scenes were observed in the SE Atlantic StCu deck, Fig. 4.2 and Fig. 4.3 provide enough motivation to filter out data where the rain rate had any appreciable contribution by the a priori constraint. Because the number of profiles removed in this manner is low relative to the total number of profiles, any biases resulting from this filtering would be negligible.

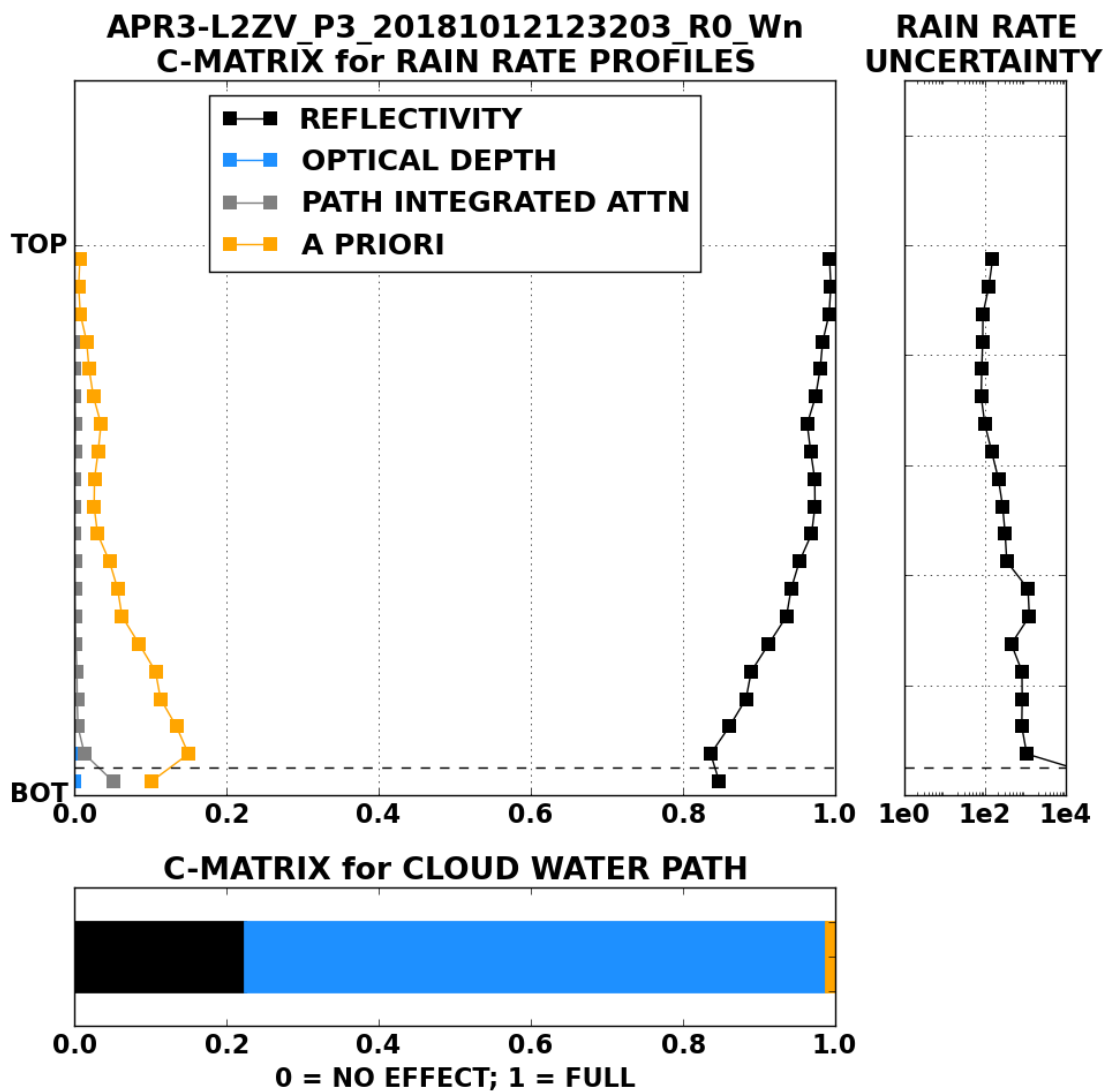


**Figure 4.2:** Mean contribution matrix (or C-matrix) calculations relative to cloud height for the radar profiles shown in Fig. 4.1. The C-matrix for each retrieved rainfall rate, as well as CWP, was calculated according to Eq. 4.13. Individual C-matrix profiles are normalized to the full length of the reflectivity profile (i.e. 0 = radar echo base, 1 = radar echo top). Data below the dashed line indicates a C-matrix calculation for both the surface (i.e. corrected for evaporation) and near-surface precipitation rates and is exactly the same for both precipitation rate quantities. In the bottom panel, the contributions from reflectivity, optical depth, PIA and a priori uncertainties are respectively shown in black, blue, gray and orange.

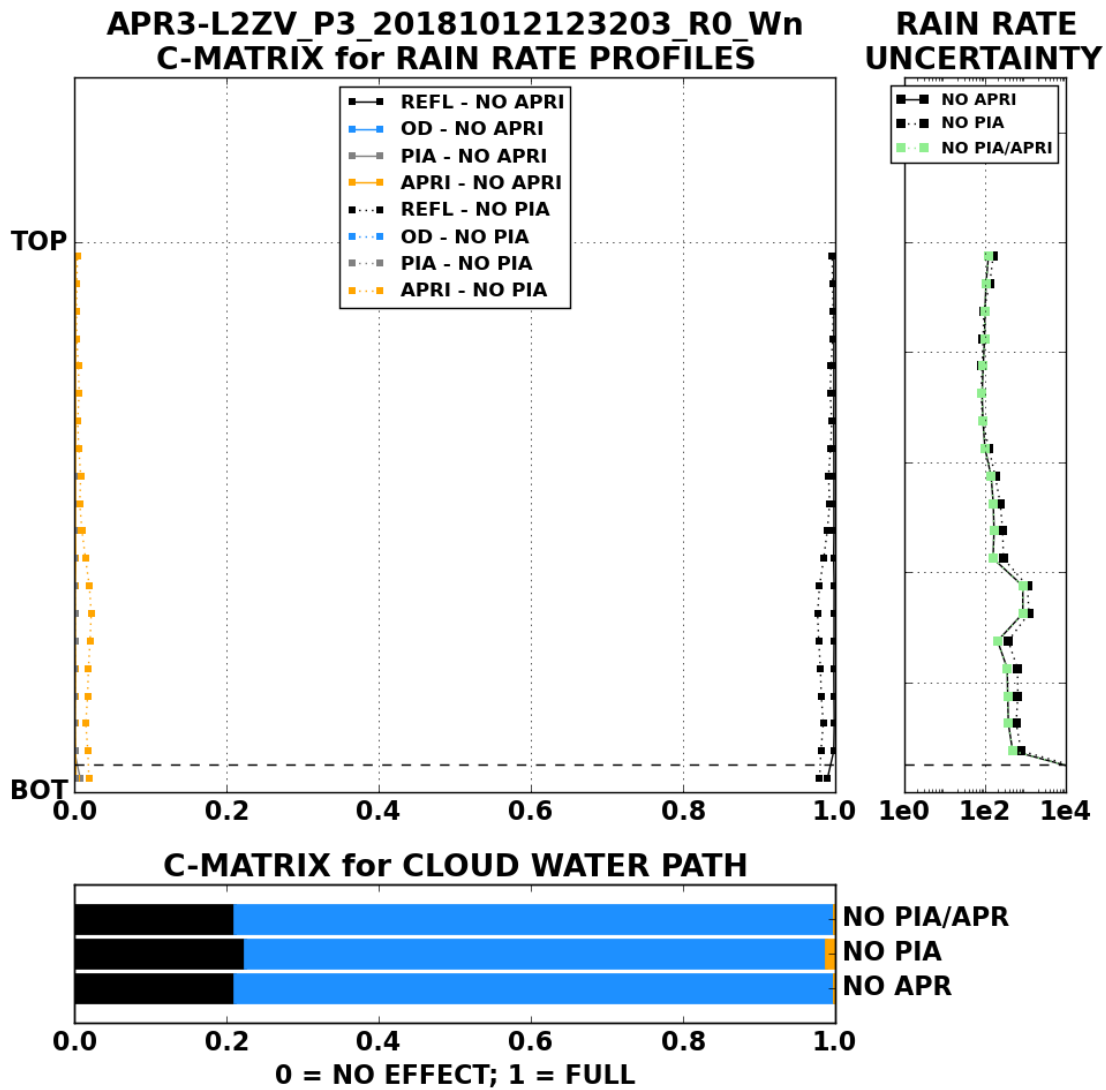


**Figure 4.3:** As in Fig. 4.2, but for profiles where the a priori constraint contributed minimal uncertainty (solid line) and profiles where the PIA contributed minimal uncertainty (dashed lines).

The sensitivity of the CWP to the reflectivity, optical depth, a priori constraint and PIA behaves differently for each constraint. As expected, optical depth contributes approximately 80% to the total uncertainty, with the reflectivity contributing the remaining 20%. The a priori constraint makes a very minimal

contribution to the CWP. Compared to the rain rates at any level, however, CWP is less sensitive to the a priori constraint. This is likely because the uncertainty associated with the CWP does not span many orders of magnitude like the uncertainties associated with precipitation rates.

#### *4.4.2: Drizzling stratocumulus scene*

The scene in Fig. 4.1 represents both a rare and extreme case from ORACLES. Figure 4.4 showcases a typical drizzling stratocumulus scene from the campaign. This scene, which spans a little over one minute, contains two drizzling cells with maximum column rain rates barely reaching  $1 \text{ mm day}^{-1}$ . Nearly every profile contains a RWP between  $0.1$  and  $10 \text{ g m}^{-2}$ . The retrieved rainfall rates also correspond well with the observed and modeled PIAs: the observed PIAs are generally less than  $\sim 2 \text{ dB}$ , leaving the vast majority of modeled PIA values well below  $1 \text{ dB}$  (recall that the uncertainty in the observed PIA is  $1 \text{ dB}$ ). The scene shown in Fig. 4.4 also showcases a nearly uniform CWP and total optical depth. As noted previously, the RSP performs best over non-broken cloud, and given that most total LWPs are under  $150 \text{ g m}^{-2}$  in this scene, the retrieved CWPs are among the most trusted and accurate with uncertainties between 25-30%.

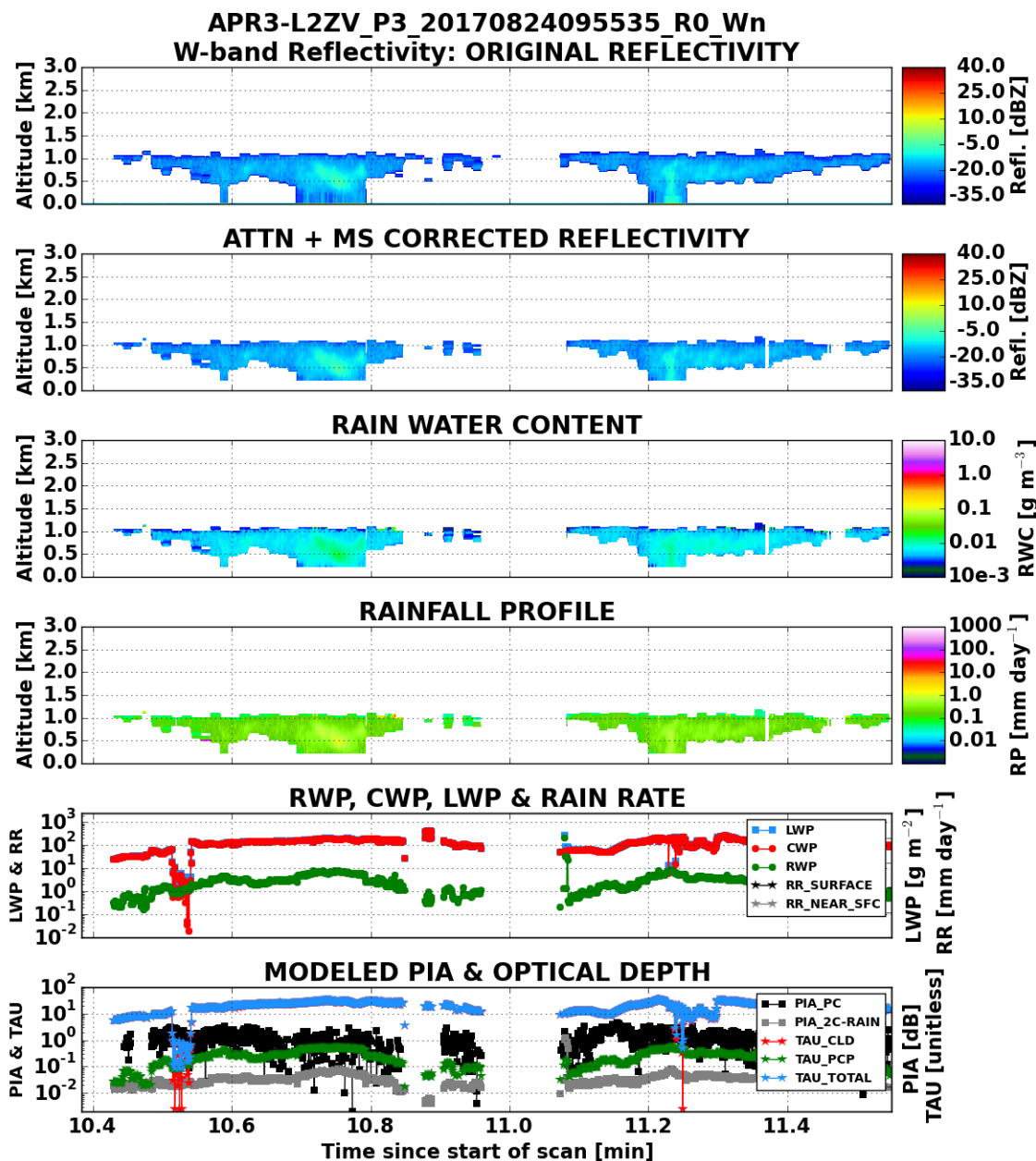


**Figure 4.4:** 2C-RAIN retrieval from lightly drizzling stratocumulus cloud observed by the APR-3 (top) on 24 Aug. 2017. The model-corrected reflectivity (top-middle) for this scene, along with retrieved RWC (top-center) and rainfall profile (bottom-center), are also shown. The bottom two panels show retrieved water paths (cloud, rain and total; square markers), rainfall rates (surface or evaporation-corrected rainfall rate and near-surface rainfall rate; star markers), attenuation ('PC' or observed and '2C-RAIN' or modeled; square markers) and optical depths (cloud, rain and total; star markers). No quality control flags are applied to the data shown

in this figure. The lower LWP and optical depth values around minute 10.5 correspond to a short period where the RSP was not operating.

The C-matrix computations and mean precipitation rate uncertainties for the weakly drizzling scene in Fig. 4.4 are given in Fig. 4.5. Unlike the heavily precipitating trade cumulus in Fig. 4.1, the uncertainty contributions to the retrieved precipitation rate profile come almost entirely from the reflectivity. This finding follows both LL11 and Lebsock et al. (2011), which found that the 2C-RAIN-PROFILE algorithm for CloudSat nearly exclusively relies on the observed reflectivity profile in the retrieved precipitation rate profile for weakly (or non-) drizzling stratocumulus. When comparing the uncertainties between Fig. 4.5 and Fig. 4.2, the uncertainty in the bottom half of the heavily precipitating profiles scale down by factors of 2-3 compared to the weakly drizzling profiles. This difference is almost assuredly due to the large attenuation propagating uncertainties deeper into the cloud [Hitschfield and Borden, 1954]. Comparing Fig. 4.5 and Fig. 4.2 also reveals very little mean contribution by the PIA, whereas the PIA contributed heavily to the retrieved precipitation rates analyzed in LL11. This could be due to one of two reasons:

1. The PIA integral constraint is not linked to the retrieved cloud water path as in Lebsock et al. (2011), and/or
2. The PIA uncertainty is manifested in the reflectivity uncertainty through the  $\sigma_{att}^2$  term, thereby distributing the (little) attenuation through the column.

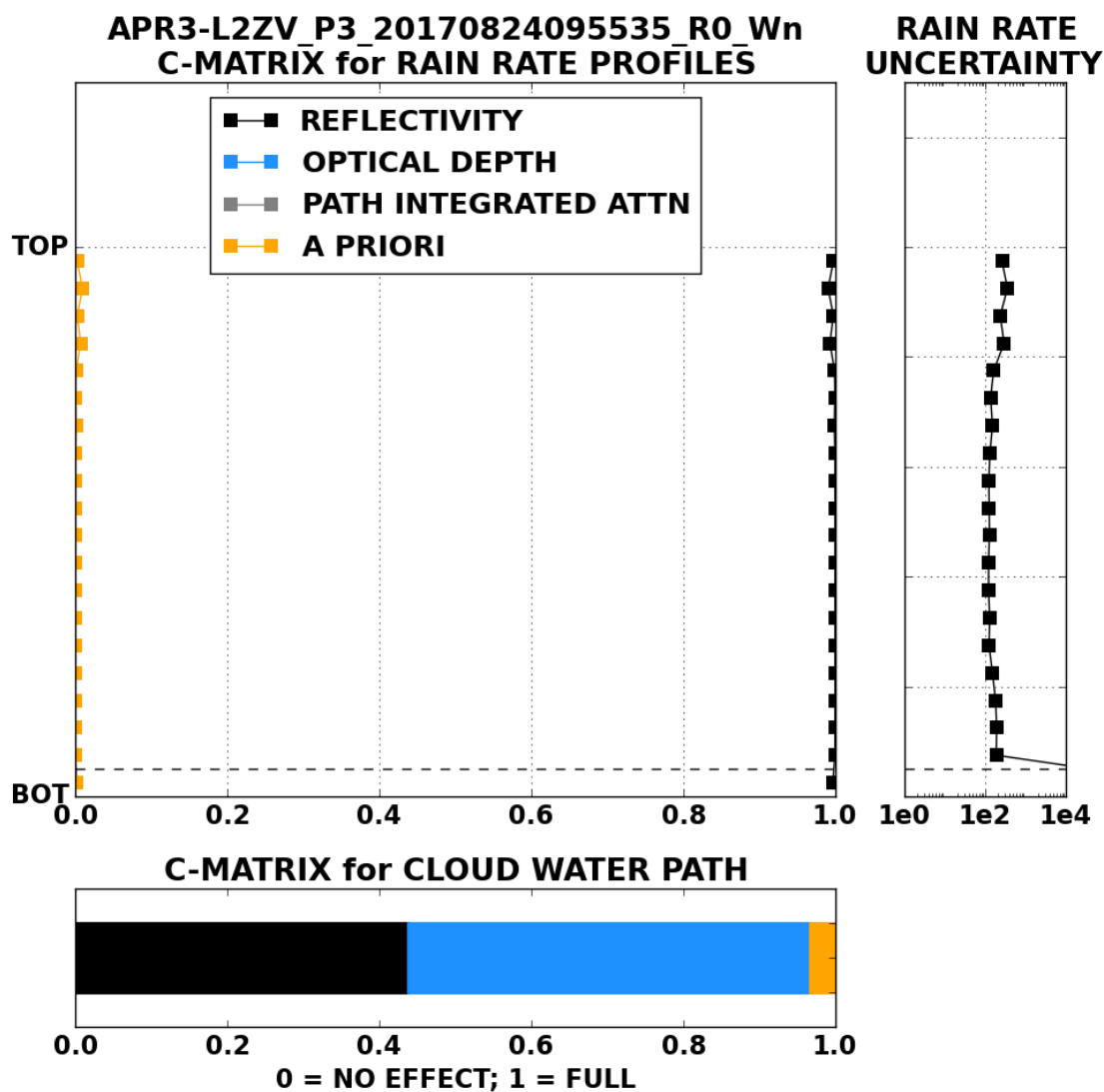


**Figure 4.5:** Mean contribution matrix (or C-matrix) calculations relative to cloud height for the radar profiles shown in Fig. 4.4. The C-matrix for each retrieved rainfall rate, as well as CWP, was calculated according to Eq. 4.13. Individual C-matrix profiles are normalized to the full length of the reflectivity profile (i.e. 0 = radar echo base, 1 = radar echo top). Data below the dashed line indicates a C-matrix calculation for both the surface (i.e. corrected for evaporation) and near-surface precipitation rates and is exactly the same for both precipitation rate quantities. In the bottom panel, the contributions from reflectivity, optical depth, PIA and a priori uncertainties are respectively shown in black, blue, gray and orange.

The contributions to the precipitation rate uncertainty are further elucidated in Fig. 4.6, which again partition profiles by the PIA and a priori C-matrices.

Removing profiles with any considerable amount of contribution by the a priori constraint results in much less of a change compared to the trade cumulus scene, though a modest mean uncertainty reduction is noted for the top-most bins. The mean uncertainties near cloud top in this scene reflect weak precipitation on the order of  $\sim 10^{-2}$  or less. The evaporation model results in complete evaporation of all near-surface precipitation rates, which is expected given the mean rain drop radius near the surface were consistently less than  $\sim 40 \mu\text{m}$  (not shown).

The C-matrix computations for CWP reveal contributions of over 0.4 by the observed reflectivity with the remaining contribution coming almost entirely from the observed optical depth. This contribution is nearly twice that observed by the trade cumulus scene, presumably because less uncertainty exists through the reflectivity profile thus mitigating uncertainty in the modeled optical depth by a large RWP. When removing profiles due to an appreciable a priori contribution, the optical depth fills in the remaining contribution to the final uncertainty. Unlike the rainfall rates, however, the a priori uncertainty does little to affect the final uncertainty in CWP, with most uncertainties falling between 25-30%. To summarize:

1. For cases when optical depth is appreciable and moderate to heavy precipitation is falling, the CWP retrieval relies more on the observed optical depth because large RWP affects the uncertainty in the optical depth more

than the reflectivity, and reflectivity is subject to both attenuation and DSD uncertainties that propagate deeper into a profile.

2. For cases in weakly or non-drizzling StCu, the uncertainty in the optical depth becomes larger relative to the uncertainty in the reflectivity due to less DSD and attenuation uncertainty (even though RWP is small), resulting in a larger contribution by the reflectivity.
3. Regardless of the case, the measured optical depth consistently contributes approximately 0.5-0.7 of the total uncertainty in any CWP retrieval.

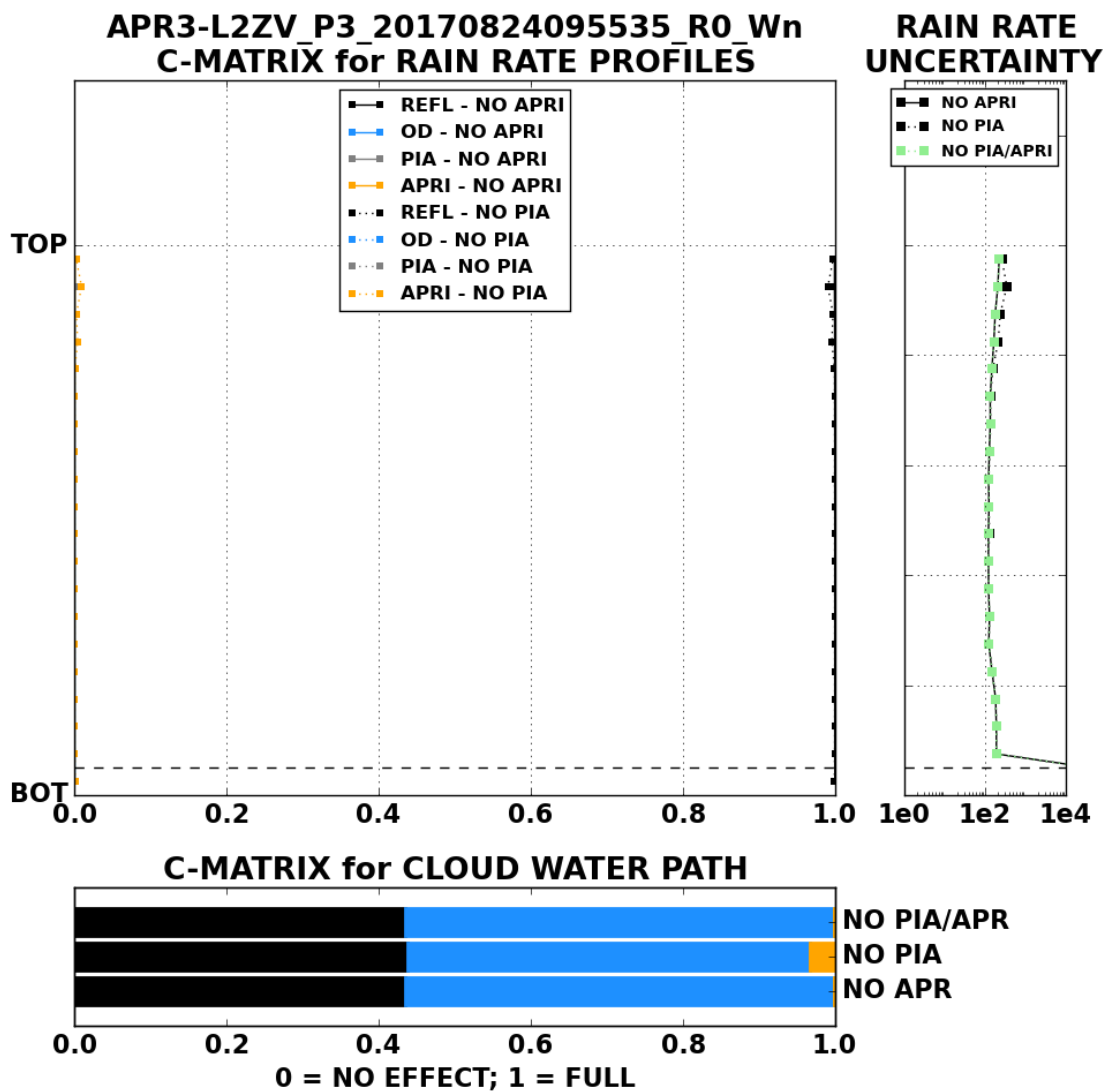


**Figure 4.6:** As in Fig. 4.5, but for profiles where the a priori constraint contributed minimal uncertainty (solid line) and profiles where the PIA contributed minimal uncertainty (dashed lines).

#### 4.5: Precipitation susceptibility

With fully characterized CWP and precipitation retrieval products generated, along with collocated HSRL-2 and RSP measurements, a comprehensive remote sensing analysis on StCu precipitation susceptibility and precipitation suppression.

As previously noted, the key advantage of using the ORACLES dataset for this analysis – specifically with the HSRL-2 – lies in the fact that the “gap” distance between the aerosol layer and StCu cloud deck can be reasonably determined. Using this fact in conjunction with the retrieved cloud and precipitation metrics, the science questions of interest (supporting SQ2 in Ch. 1) are as follows:

1. When controlling for EIS, are larger CWP estimates obtained in scenarios where the aerosol layer is touching the cloud, and if so, are they statistically significant from non-touching cases?
2. When controlling for EIS, is precipitation suppressed in scenarios when the aerosol layer is touching the cloud?
3. Accounting for uncertainties in the magnitude of rainfall rate, are statistically different rain rates observed in touching vs. non-touching scenarios?
4. What are the differences in the ratio of CWP to RWP observed between touching and non-touching scenarios?

The above science questions aim to address part of the long-standing questions on the aerosol lifetime effect.

#### *4.5.1: Gap distance definition*

The “touching vs. non-touching” framework adopted here allows for an analysis of the *likelihood* of aerosol effects on the underlying StCu cloud layer. Aerosol indirect effects cannot be fully ascertained using this framework because, without concurrent in-situ measurements for all profiles, the actual amount of aerosol in the PBL is indeterminable. Diamond et al. (2018) recently showed that

free tropospheric aerosols are very poorly correlated with MBL aerosols, implying that contact time between the aerosol layer and StCu deck along with entrainment rate must be at least considered for any indirect effect analysis. Such an analysis is difficult to perform without (for example) dropsonde data that could provide accurate moisture, temperature and wind profiles necessary for the computation of entrainment rates. To simplify this study, without introducing further ambiguity or uncertainty in any remaining results, a “gap distance” metric proxies the degree to which the aerosol layer is in contact with the cloud.

Figure 4.7 shows a full HSRL-2 curtain for the 15 Aug. 2017 research flight. Aerosol contacted the MBL throughout the entire flight, as evidenced by aerosol backscatter coefficients exceeding  $1 \text{ Mm}^{-1} \text{ Sr}^{-1}$  and above-cloud AODs exceeding 0.3 nearly everywhere. Not unsurprisingly, smoke was the primary aerosol in contact with the MBL on this day with patches of fresh smoke and dusty mix present during a few short segments on this flight. Figure 4.7 also reveals polluted-marine, marine, and dusty mix aerosols throughout the MBL. MBL aerosols are consistently observed in this fashion during ORACLES, and though not explicitly considered in this analysis, the influence of marine or polluted-marine aerosols is expected to be consistent throughout ORACLES. In any case, smoky aerosol clearly contacts the MBL for this case and thus assumed that overlying aerosols influenced underlying cloud/precipitation in some fashion.

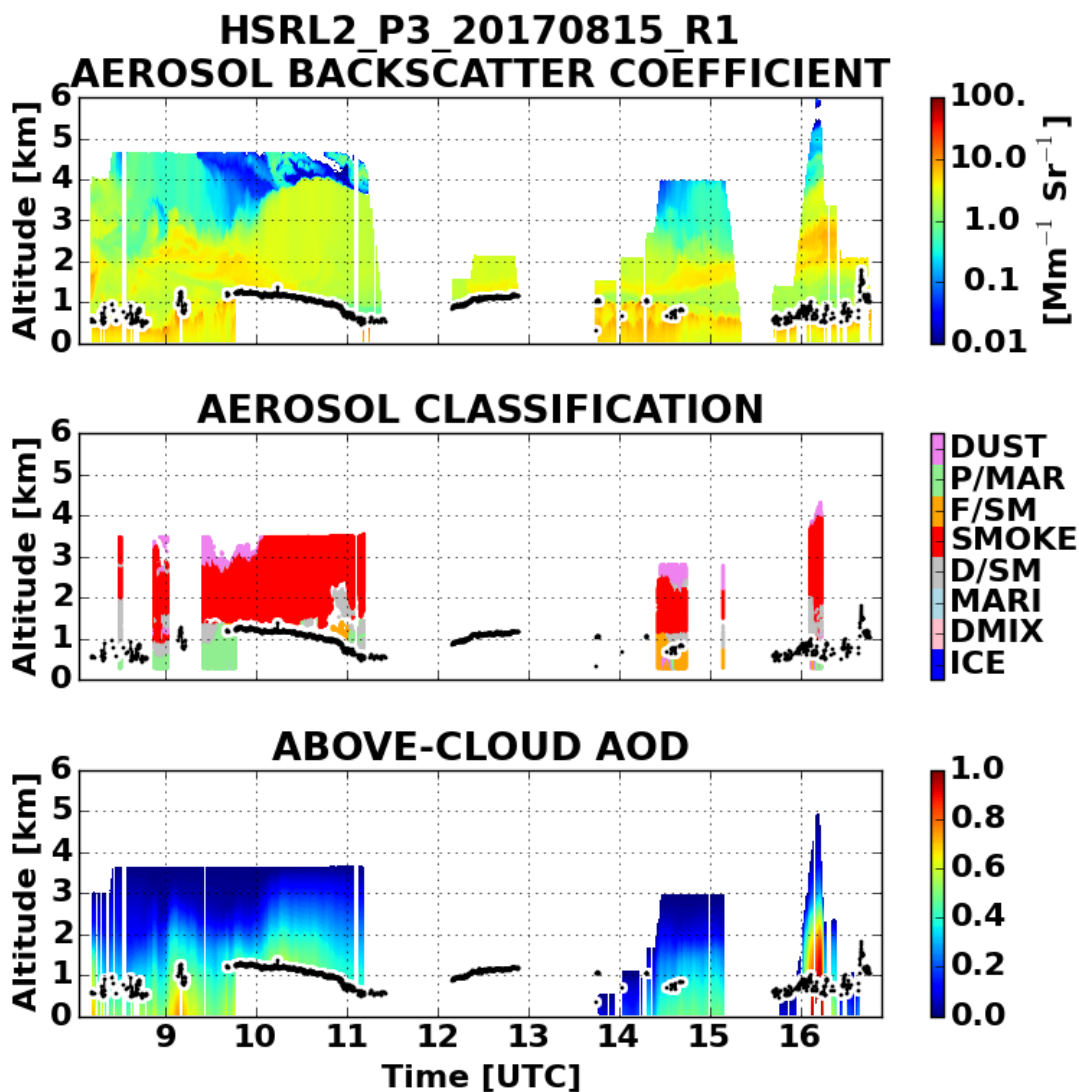


**Figure 4.7:** A full HSRL-2 curtain from the 15 Aug. 2017 research flight. The top panel shows the cloud-screened aerosol backscatter coefficient in  $\text{Mm}^{-1} \text{Sr}^{-1}$ , which proxies both the mass and volume of aerosol at a given bin and has a resolution of 15 m. The middle panel shows the aerosol classification for this curtain following Burton et al. (2012), and the bottom panel shows the above cloud aerosol optical thickness and has a range resolution of 315 m. Data in the top and bottom panels are from the 532 nm channel. Black lines indicate the cloud top altitude.

Figure 4.8 shows the HSRL-2 lidar curtain from the 17 Oct. 2018 flight.

Dubbed the “bacon-layer” case, with the 2 km aerosol backscatter coefficient

resembling a strip of bacon, the aerosol backscatter coefficient and above-cloud AOD are much less overall compared to the same metrics in Fig. 4.7. The case shown in Fig. 4.8 clearly shows aerosol-cloud gaps in the early and late flight segments. While the aerosol-cloud gap is visually obvious, quantifying the actual distance is challenging because the aerosol backscatter coefficient is almost always non-zero. To circumvent this, the above-cloud AOD can be utilized as a secondary check. Since AOD always increases away from the lidar *assuming aerosol is present in every layer*, the slope of the change of AOD with respect to altitude is exploited. Given these examples, the following criteria is used to define a cloud-aerosol gap:

1. An above-cloud AOD of 0.1 or less,
2. An above-cloud AOD slope of  $-0.05 \text{ km}^{-1}$  or greater (positive slope implies decreasing layer optical depth toward cloud), and
3. An above-cloud aerosol backscatter coefficient (BSC) of  $0.25 \text{ Mm}^{-1} \text{ Sr}^{-1}$  or less [suggested by Sharon Burton, HSRL-2 Co-Investigator, personal communication].

The first criterion of an AOD less than 0.1 mitigates uncertainties due to the aerosol semi-direct effect, even if the vast majority of aerosol is contained just above the cloud-aerosol gap. The second criterion checks the first criterion by ensuring that the bulk of the above-cloud AOD lays sufficiently above the StCu cloud deck. Finally, the last criterion ensures a negligible amount of aerosol (if any) is directly above the StCu cloud deck should the AOD or AOD slope lay just outside the bounds of their respective criterion. The selected criterion were objectively chosen and carefully considered the main concern that strictly screening data based on “no”

contact (e.g. AOD < 0.05, aerosol BSC < 0.1) would result in an overwhelming majority of cases (> 95%) classified as contacting the StCu cloud deck. Thus, results presented hereafter should be interpreted as “weak or no contact” versus “aerosol contact”. To summarize, a profile where aerosol is “not touching” implies no aerosol semi-direct nor indirect effects from the above-cloud aerosol layer, whereas a “touching” profile means the above-cloud BB aerosol layer directly contacts the StCu cloud deck. Partitioning semi-direct effects from non-touching scenes is not attempted for this work, and will be a topic of future research.

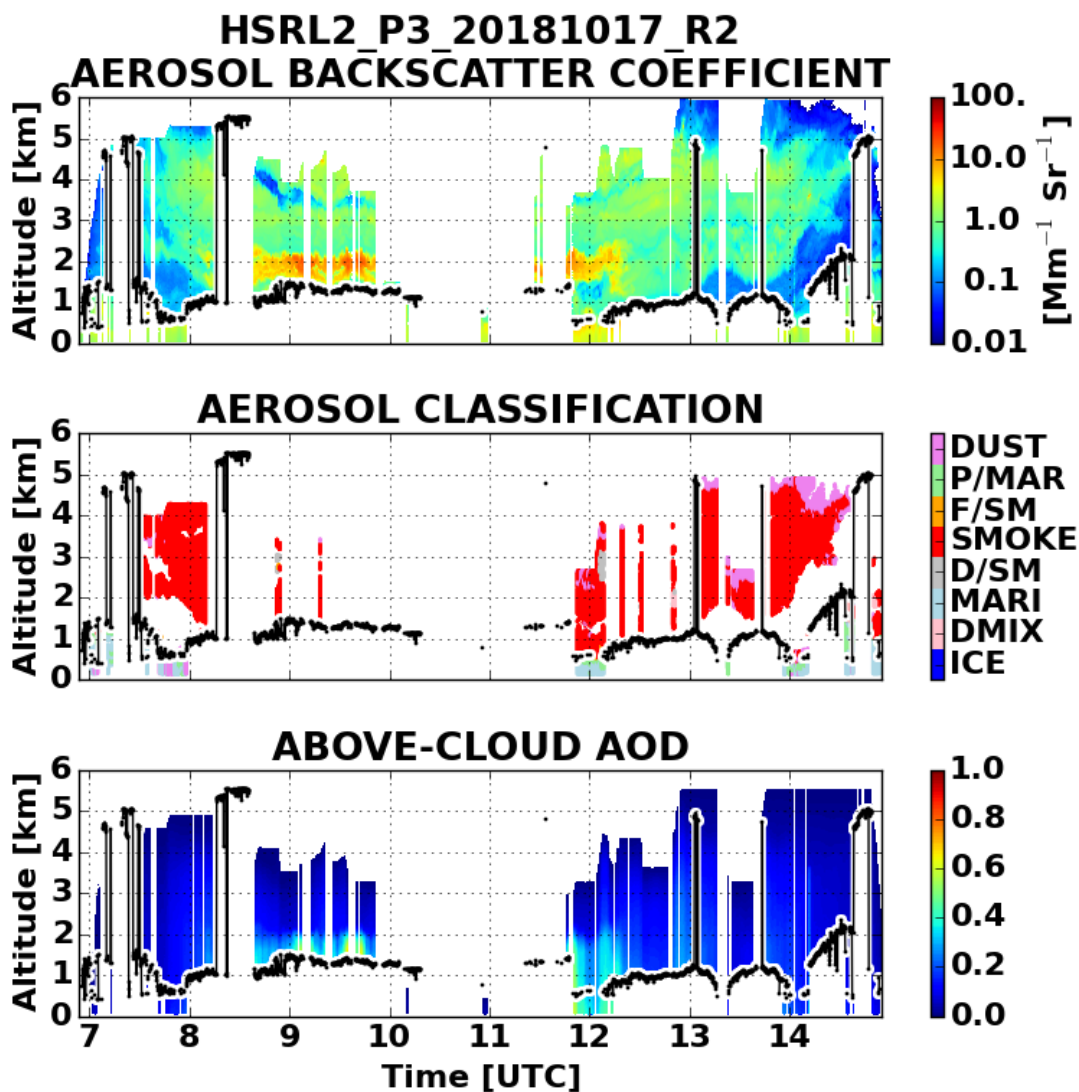


**Figure 4.8:** As in Fig. 4.7, but for the 15 Aug. 2017 research flight.

Figures 4.9 and 4.10 demonstrate the cloud-aerosol gap computations. In the case of Fig. 4.10, cloud-aerosol gaps do not exist thus revealing no positive slopes (corresponding to decreasing AOD closer to cloud top) confirm this. For all available data from the 15 Aug. 2017 research flight, the BB aerosol layer is indubitably in contact with the underlying StCu cloud layer. Conversely for the 17 Oct. 2018 research flight, aerosol BSC is fairly low everywhere with the exception of the

“bacon layer”. The above-cloud AODs, unsurprisingly, exceeds 0.5 everywhere above the bacon layer but barely exceed 0.1 to 0.2 during other flight segments. A small fraction of slopes computed from Fig. 4.8 reveal decreasing AOD closer to cloud top and roughly corresponds to the fact ~20% of all segments (near 8 UTC and 13-14 UTC) have no aerosol-cloud gap (Fig. 4.10). Prior to any collocation with the APR-3 or RSP datasets, there are 16,617 possible gaps between the 2017 and 2018 experiments, and following the aforementioned gap classification logic, 14% of these gaps qualify as non-contact.

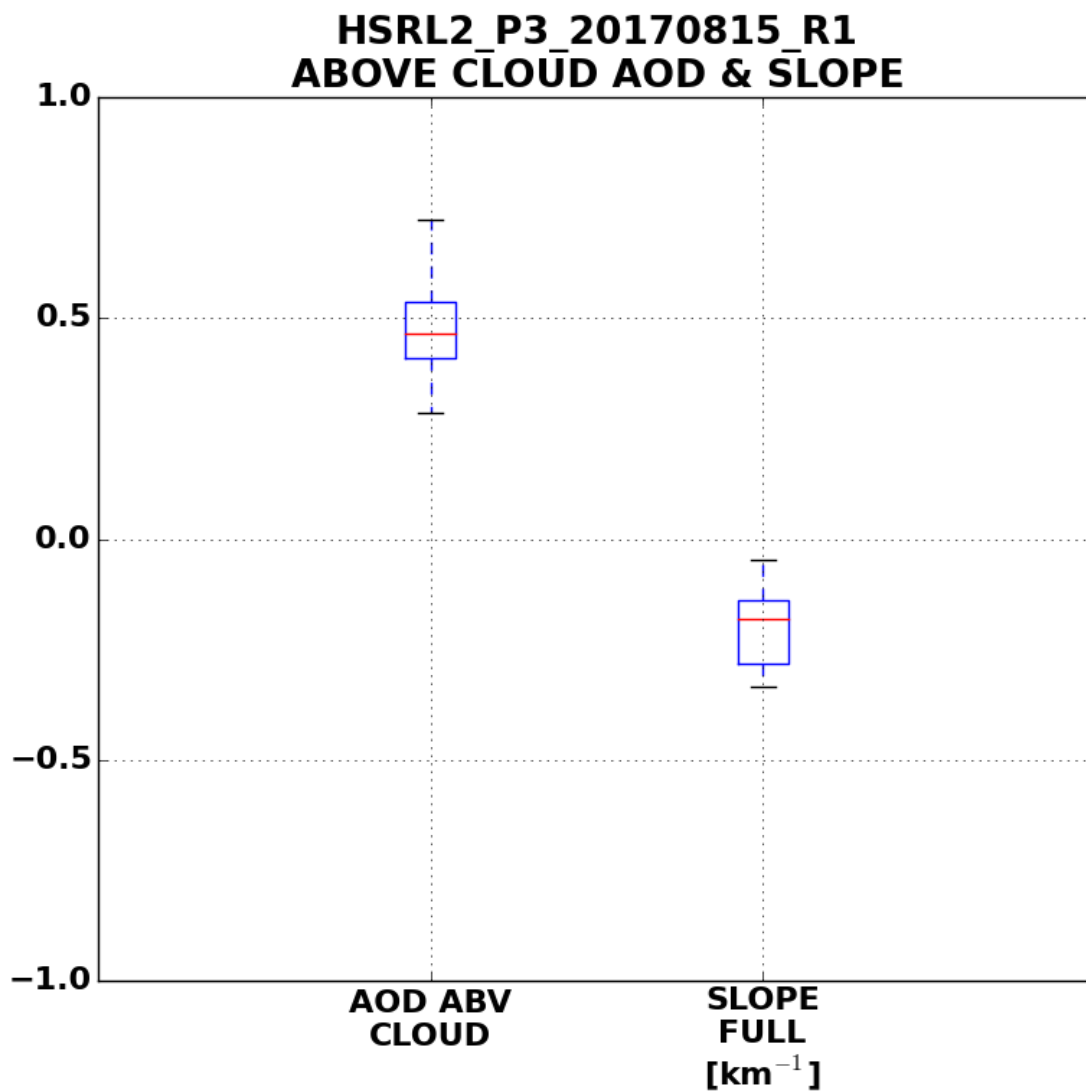


**Figure 4.9:** The average aerosol above-cloud optical depth (left) and the change in AOD across two range bins above cloud (~630 m, or two HSRL-2 range bins; right) for the 15 Aug. 2017 research flight. A negative slope corresponds to *increasing* AOD from the HSRL-2 toward the cloud.

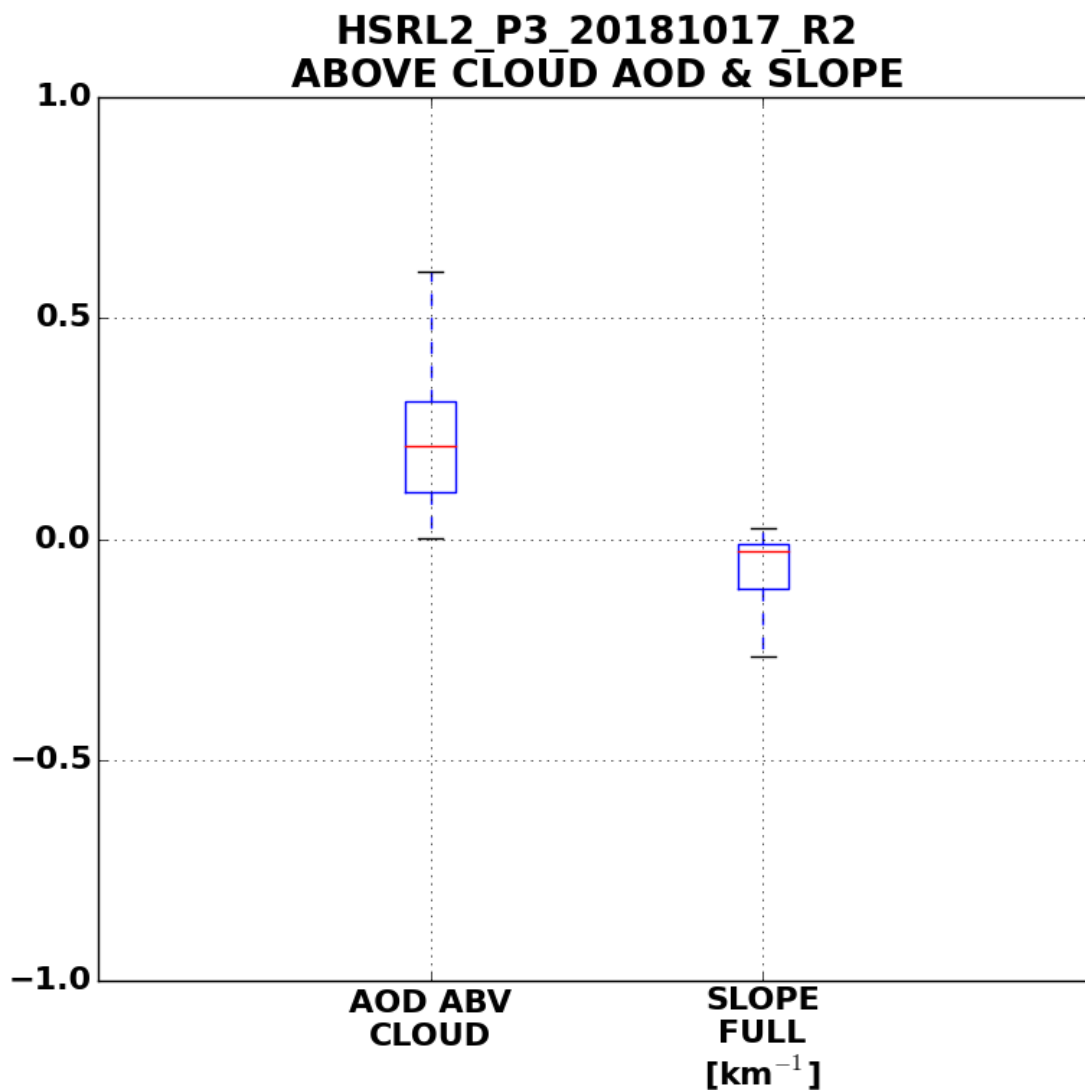


**Figure 4.10:** As in Fig. 4.9 but for the 17 Oct. 2018 research flight.

Simplifying results using a gap distance metric, in this context, can disseminate the effects of aerosols on precipitation frequency and cloud lifetime assuming other processes (i.e. meteorological and environmental controls) have been accounted for. Figures 4.9 and 4.10 demonstrate that aerosols contact the majority of cloudy profiles. Sampling contact vs. non-contact profiles, on top of

parsing data by EIS, requires careful statistical consideration especially since (as suggested by Fig. 4.7 and Fig. 4.8) aerosol contact with the StCu *and* low EIS conditions prevail most often.

Numerous studies connected variability in StCu total LWP with the diurnal cycle [Pincus et al., 1997; Wood 2012]. One convenient advantage of the ORACLES dataset to at least somewhat mitigate uncertainty due to diurnal effects is the fact that outbound, high altitude transit flights took place at approximately the same time every flight (~08 to 13 UTC). The implication here is that the first hour or two of each flight in 2017 and 2018 occur in lower EIS regimes and subject to less heating, whereas measurements taken near the end of the outbound high-altitude transits likely occur during peak diurnal heating. To mitigate the uncertainty in results due to the diurnal cycle, only data collected on these outbound transit flights are used.

#### *4.5.2: Assessment of aerosol effects on cloud and precipitation properties*

General statistics of CWP/RWP fraction are summarized in Fig. 4.11. The CWP/RWP statistic is chosen here because it encapsulates both CWP and RWP and indicates when a cloud is CWP or RWP dominated. For ORACLES, most CWP/RWP ratios were between 30:1 and 90:1, indicating (perhaps unsurprisingly) that most clouds contained little if any precipitable water. When partitioning by maximum column precipitation rates for light rain, typical CWP/RWP ratios fall to 1:2. Conversely, for very light drizzle at 0.01 mm/hr or less, ratios exceeding 100:1 are not uncommon. The sensitivity of the CWP/RWP ratio to RWP is especially striking,

and perhaps offers more insight into potential cloud-aerosol-precipitation interactions than radar data alone (i.e. RWP and RR only) can provide.

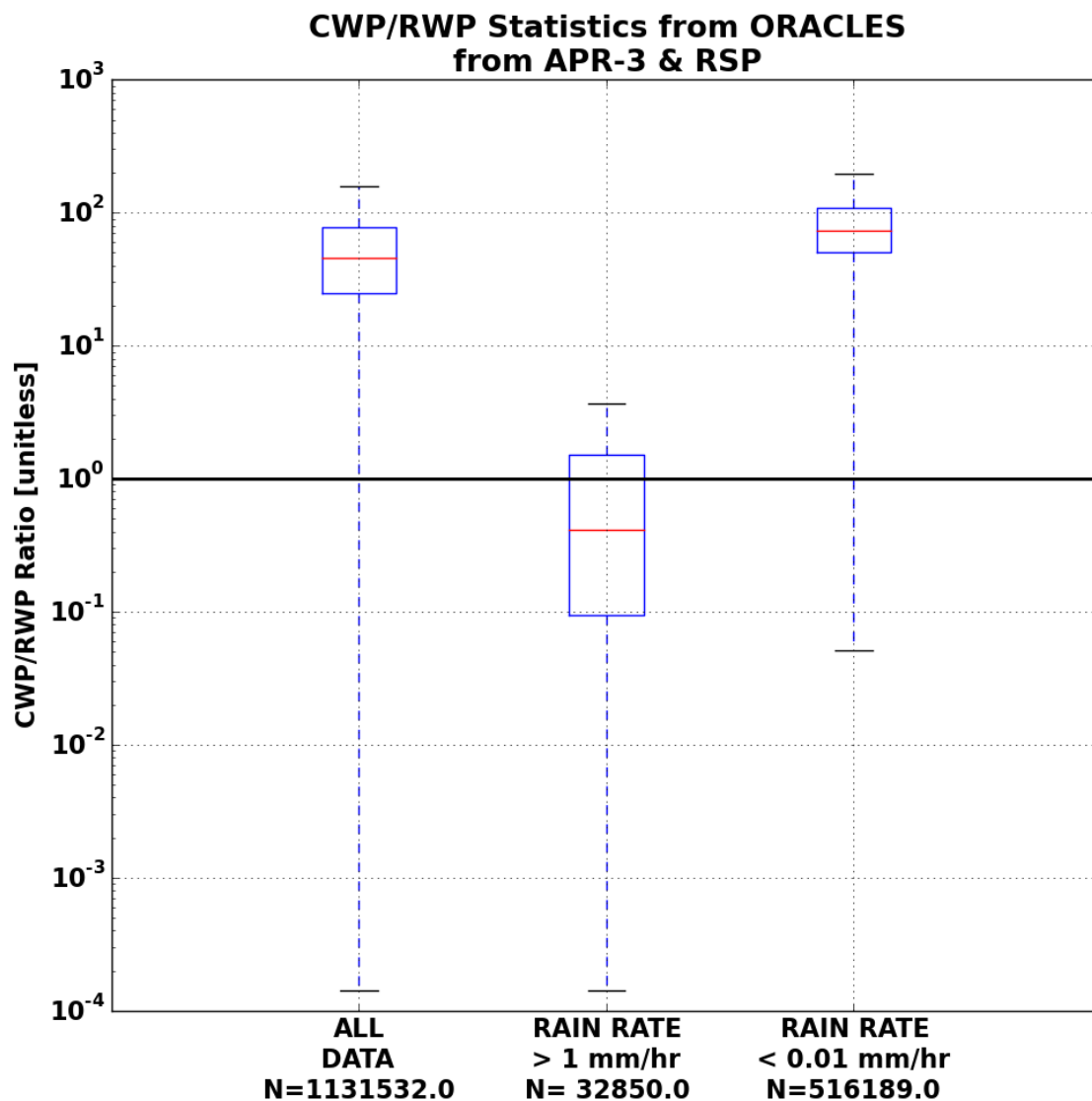


**Figure 4.11:** Box-and-whisker plots of CWP to RWP ratio for the ORACLES field campaign. The middle and right box-and-whisker plots correspond to light rain and light drizzle respectively.

Chapter 3 concluded that environmental controls must be considered prior to an aerosol indirect effect analysis. Figure 4.12 shows RWP, CWP and maximum column precipitation rate as a function of SST and EIS. Given the wide spread of data across a number of conditions, all correlations relating each cloud/precipitation variable to SST or EIS are weak. These variables are, however, slightly more correlated with EIS than SST. Despite these low correlations, the trends in data undeniably show some dependence on EIS and, to a lesser extent, SST. One particular trend that stands out is that larger CWP, RWP and RR occur with warmer SST but smaller CWP, RWP and RR occur with increasing stability.

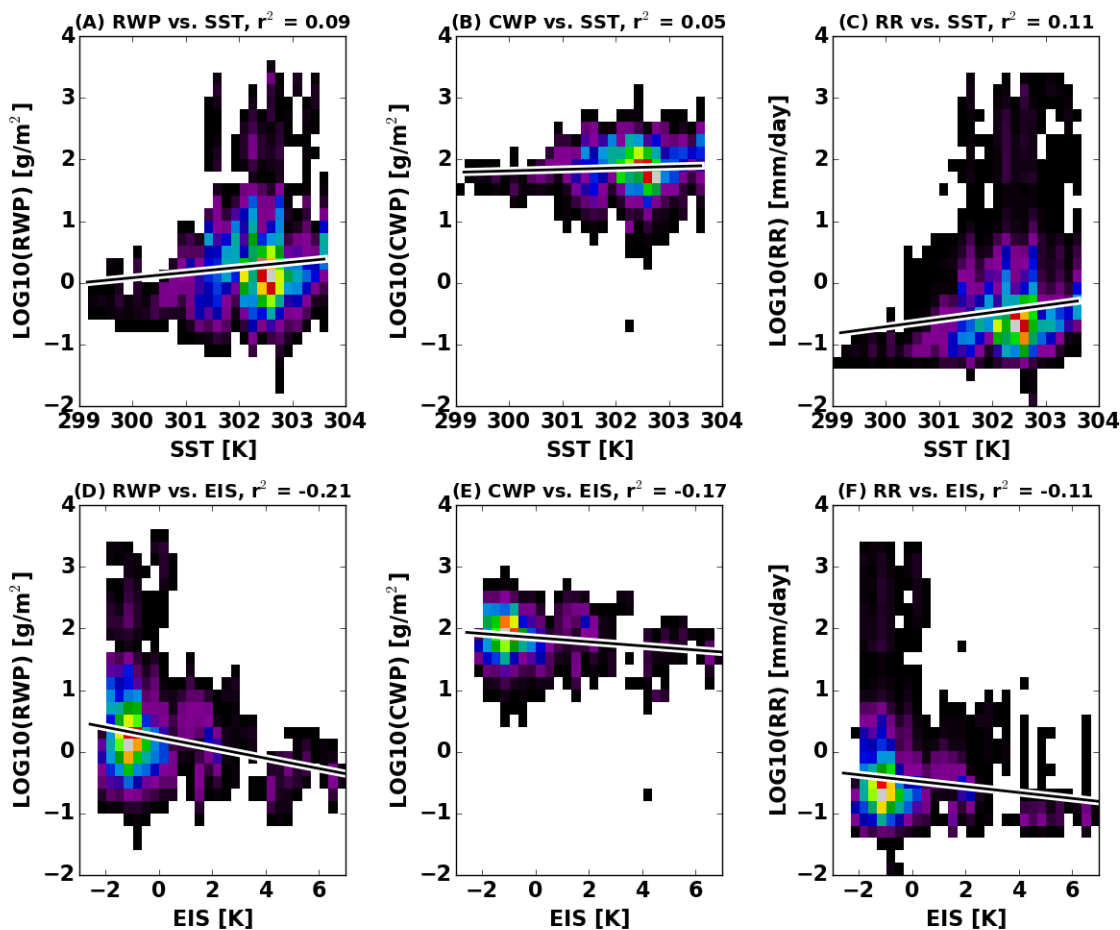


**Figure 4.12:** Retrieved RWP, CWP and maximum column precipitation rate (left to right) as functions of SST (top) and EIS (bottom). The dark lines represent 1<sup>st</sup> order lines of best fit. Pearson correlation coefficients are given in the title of each subplot. Colored pixels represent data where at least 30 points are binned. Each subplot is normalized to the number of points in the entire plot, with the red/gray pixels corresponding to values near 1.

When further partitioning data by the predefined aerosol contact versus non-contact scenarios, evidence of precipitation susceptibility arises from the CWP and RWP data (Table 4.1). When controlling for moderate ( $> 2$  K) and strong ( $> 4$ ) EIS scenarios, the ratio of CWP/RWP becomes much larger, indicating that increased stability leads to a higher likelihood of lower RWP. The estimated median

precipitation rate also decreases in the stable scenario (compared to the non-contact case), however, no results involving precipitation rate are statistically significant (p values > 0.1, or not significant at the 90% level).

**Table 4.1:** Summary of median CWP, RWP and maximum column precipitation rate for contact and non-contact scenarios, partitioned by stable (EIS > 2 K, or EIS > 4 K in parenthesis) or unstable (EIS < 0 K) environmental conditions.

	<b>CWP/RWP contact</b>	<b>CWP/RWP non-contact</b>	<b>P-value (CWP/RWP)</b>	<b>RR contact</b>	<b>RR non-cont.</b>	<b>P-value (RR)</b>
<b>Stable EIS &gt; 2K</b>	77.6	36.6	<< 0.01	0.212 mm/day	0.289 mm/day	0.137
<b>Stable EIS &gt; 4K</b>	91.4	32.0	<< 0.01	0.116 mm/day	0.252 mm/day	0.298
<b>Unstable</b>	47.8	48.7	<< 0.01	0.291 mm/day	0.180 mm/day	0.172

A very interesting result lies in the unstable data. For CWP, RWP and precipitation rate, all three median estimates increase when in contact with the aerosol layer. The statistically different CWP/RWP ratio, despite being similar within 1 unit between the contact and non-contact cases, is likely due to the fact that both CWP and RWP increase. Precipitation rate, similarly, increases when in contact with the aerosol layer. This result falls in line with Small et al. (2009) and Douglas and L'Ecuyer (*in prep*), which found that decreased cloud lifetime could occur in unstable environments. This phenomenon is likely explained by aerosol-induced invigoration, where increased aerosol loading allows for both cloud-size and rain-size droplets to grow to larger sizes before precipitating. Aerosol-induced

invigoration would also explain why the retrieved precipitation rates are generally larger in unstable environments. Evidence for aerosol invigoration exists in several observational studies [e.g. Koren et al., 2014; Mace and Abernathy, 2016] as well as modeling studies [e.g. Small et al., 2009; Oreopoulos et al., 2020 and reference therein]. Finally, given that most clouds measured in 0 K or less EIS regimes are likely transitioning StCu to Cu, or outright Cu, this result adds evidence to the idea that aerosols could invigorate precipitation albeit at the expense of cloud lifetime.

To this end, EIS has been used as a proxy for cloud type where unstable regimes assume cumulus-dominant and stable regimes assume stratus or StCu-dominant environments. A more thorough investigation would examine both EIS *and* cloud type, including how often open-cell or closed-cell clouds prevail, prior to repeating the analysis presented in this section. Cumulus in deeper MBLs is especially susceptible to aerosol invigoration, hence why a cloud-type specific analysis could further elucidate aerosol-cloud interactions.

The presented results offer evidence backing up previous studies that find precipitation suppression in stable environments and in contact with an overlying aerosol. Controlling for LWP [Albrecht 1989] could add further evidence to the results presented here, where CWP/RWP ratios may also indicate evidence for increased cloud lifetime. Reflectance data from the RSP could supplement this analysis by investigating possible increases in cloud albedo (corresponding to decreases in mean effective radius. Retrieved number concentrations from the RSP could also supplement this analysis by making a direct precipitation susceptibility measurement possible [Sorooshian et al., 2009] via the change in retrieved 2C-RAIN

precipitation rates as a function of the change in retrieved droplet number concentration. All of these suggested routes for future study, however, do neglect an important process: cloud processing of aerosols. The observed cloud-aerosol gaps could either be a physical separation of the StCu cloud and aerosol layers or evidence of aerosol processing via entrainment. The latter process is extremely difficult to observe, although it remains highly likely that both the entrainment of aerosols and physical separation occur.

#### **4.6: Conclusions**

In this chapter, a CWP retrieval product was added to the existing 2C-RAIN algorithm. Uncertainties in CWP lie in the 25-30% range. CWP, RWP and maximum column precipitation rate each increase with increasing SST but decrease with increasing EIS, although a large range of values are possible especially at warm SSTs and in highly stable environments. Statistically different CWP/RWP ratios between aerosol contact and non-contact regimes in stable environments hint at potential aerosol-based precipitation suppression. Ongoing analyses from the ORACLES cloud probe groups find a similar result under stable environments [Siddhant Gupta, personal communication]. Further tests are needed, including controls for total LWP, as well as supplementary reflectance, number concentration and effective radius data, to investigate the cloud albedo and lifetime effects. Each of these analyses will lend additional credence to the primary result indicating a marked increase in CWP relative to RWP with increasing stability and aerosol contact. Evidence for aerosol invigoration was found when evaluating data in the unstable

regime, which also represents another interesting avenue of research beyond the primary scope of this chapter.

## **Chapter 5: The role of evaporation in SE Atlantic stratocumulus clouds on Earth's energy budget**

To re-emphasize, one of the main science questions seeks to answer how much (or little) evaporating virga or drizzle in SE Atlantic StCu contributes to Earth's energy budget. Using the updated 2C-RAIN dataset outlined in Chapter 4, and taking advantage of both the vast quantity of radar measurements and the geographical expanse of measurements from ORACLES, this chapter outlines a process for quantifying evaporation rates from both virga and precipitation and generates an estimate of total latent cooling from SE Atlantic StCu.

### **5.1: Introduction**

Stratocumulus clouds are widespread over the Earth's subtropical oceans, and are a critical component of Earth's global energy balance [Lamb and Verlinde, 2011; Wood 2012]. These clouds can form under a wide variety of conditions globally, but over the subtropical oceans, StCu clouds are typically formed under regions of large-scale subsidence and lower tropospheric stability [Wood and Bretherton, 2006]. Precipitation processes in StCu clouds are especially important for governing their lifetime [Albrecht 1989]. Precipitation leads to the redistribution of cloud condensation nuclei through the planetary boundary layer and scavenging of aerosol particles [Radke et al., 1980; Hou et al., 2018], where both of the aforementioned processes modify local cloud properties. Understanding precipitation processes also requires a priori knowledge of environmental controls

including, but not limited to, boundary layer decoupling and entrainment [Wood 2012; Zhang et al., 2016; Douglas and L'Ecuyer, 2019].

Precipitation is also one of the largest sources of uncertainty in the global energy balance. In global energy budget frameworks, precipitation balances surface evaporation [Stephens et al., 2012]. The largest sources of both precipitation and evaporation come from the oceans [Baumgartner and Reichel, 1975]. Stephens et al. (2012) adjusted a previous estimate of latent heat flux to  $80 \pm 10 \text{ W m}^2$  due to CloudSat CPR-based measurements indicating increased global precipitation fraction (relative to what was previously known). Some of the uncertainty in this estimate is inherently due to the uncertainty in the vertical distribution of latent heating. While the distribution of latent heating (or cooling) does not affect the global balance between surface evaporation and precipitation, the amount and distribution of latent heating or cooling could strongly impact (for example) marine boundary layer mixing, cloud fraction and precipitation processes [Feingold et al., 1996a].

Observational studies of sub-cloud evaporation in our atmosphere remain severely limited, and existing studies of evaporation required numerous assumptions to make them possible. Lolli et al. (2017) found that evaporation rates retrieved from lidar and radiosonde measurements compared well with the analytical solution proposed by Li and Srivastava (2001), however, only two cases were presented in this study and horizontal drift by radiosondes introduce ambiguity in air mass sampling. Spaceborne radiometer-based studies of virga provide large-scale spatial context of virga and precipitation; however, these studies

are limited by the radiometer's classification of virga as surface precipitation [Wang et al., 2018]. Yang et al. (2018) recently showed that, for StCu data collected in the North Atlantic Ocean, 83% of StCu observed in their study were drizzling but only 31% of those drizzling cells actually reached the surface. When drizzle does not reach the surface, the sub-cloud layer immediately below cloud base cools, resulting in destabilization and increased mixing of the underlying planetary boundary layer [Feingold et al., 1996a]. This scenario for virga is especially true, given that drizzle-size drops usually evaporate within a couple hundred meters below cloud base [Fox and Illingworth, 1997]. Understanding processes that lead to virga and drizzle formation in StCu have wide-reaching implications on cloud feedbacks, cloud-aerosol-precipitation interactions, and the local environment [Nelson and L'Ecuyer, 2018].

This study aims to build upon recent observational studies such as Yang et al. (2018) by quantifying properties of virga and precipitation during the ObseRvations Above CLouds and their intERactions (ORACLES) field campaign from 2016-2018 [Redemann et al., *in prep*]. To our knowledge, virga characteristics and evaporation rates from virga have never been quantified over the SE Atlantic basin, thus representing one of the first extensive observational studies of virga for this region. Furthermore, precipitation properties derived from airborne radar during ORACLES [Dzambo et al., 2019] offers a unique chance to quantify and compare the latent cooling amounts from evaporating precipitation and virga. Though not covered in this study, the presence of a biomass burning (BB) layer over the SE Atlantic StCu deck offers a unique dataset for evaluating the effects of aerosols on cloud and

precipitation processes, which remain poorly understood processes [Stevens and Feingold, 2009]. Due to the lack of observational-based estimates of evaporation from virga and precipitation in the current literature, this study emphasizes the quantification of evaporation rates and fluxes with a focus on environmental controls. The next section describes the datasets used for this study.

## **5.2: Datasets**

For this study, we use the 2C-RAIN product generated from ORACLES Airborne Precipitation Radar - 3rd Generation (APR-3) radar data for the 2016, 2017 and 2018 campaigns [Dzambo et al., 2019]. Approximately 1.3 million profiles from the 2016 (~52,000), 2017 (~590,000) and 2018 (~650,000) campaigns are analyzed following the criteria described in this section. A brief description of both the APR-3 and 2C-RAIN datasets are also provided here. All data used in this study can be accessed via the NASA ESPO data archive for ORACLES [<https://espoarchive.nasa.gov/archive/browse/oracles>].

### **5.2.1: APR-3 Radar Data**

The APR-3 is a triple-frequency (Ku-, Ka-, and W-band) airborne radar utilized during all three ORACLES field campaigns, which took place at various times during the southern African continent's biomass burning (BB) season. The role of the APR-3 was to profile clouds and characterize precipitation over the southeast Atlantic Ocean, specifically in regions where the BB layer interacted with the Southeast Atlantic StCu deck. Most StCu observed during ORACLES were very thin,

and when they were precipitating, most precipitation rates were very light [Dzambo et al., 2019]. For these reasons, we use only the W-band (95 GHz) channel for this study. Attenuation effects are also accounted for and described in the next subsection.

### 5.2.2: 2C-RAIN Product

The 2C-RAIN product is an adapted version of the 2C-RAIN-PROFILE product [Mitrescu et al., 2010; Lebsock and L'Ecuyer, 2011; Dzambo et al., 2019], which was designed and implemented for use with CloudSat W-band radar data. W-band reflectivity profiles are first corrected for gas attenuation following Matrosov et al. (2004). Next, an adapted version of the CloudSat 2C-PRECIP-COLUMN [Haynes et al., 2009] algorithm is applied to the gas attenuation-corrected reflectivity data to attain initial estimates of surface rainfall rate, rain rate uncertainty, and hydrometeor attenuation (by comparing the observed surface backscatter or  $\sigma_0$  to a reference clear-sky  $\sigma_0$ ).

The 2C-RAIN algorithm is then employed to attain profiles of rainfall rate. This algorithm is a 1-D optimal estimation technique, which aims to minimize the following cost function (similar to Eq. 3.1 and Eq. 4.3):

$$\Phi = [Z_{sim} - Z]^T S_Z [Z_{sim} - Z] + [x - x_a]^T S_a [x - x_a] + \frac{(\tau_{sim} - \tau)^2}{\sigma_\tau^2} + \frac{(PIA_{sim} - PIA)^2}{\sigma_{PIA}^2} \quad (5.1)$$

Where  $Z_{sim}$  is the simulated reflectivity,  $Z$  is the APR-3 observed reflectivity,  $x_a$  is an a priori estimate of the background state,  $\tau_{sim}$  is the simulated optical depth,  $PIA_{sim}$  is the simulated path integrated attenuation,  $\sigma_\tau^2$  is the uncertainty in the optical depth estimate,  $\sigma_{PIA}^2$  is the uncertainty in the PIA estimate, and  $S_Z$  ( $S_a$ ) is the error covariance matrix for observational uncertainty (a priori estimate uncertainty). The European Centre for Medium-Range Weather Forecast (ECMWF) Re-Analysis Interim (ERA-Interim) data product [Dee et al., 2011] supplies atmospheric state variables. This algorithm further accounts for non-Rayleigh scattering effects and corrects for multiple scattering.

As in previous studies, the biggest limitation comes from the drop size distribution (DSD) assumption: it is impossible to quantify the exact spectrum of drop sizes for a given reflectivity measurement. The uncertainty from any liquid water content or rainfall rate retrieval, following any DSD assumption, is quite large. As described in Dzambo et al. (2019), rainfall rates are computed using the Abel and Boutle (2012) DSD assumption. Uncertainties in rainfall rate for certain drizzling scenes are typically on the order of 150-200%, with higher uncertainties for smaller rainfall rates. Regardless, the large uncertainties in the retrieved rainfall rates will not introduce bias in any results given the  $\sim 1.3$  million rainfall rate profiles utilized for this study although the uncertainty arising from the retrieved rainfall rate profiles necessitates a large uncertainty estimate to go with any estimated results.

Figure 5.1 highlights both the APR-3 and 2C-RAIN datasets. The top panel in Fig. 5.1 shows uncorrected W-band radar reflectivity, while the next two panels show the modeled hydrometeor attenuation correction and corrected W-band radar

reflectivity. For this particular case, virga is present in most of the radar profiles along with two distinct surface precipitating cells. Aside from the second precipitating cell, which contains a pocket of reflectivity values greater than 0 dBZ, the vast majority of maximum reflectivity values in each individual profile is between 0 and -20 dBZ. The maximum rainfall rate in each virga profile ranges between 0.01 and 0.03 mm/hr (or ~0.2 to 0.6 mm/day). As we will show later, the maximum rainfall rate in a majority of virga profiles is between those two values.

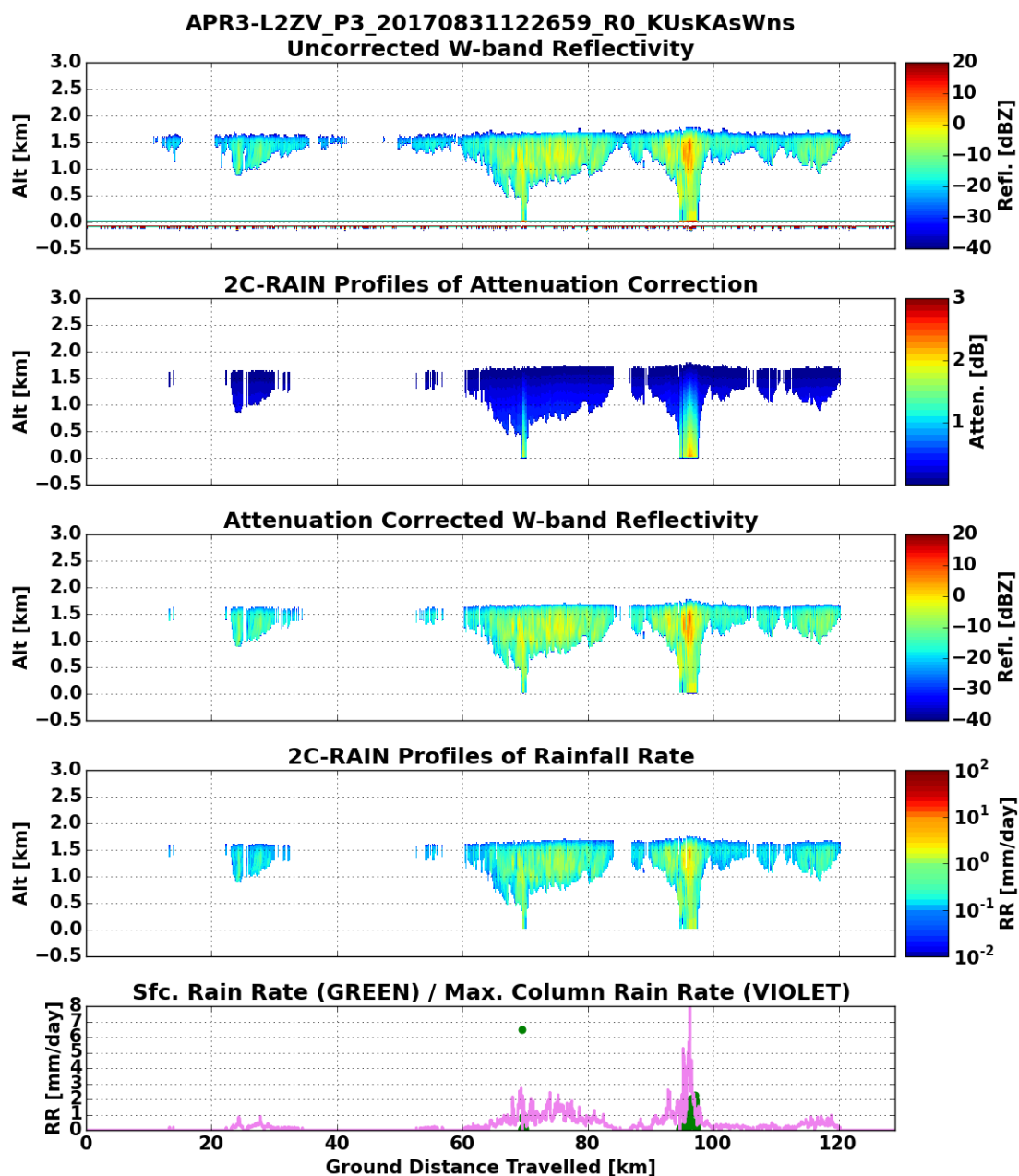


**Figure 5.1:** An APR-3/2C-RAIN example from the 31 Aug. 2017 research flight, with this particular radar scan beginning at 12:56 UTC and showing uncorrected W-band reflectivity (top), modeled hydrometeor attenuation (top-middle), corrected W-band reflectivity (middle), profiles of rainfall rate (bottom-middle) and rainfall rates representing surface (green) and profile maximum (violet) from nadir APR-3 and 2C-RAIN data. For this case, scanning W-band data were used, which had approximately 10 dB less sensitivity (e.g. minimum detectable signal was about -20 dB).

### 5.3: Methods

We evaluate evaporation rates from W-band radar profiles for both virga and surface-precipitating profiles, and the classification methodology for virga and surface precipitation are outlined here. Virga is first defined as any profile with a zero surface rain rate but also contains a maximum reflectivity of at least -15 dBZ, while surface precipitation follows the same logic but with a non-zero surface rain rate. The purpose of the -15 dBZ threshold is twofold: a -15 dBZ threshold follows the minimum criteria for "rain possible" scenes in CloudSat data [Haynes et al., 2009], and -15 is a "near-consensus" threshold value quantified from previous studies showing that drizzle-size drops are present when the maximum reflectivity in a profile is at least -20 to -15 dBZ [e.g. Mace and Sassen, 2000; Kollias et al., 2007; Liu et al., 2008. Wang and Geerts (2003) showed that larger reflectivity values near the cloud top do not always contain drizzle-size drops, but near the cloud base, reflectivity values exceeding the prescribed drizzle threshold are more certain to be actual drizzle drops. Requiring the maximum reflectivity to occur in the lowest half of the reflectivity profile, therefore, reduces uncertainty that the virga profile is indeed precipitating. Finally, a minimum distance of 400 meters is required between the bottom of the cloud or virga/precipitation profile and the surface. Given that the maximum reflectivity in a virga profile is often less than 0 dBZ, and noting that rain-size droplets typically fall at  $\sim 2$  m/s, rain would reach the surface in  $\sim 3$  minutes. Since clouds typically live for 30-45 minutes, the odds of misclassifying a profile as virga instead of surface precipitation are very low.

Unlike previous studies such as Lolli et al. (2017) or Morrison et al. (2009), where evaporation rates were quantified as a change in mean drop diameter or rain water mixing ratio over time, we directly estimate the evaporation rate (in mm/day) using the 2C-RAIN algorithm. We define evaporation rate in this study as being equal to the rainfall rate at cloud base, which is taken to be the maximum column rainfall rate in the profile. The idea to use the maximum rainfall rate (or sedimentation flux) as cloud base is supported by previous studies [e.g. Ragette and Wotawa, 1998], especially in cases such as ORACLES where the vast majority of precipitation is weak and mostly occurs far above ground level.

We use ERA-Interim atmospheric state data used to assess environmental controls including sea surface temperature (SST), relative humidity (RH), and estimated inversion strength (EIS, refer to Wood and Bretherton (2006) for more information). Partitioning results according to EIS, among other environmental control variables, offers the advantage of assuring (for example) aerosol effects on clouds are robustly quantified [Douglas and L'Ecuyer, 2019]. Aerosol effects are, however, not examined in this study. Trends in evaporation rate according to SST and EIS are presented in this study. Our evaluation of RH (not shown) was inconclusive and dubious at best, although we note that if in-situ RH were available and collocated with the 2C-RAIN product, confidence in those results would be much higher.

#### **5.4: Campaign Evaporation**

Figure 5.2 shows the cumulative distribution of evaporation rates derived from virga and surface precipitation as a function of EIS. This figure elucidates a number of ideas from the ORACLES 2C-RAIN dataset. First, virga occurring under low EIS (or unstable environments corresponding to  $EIS < 0$  K) was the most frequently occurring scenario and occurred nearly 10 times more often than the high EIS (i.e.  $EIS > 2$  K or stable environments) virga or the low EIS surface precipitation scenario. Surface precipitation rarely occurred in high EIS regimes, with 100 times fewer data than data from the low EIS surface precipitation regime. High EIS regimes occurred frequently during the 2016 campaign, however, only five flights contained collocated APR-3 and RSP data thus representing a very limited subset (~52,000 out of 1.3 million total usable profiles). Given that only around 1% of all cloudy profiles had any measurable surface precipitation rate in high EIS regimes, it should be no surprise that the total number of surface precipitation profiles in high EIS regimes is several orders of magnitude less than in the other scenarios. Regardless, surface precipitation in both the low and high EIS regimes have a significant fraction of points in the 1 mm/day to 10 mm/day range. By contrast, nearly all evaporation rates from virga are less than 1 mm/day.

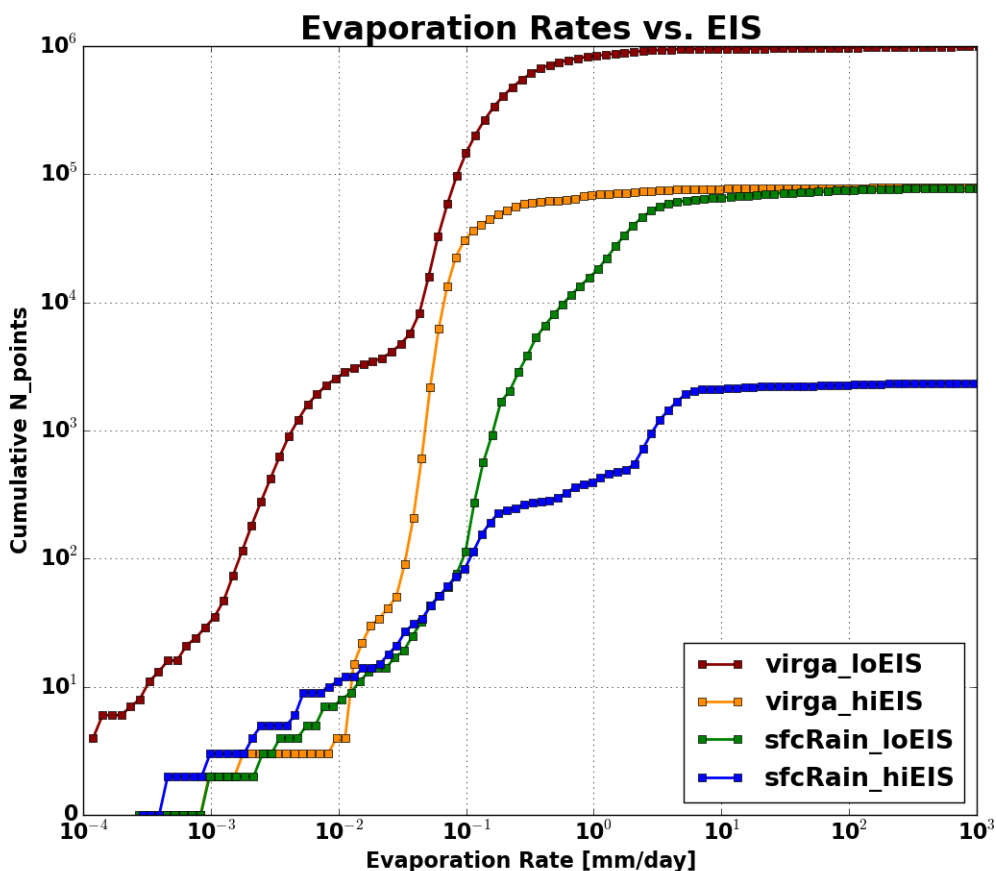


**Figure 5.2:** Cumulative distributions of evaporation rates derived from virga and surface precipitation. Results are partitioned by low EIS (i.e.  $EIS < 0$  K) and high EIS (i.e.  $EIS > 2$  K).

Table 5.1 shows the median evaporation rates and derived evaporation fluxes from the scenarios explored in Fig. 5.2. Following Fig. 5.2, surface precipitation contributes much more evaporation in both stable and unstable regimes compared to virga. The evaporation rates and fluxes for high EIS virga regimes are less than those under low EIS virga regimes. Interestingly, the median evaporation rate from surface precipitation in high EIS regimes is nearly 1.5

mm/day larger. Following a similar statistical significance testing methodology from Chapter 4, no statistical significance is found when comparing evaporation in different EIS regimes for either virga or surface precipitation. Statistical significance arises when comparing evaporation from surface precipitation to virga.

**Table 5.1:** Summary of median campaign evaporation statistics from surface precipitation and virga, partitioned by unstable (EIS < 0 K) and stable (EIS > 2 K) regimes. Positive evaporation fluxes imply a latent cooling.

	Evaporation Rate [mm day <sup>-1</sup> ]	Evaporation Flux [W m <sup>-2</sup> ]
Surface Precipitation EIS < 0 K	2.32	65.4
Surface Precipitation EIS > 2 K	3.74	105.4
Virga EIS < 0 K	0.253	7.12
Virga EIS > 2 K	0.138	3.88
Campaign Virga	0.255	7.16
Campaign Surface Precipitation	2.47	69.6

Following the key results in Dzambo et al. (2019), especially for the 2016 and 2017 campaigns, lower evaporation rates in 2016 (not shown) qualitatively align with lower retrieved surface precipitation rates throughout the 2016 campaign. The structure of attenuation-corrected W-band reflectivity (Fig. 8 in Dzambo et al., 2019) indicated that clouds were generally shallower and had lower reflectivity throughout the column. The 2017 and 2018 campaigns, by comparison, had very similar cloud and precipitation structure (not shown).

The experiment location in 2016 (Namibia) resulted in the majority of measurements being collected closer to the African coast and on the southern

portion of the StCu deck, whereas the experiment location in 2017 and 2018 (São Tomé) allowed for more observations from the heart of the StCu deck. Figure 5.3 shows median evaporation rates from virga for all three campaigns as well as median evaporation rates from the entire campaign across the Southeast Atlantic basin. Following Figure 5.2, the median evaporation rate observed across the ORACLES experiment domain was generally between 0.3 to 0.6 mm/day. Evaporation rates increased west of the African coast. For 2016, evaporation rates of 0.3 mm/day or less were very common, especially near the coast. Slightly higher evaporation rates are noted further west along the routine flight track for that year (ending at approximately 10°S and 0°E).

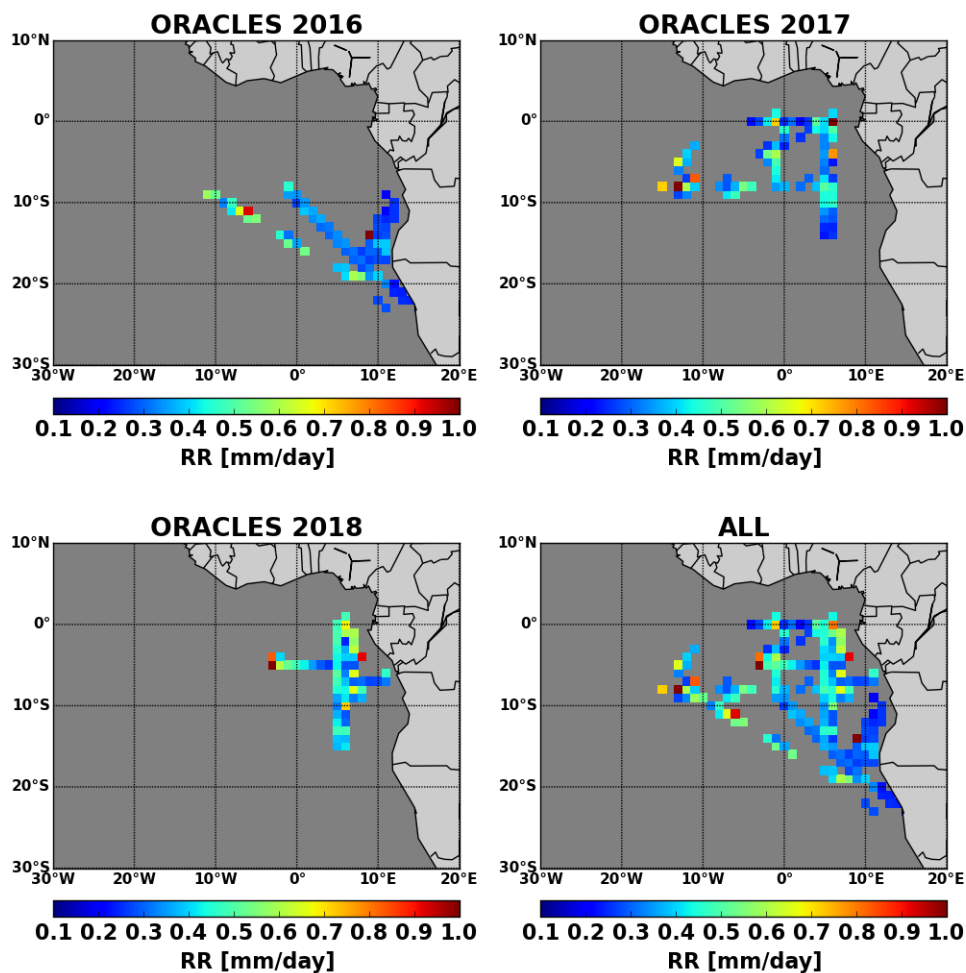


**Figure 5.3:** Median evaporation rate as a function latitude and longitude (in 1 degree bins) for the 2016 (top-left), 2017 (top-right), 2018 (bottom-left) and entire (bottom-right) ORACLES campaign.

The character of evaporation in 2017 and 2018, compared to 2016, is quite different. In 2017, the median evaporation rate along the routine flight track falls between 0.5 and 0.6 mm/day around 10°S, but decreases in both the northward and southward directions (e.g. around 5-7°S and 12-15°S latitude). The meteorological drivers and potential effects of aerosols will be the topic of future studies. With this

in mind, we note that the African easterly jet is typically centered near 10°S this time of year [Adebiyi and Zuidema, 2016], and dynamical drivers associated with the easterly jet could explain this peak in evaporation rate centered at 10°S. West of the 5°E routine flight track, evaporation rates again are larger especially in 2018 where the median evaporation rate exceeds 0.6 mm/day (around 4-5°W). The sampling of StCu in the stratocumulus to cumulus transition region [Yamaguchi et al., 2015] could explain why larger evaporation rates are observed around this point. Furthermore, higher median evaporation rates are observed in many locations compared to 2017, which follows the increased number of higher evaporation rates (above 0.5 mm/day) indicated in Fig. 5.3. With over ~1.2 million profiles analyzed from 2017 and 2018, and with most of them collected along the 5°E longitude path, many opportunities for studying aerosol effects on evaporation rate are possible.

Across all campaigns, we find that evaporation rate appears to vary with both SST and EIS (Fig. 5.4). The vast majority of evaporation rates are 0.4 mm/day or less for SSTs less than 301 K. Above 301 K, and where EIS is less than 2 K, evaporation rates are found to be higher at 0.4 to 0.6 mm/day. This result corroborates Fig. 4.12, which showed that larger maximum column rain rates (analogous to the evaporation rates assumed in this study) occurred more often in higher SST and lower EIS regimes. StCu observed in these regions were generally thicker and contained a larger maximum column reflectivity. With few exceptions, regions with low EIS (i.e. less than about 2 K) occurred closer to the equator. Interestingly, regions containing the highest evaporation rates occurred when SSTs were high

(greater than 302 K) as well as EIS (greater than 3 K). Evaporation rates contained in the aforementioned regions will be of great interest in future studies, given these clouds are likely maintained by larger moisture fluxes and further sustained by strong inversions aloft.

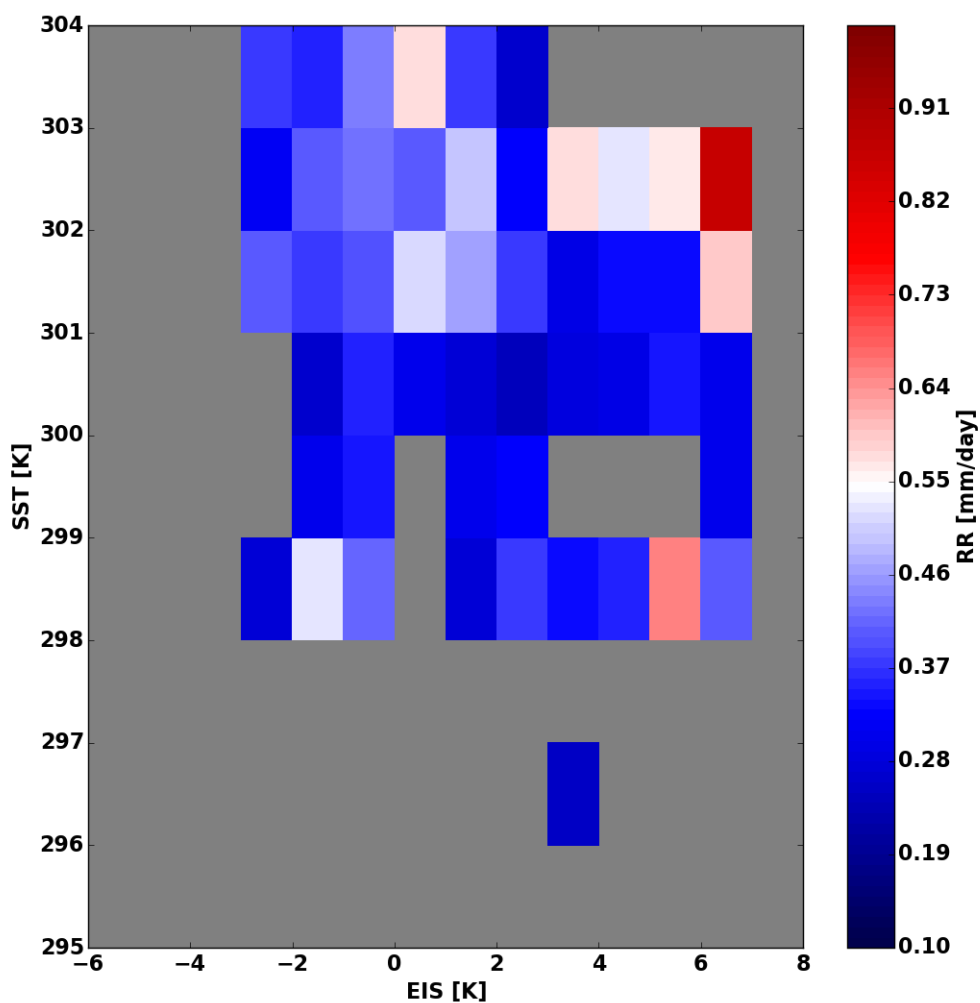


**Figure 5.4:** Median evaporation rate as a function of estimated inversion strength (EIS; x-axis) and sea surface temperature (SST; y-axis). EIS and SST bins are each binned every 1 K.

The campaign median conditional evaporation rate for virga is an estimated 0.25 mm/day, with the vast majority of evaporation rates between 0.2 mm/day and 0.6 mm/day. The campaign median conditional evaporation rate from surface precipitation, by comparison, was approximately 2.5 mm/day. These estimates align very well with estimates of cloud base rainfall rate from the Comstock et al. (2004) evaporation-sedimentation model, where estimates of  $\sim 0.25$  to 2 mm/day were attained for reflectivities in the range used for our study. From this point, virga- and surface precipitation-based evaporation flux (Eq. 5.1) and heating (cooling) rate (Eq. 5.2) can be estimated (evaporation flux values are recorded in Table 5.1):

$$F_z = \rho_l L_v E_z \quad (5.1)$$

$$H = \frac{-1}{\rho_a c_p} \int_{z_{sfc}}^{z_{cb}} \frac{dF}{dz} = \frac{-1}{\rho_a c_p} \frac{F_{cb} - F_{sfc}}{z_{cb} - z_{sfc}} \quad (5.2)$$

Equations 5.1 and 5.2 imply that, whether carrying out a computation for virga or surface precipitation, the only difference in the estimated values would come from the height dependence in Eq. 5.2.

The campaign estimates of virga- and surface precipitation-based evaporation rate correspond to associated evaporation fluxes of  $7 \text{ W m}^{-2}$  and  $70 \text{ W m}^{-2}$  respectively, implying that evaporating light or heavy drizzle can significantly cool the sub-cloud layer. The implications for this magnitude of latent cooling become significant when one considers the typical extent of the StCu cloud layer during the biomass-burning season over the South African continent. Figure 5.5 approximates the area covered by StCu clouds over the SE Atlantic Ocean during this time. A qualitative analysis of the StCu cloud deck sizes suggests that the typical

expanse of this cloud deck ranges from  $3 \times 10^6 \text{ km}^2$  to  $7 \times 10^6 \text{ km}^2$ . The lower bound of possible SE Atlantic StCu areal coverage could theoretically be much lower than  $3 \times 10^6 \text{ km}^2$ , especially given the degree of (essential) subjectivity determining what clouds are part of the StCu cloud deck and what clouds formed via other processes.

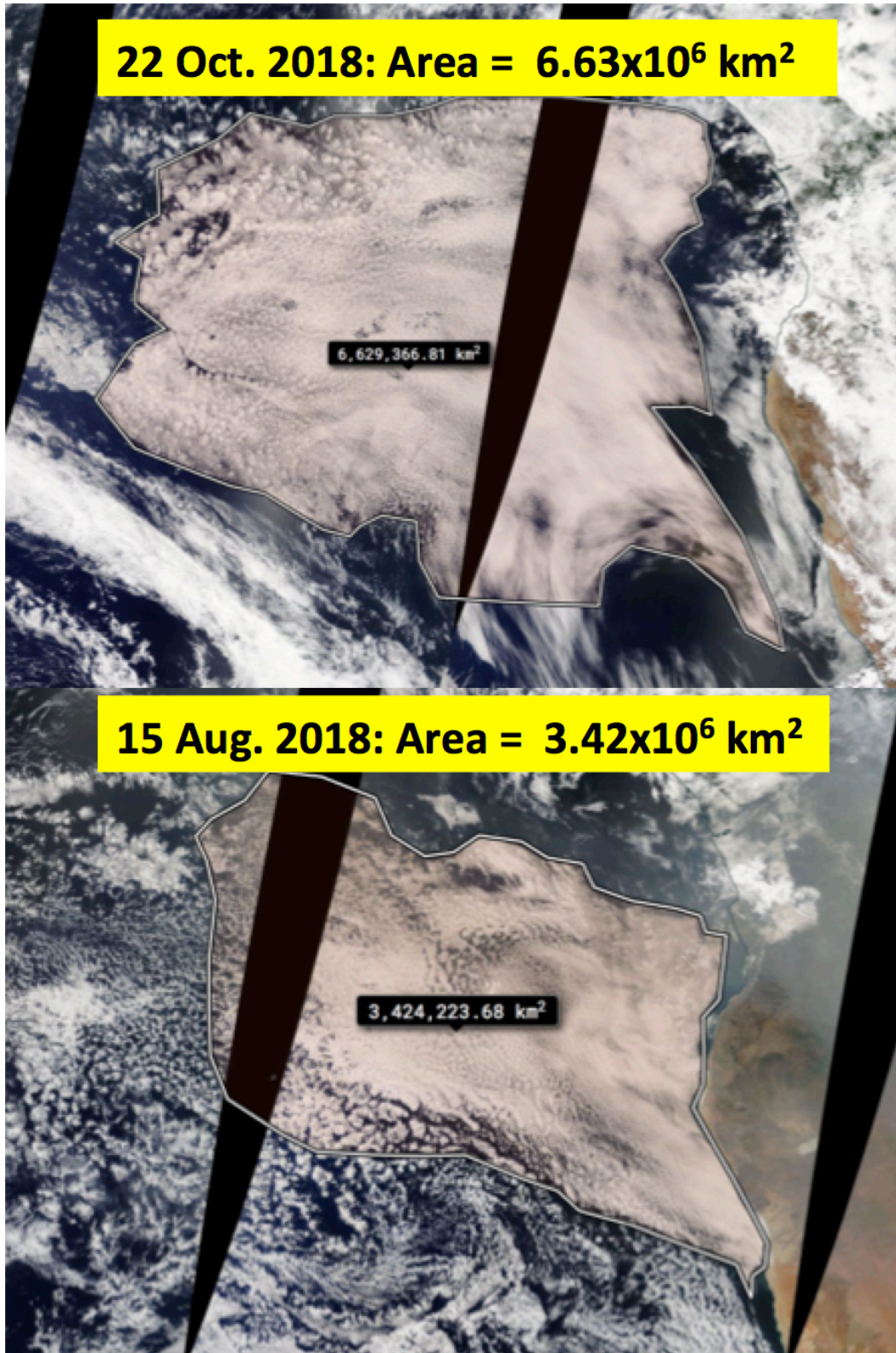


**Figure 5.5:** Estimated areal coverage of the SE Atlantic StCu cloud deck on 22 Oct. 2018 (top) and 15 Aug. 2018 (bottom). Both images and estimates were provided courtesy of <https://worldview.earthdata.nasa.gov>.

Knowing the cloud fraction, virga and surface precipitation fractions, and the median latent cooling for a given area, one could compute the total cooling power from the SE Atlantic StCu deck as:

$$C = \oint CF(A)PF_{v,p}(A)LH_{v,p}(A)dA \quad (5.3)$$

Where  $C$  is the total cooling power,  $CF$  is the area cloud fraction, and  $PF$  and  $LH$  are precipitation fraction and sub-cloud latent cooling (corresponding to virga and surface precipitation respectively) from evaporation as a function of area. Cloud fraction in the examples shown in Fig. 5.5 is nearly everywhere in the prescribed area, with lower cloud fractions around the edges of the StCu deck. Precipitation fraction is trickier to estimate for a number of reasons. Dzambo et al. (2019) found that surface precipitation occurred almost twice as often near the coast than away from the coast in 2016 compared to 2017. The surface precipitation amount is also somewhat dependent on EIS (Fig. 5.6). In unstable environments ( $EIS < 0$  K), the estimated surface precipitation fraction hovers near 8%. In somewhat stable or very stable environments, precipitation fraction drops off to under 2%. Virga fraction is estimated from Dzambo et al. (2019). When applying the median values for evaporative cooling (flux) or cooling rates into Eq. 5.3, surface precipitation is estimated to account for nearly twice as much evaporative cooling compared to virga (a ~2:1 ratio). The main implication from this computation is the fact that, while the evaporative cooling from surface precipitation dominates, virga cannot be

ignored in any meaningful energy budget analysis. Evaporative cooling from virga and surface precipitation plays a key role in local boundary layer dynamics and thermodynamics, with further implications for (among other processes) cloud lifetime.

A measure of net evaporative energy output can be estimated from Eq. 5.3. Using the median values for evaporative cooling for virga and surface precipitation, along with the estimates presented here, an estimated 0.03 PW of sub-cloud evaporative cooling occurs in the SE Atlantic StCu deck. Accounting for upper bound ( $A = 7 \times 10^6 \text{ km}^2$ ,  $CF = 1$ ,  $PF_p = 12\%$ ,  $PF_v = 55\%$ ) and lower bound ( $A = 3 \times 10^6 \text{ km}^2$ ,  $CF = 0.35$ ,  $PF_p = 2\%$ ,  $PF_v = 30\%$ ) cloud and precipitation fraction estimates, sub-cloud cooling from evaporation ranges from 0.003 PW to 0.08 PW. The purpose of this calculation is to provide reference for similar calculations made across other major subtropical StCu decks where extensive data are available. For this work, a more instructive calculation lies in the comparison of average/median evaporation flux or heating rate between virga and surface precipitation with average/median virga and surface precipitation fractions accounted for.

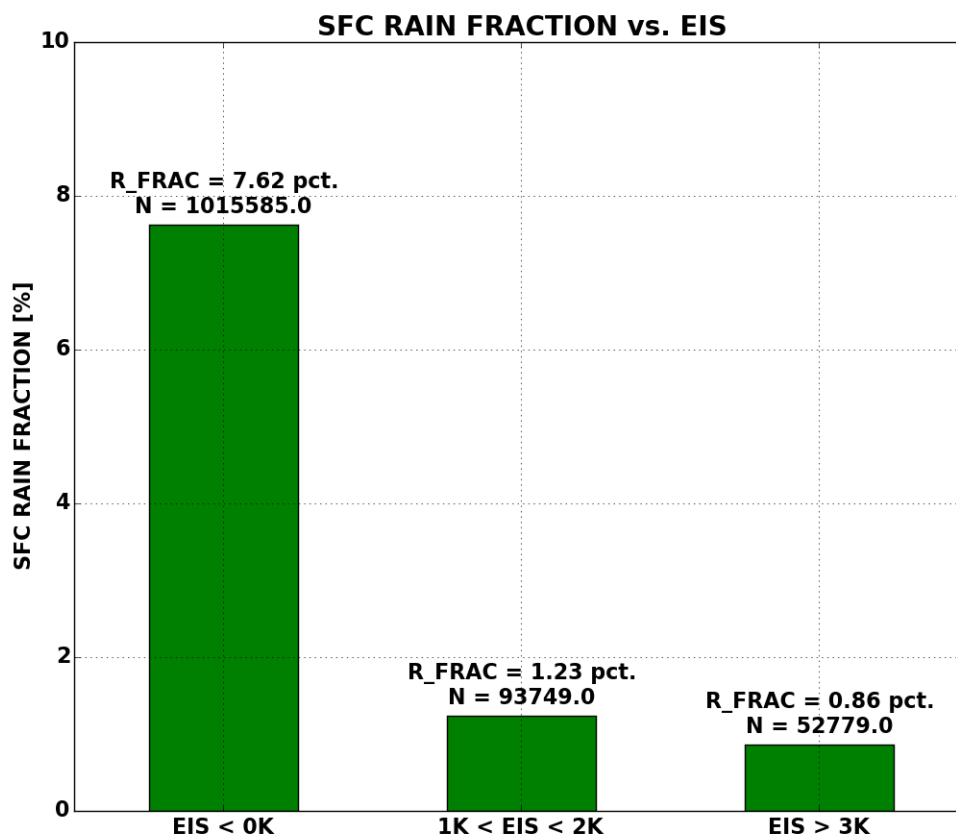


**Figure 5.6:** Estimated surface precipitation fraction as a function of EIS.

The utility of the estimated cooling power output from SE Atlantic Stratocumulus clouds remains an area of active research and investigation. To gain more utility out of this estimate, similar calculations must be carried out across all major StCu decks. With atmospheric remote sensing systems becoming more sophisticated and capable of observing phenomena in greater detail across the globe, power output computations could be very useful as a means of validating a number of model processes.

Validating latent heating/cooling across the StCu deck would have a number of useful applications. For example, finding the balance between precipitation and surface evaporation in the StCu region would elucidate sources and sinks of latent energy. This result could inform process-oriented physics, where the amount of latent heating/cooling in a model is predicated on the amount of (for example) autoconversion parameterizations and resulting precipitation. Validating latent heating/cooling estimates using observations represents a possible pathway toward diagnosing vertical heating/cooling rates, vertical motion, and perhaps (indirectly) validating precipitation processes. These processes become especially important to understand in the presence of aerosols, where both vertical motions induced by latent heating/cooling and precipitation processes scavenge and redistribute aerosol throughout the MBL. Ultimately, understanding the role of evaporative cooling in redistributing heat throughout the atmosphere has a variety of implications toward de-convolving thermodynamic, dynamical and radiative processes in the subtropical StCu decks.

## **5.5: Conclusions**

An extensive observational-based analysis of evaporation from virga and surface precipitation over a major oceanic basin is presented. We estimate evaporation rates and fluxes from nearly 1.3 million attenuation-corrected reflectivity profiles over all three ORACLES deployments. Evaporation rate estimates from virga are estimated to be 0.2 to 0.6 mm/day, while evaporation rates from surface precipitation are an order of magnitude larger. Slightly lower

evaporation rates are found for 2016, likely owing to the experiment location's proximity to the African coast and sampling regions where low SST and high EIS prevailed compared to 2017 and 2018. A higher count of larger evaporation rates are noted in 2018 compared to 2017, with less discernible variability in evaporation rates noted for 2018. Both SST and EIS an important control in evaporation rate as well.

Regardless of environmental controls, latent cooling from both surface precipitation and virga are significant. Surface precipitation occurred much less often than virga during ORACLES, yet the median latent cooling from surface precipitation is larger than that from virga by an approximated 2:1 ratio. This result highlights the importance of both surface precipitation and evaporating virga on sub-cloud latent cooling. When accounting for plausible cloud, virga and precipitation fractions across the StCu cloud deck, and using the calculated median evaporation (latent cooling) fluxes, sub-cloud cooling from the SE Atlantic StCu deck is on the order of  $\sim 0.02$  PW, with upper and lower bound values of 0.08 and 0.003 PW respectively. Evaporation from evaporating virga contributes approximately a third of this net cooling, illustrating that virga is just as important as surface precipitation toward cooling the MBL.

The large uncertainties in the evaporation rate estimates will require future studies on the topic of sub-cloud evaporation. While airborne radar provides accurate cloud, virga and surface precipitation rate estimates, the magnitude of precipitation (evaporation) rate uncertainties exceed 100% in nearly every scenario, which impacts the upper- and lower-bound cooling power estimates. An

adapted version of the Wisconsin Algorithm for Latent Heating and Rainfall Using Satellites [WALRUS, Nelson et al., 2016], a Bayesian retrieval algorithm also using W-band reflectivity and PIA, would provide independent estimates of latent heating profiles from the same data presented in this study, thus revealing possible biases in the quoted estimates in this study. Finally, all measurements presented in this study were collected during ORACLES, which corresponds to the climatological peak in StCu areal coverage.

Precipitation processes play a very important role in redistributing aerosols and other CCN throughout the planetary boundary layer. Virga, by definition, evaporates before reaching the surface, therefore redistributing aerosols and CCN throughout the PBL without bringing them to the surface. Latent cooling from sub-cloud evaporation also aids in the maintenance of StCu by driving additional vertical mixing. Evaporation rates from surface precipitation, by contrast, cool the entire layer between cloud base and the surface, further complicating the local structure of latent heating. Our estimates of evaporation rate could provide an important observational constraint for future modeling studies, especially those related to the scavenging, consumption and redistribution of aerosols throughout the PBL.

## Chapter 6: Future Research

Numerous avenues of further research are possible stemming from the results presented in Chapters 4 and 5.

In the Chapter 4 aerosol indirect effect study, the aerosol semi-direct effect was not explicitly accounted for in the touching vs. non-touching partitioning. One method of exploration lies in the refractory black carbon in-situ dataset collected during ORACLES. Black carbon is highly absorptive and was frequently observed in the BB aerosol layer, and noting from Chapter 4 that layers of thick smoke over 1 km thick could realistically have heating rates of  $\sim 0.5$  K/hr or larger, meaning the local thermodynamic environment could change quite dramatically. As one example, a strengthened above-cloud inversion (increased EIS) for highly absorbing above-cloud aerosol could possibly lessen the entrainment of aerosols into the StCu cloud deck since both vertical motion and entrainment rate are closely correlated [Kazil et al., 2017]. Aerosol-induced heating in the StCu cloud deck itself is not considered in this study, but is an active area of research by other ORACLES investigators and such results will provide important additional context for the efficacy of all aerosol indirect effect studies.

Multi-frequency radar-based precipitation retrieval development is another avenue for future research. While moderate and heavy precipitation occurred infrequently during ORACLES, a number of heavily precipitating trade cumulus scenes occurred (e.g. Fig. 4.1) where heavy attenuation resulted in very large uncertainties in the retrieved rain rates. ORACLES is also the first field campaign

where the APR-3 flew entirely over the ocean, although the recently completed CAMP2Ex experiment also likely offers abundant triple-frequency measurements of precipitation. Using two or more frequencies enables a direct retrieval of a DSD, which would offer the following advantages:

1. Eliminating the need for the rain rate lookup tables presently used in this algorithm,
2. Direct solution for two (or three) of the slope/shape/intercept parameters if two (or three) frequencies are used,
3. Elimination of the uncertainties caused by PIA and layer attenuation, and
4. Further reduction in rain rate uncertainties created by assuming a DSD, and replaced by uncertainties arising from using one assumed parameter (if two frequencies are used), which is expected to be less.

Expanding the algorithm to accommodate an extra vector of measurements would be straightforward:

$$Y = ([Z_1, dA_1], [Z_2, dA_2], \dots [Z_N, dA_N])$$

$$dA_x = Z_{Ka,x} - Z_{W,x}$$

Where  $Z$  is the  $W$ -band reflectivity profile and  $dA$  is the differential attenuation at layer  $x$  between a lower and higher frequency radar ( $Ka$ -band and  $W$ -band in this example). A dual-frequency precipitation retrieval algorithm likely has the most utility over a triple-frequency algorithm since, for most raining scenes, the  $Ku$ -band and  $Ka$ -band frequencies will observe the same profile to within each channel's measurement uncertainty. Likewise, few scenarios likely exist where all three frequencies would observe precipitation from cloud top to the surface. The

majority of the work stemming from the development of a multi-frequency precipitation retrieval algorithm lies in using the observed  $dA$  to constrain the modeled reflectivity  $F(x)$  since either of the lower frequency channels serve as a “reference” reflectivity profile, with the obvious assumption that the reference profile is unattenuated. To retrieve rain rate, the algorithm would iterate over two parameters (slope and shape parameters, for example, if using two frequencies) such that:

$$X = ([\mu_1, \lambda_1], [\mu_2, \lambda_2], \dots, [\mu_N, \lambda_N])$$

Once the algorithm converges on a solution for the slope and shape parameters as in  $X$ , equations 1.1 and 1.3 could directly solve for  $N(D)$  and  $R$  respectively if a table for droplet fall velocities is provided [e.g. Gunn and Kinzer, 1949; Beard 1976].

Another avenue for improving the precipitation retrieval algorithm could involve the addition of a LWP integral constraint. The optical depth constraint provided by the RSP in this dissertation enabled a joint cloud and precipitation retrieval. A reliable optical depth product, such as the one provided by the RSP, is perhaps the best way to fully constrain and minimize uncertainty in CWP; however, optical depth offers no added benefit to reducing uncertainty in retrieved precipitation products. A robust LWP retrieval is possible from the 2016 AMPR dataset from ORACLES and from the entire CAMP2Ex campaign. A LWP constraint, compared to an optical depth constraint, offers an immense advantage by eliminating the uncertainty in CWP retrievals by assuming a homogeneous vs. linearly increasing CWC profile with altitude, which contributes approximately 20%

uncertainty to the final CWP product. The LWP retrieval from AMPR is far more sensitive to precipitation than the RSP, lending greater confidence to retrieved precipitation quantities. A LWP constraint in conjunction with a dual-frequency retrieval framework promises a dramatic reduction in cloud and precipitation retrieval uncertainties.

Inverse-modeled cloud and precipitation properties following the methods presented throughout this dissertation enable a direct validation of state-of-the-art Large-Eddy Simulation (LES) modeling. For the ORACLES experiment, Zhou et al. (2017) examined aerosol semi-direct and indirect effects related to the SE Atlantic StCu layer. Their study found that aerosol semi-direct effects substantially reduce total LWP, while precipitation suppression overcame the loss of CWP to entrainment. The collocated APR-3, HSRL-2, SSFR and RSP measurements all offer a means to validate the ORACLES-based LES case study. Additional studies from this ORACLES LES case study are presently ongoing, including this observation-model inter-comparison.

The methods presented in this dissertation also allow for the direct validation of similar spaceborne measured and retrieved data. The inverse methods described in Chapters 3 and 4 were direct adaptations of the operational 2C-RAIN-PROFILE algorithm (and 2C-PRECIP-COLUMN, to a lesser degree) for CloudSat. The adaptations for the ORACLES dataset centered mostly on using APR-3 specifications (i.e. narrower beamwidth, ~7km transit altitudes, etc.), and accounted for the APR-3's capabilities to see very thin, shallow StCu that CloudSat might otherwise be insensitive or blind to. Similarly, this adapted algorithm could be similarly

implemented for other field campaigns (e.g. CAMP2Ex, LPVEx, CSET, OTREC) measuring precipitation in distinct regions of the globe. This algorithm's broader applicability has great promise for validating CloudSat's precipitation retrieval algorithms under a wide variety of cloud types and environmental conditions.

Another avenue toward improving the results in this dissertation entails using a cloud classification scheme. EIS, a bulk measure of atmospheric stability and proxy for different cloud types, does not fully disentangle the different types of observed cloud types including open-cell versus closed-cell StCu. A distinct cloud classification scheme would eliminate possible contamination of results by, for example, 2-3 km thick cumulus clouds. Another benefit to implementing a cloud classification scheme is the ability to quantify other bulk properties such as spatial LWP variability and horizontal (geometric) cloud extent. This information could add important detail toward other aerosol-cloud effects, or even add important context or explanation for regional-scale evaporative cooling if the horizontal extent of clouds varies considerably between clean and polluted environmental regimes. Finally, a classification scheme could also prove important for validating EIS as a bulk measure as employed in this dissertation and in numerous previous studies.

Finally, at the time of this writing, a few active collaborative efforts remain ongoing related to this work. The in-situ cloud probe groups from ORACLES are using APR-3/2C-RAIN data as a secondary data source to investigate precipitation susceptibility. A number of conference presentations have been given on this topic, with preliminary results corroborating results presented in Chapter 4. An extension of the evaporation work presented in Chapter 5 will be explored further with the

isotopes group at Oregon State University, led by Dr. David Noone. The in-situ isotope measurements offer a secondary data source estimating the amount of evaporation occurring in the sub-cloud layer. These measurements would provide a constraint on the frequency of evaporation in virga and the magnitude of evaporation in surface precipitation, since evaporation was assumed everywhere a radar profile exceeded a -15 dBZ reflectivity threshold and the evaporation model used for surface precipitation has not been validated for ORACLES use. Finally, an active study on aerosol semi-direct and indirect effects along the 5°E flight track is ongoing with a group from the University of Miami. Routine flights in 2017 and 2018 sampled the 5°E longitude line from São Tomé to approximately 10-15°S.

## Chapter 7: Conclusions

The ORACLES dataset presented throughout this dissertation offers a unique and perhaps unprecedented window into cloud-aerosol-precipitation interactions and processes, whereby the work presented in this dissertation merely scratches the surface on this window.

The first step in this work involved the adaptation of the 2C-RAIN-PROFILE algorithm, a precipitation retrieval algorithm designed for CloudSat's CPR, to airborne W-band radar data. Numerous measurement strategies were employed throughout ORACLES, collecting W-band radar data at high sensitivity ( $-30$  dBZ or lower) and frequency (approximately every 0.05 seconds). These radar data, in conjunction with ECMWF ERA-I atmospheric state data, enabled the creation of the 2C-RAIN product: an extensive database of precipitation retrievals including RWP, surface precipitation rate and profiles of precipitation rate. Uncertainty estimates for the retrieved precipitation rate variables exhaustively account for all possible sources of error. This database was uploaded to NASA's ESPO Archive in September 2019.

Chapter 3 characterized cloud structure and precipitation statistics from 2C-RAIN. Surface precipitation fraction in 2016 was 34%, which was higher than the 13% estimated for 2017. Several flights during the 2016 campaign occurred near the African coast, where shallower MBLs prevailed thus resulting in numerous radar profiles extending entirely to the surface. The 2017 (and 2018) campaign, stationed in São Tomé, sampled a different part of the SE Atlantic basin. Estimated Inversion

Strength (EIS), a stability parameter used throughout this work, was much lower during the final two ORACLES campaigns and resulted in many more observations taken in unstable ( $EIS < 0$  K) environments. Cloud top heights in 2017, unsurprisingly, were on average a few hundred meters higher than those observed in 2016. The most frequent column reflectivity measurements were between -20 to -15 dBZ. The fraction of low (less than 0.01 mm/hr) surface precipitation rates in 2016 was suspected to be the result of more sampling taking place in highly stable ( $EIS > 6$  K) environments during 2016. The role of EIS on precipitation rate, henceforth, became a logical next path for investigation in Chapters 4 and 5.

To improve the 2C-RAIN dataset for addressing precipitation susceptibility-based science questions, RSP optical depth and effective radius data enabled CWP retrievals. Even though RSP data were somewhat limited in 2016, nearly 1.3 million collocated RSP and APR-3 profiles contained usable data for investigating cloud and precipitation characteristics.

In Chapter 1, the following questions were posed:

1. (SQ1) What are the retrieved precipitation rates from airborne radar, and how do environmental controls explain variations in these precipitation rates?
2. (SQ2) Using multiple airborne remote sensing datasets, is the presence of aerosol-induced precipitation suppression observed during ORACLES?
3. (SQ3) What are the relative roles of virga and surface precipitation on the local energy budget?

To answer SQ1, developing the 2C-RAIN product to include CWP, RWP and both surface and maximum column rain rates enabled investigation. Results from Chapter 3 suggested partitioning results by EIS would disentangle actual effects of aerosols on the underlying StCu deck from large-scale atmospheric processes. The gap definition in Chapter 4 allowed for the analysis of aerosol effects in “contact” versus “non-contact” scenarios (applicable to SQ2), with further partitioning limited by uncertainties in aerosol contact time [Diamond et al., 2018], lack of entrainment rate knowledge, and limited data in high EIS regimes (especially from 2016). The most conclusive result revealed a dramatic increase in CWP/RWP ratios in the presence of aerosols, with these ratios increasing with increasing stability. A surprising result was noted for unstable environments: the CWP/RWP ratios were similar, but *increases* in both CWP and RWP in contact with aerosols led to a statistically significant result between the contact and non-contact results. Statistical significance was not found for any scenario involving the sensitivity of precipitation rates to aerosol contact versus non-contact scenarios. Given the large uncertainties at the common retrieved precipitation rates (i.e. less than 0.5 mm/day) and the large variance of retrieved precipitation rates across all conditions, this result further motivates the need to reduce uncertainties in retrieved precipitation rates. The reduction in RWP and RR for stable environments, nonetheless, adds to the prevailing evidence that aerosols suppress precipitation.

To conclude this dissertation, each hypothesis from Chapter 1 is reiterated and summarized as follows:

1. The majority of retrieved precipitation rates from clouds observed during ORACLES will be less than 2 mm/day ( $\sim 0.1$  mm/hr) reflecting expected drizzling stratocumulus clouds, and with variability due to varying environmental conditions.

In Chapter 3, the majority of retrieved precipitation rates were indeed under  $\sim 0.1$  mm/hr. The different sampling environments between 2016 and 2017, indicated by larger average EIS during 2016 compared to 2017, likely resulted in the increased percentage of precipitation rates exceeding 0.1 mm/hr. This result was corroborated further in Chapter 4, where CWP and RWP also varied with EIS.

2. The presence of fine-mode aerosols produces a statistically-significant reduction in precipitation frequency and magnitude, given the large number of radar observations available in regions of the SE Atlantic Ocean that exhibit consistent (or relatively stagnant) environmental and meteorological conditions.

In Chapter 4, no statistically significant reduction in precipitation magnitude was found. CWP, RWP and the ratio of CWP/RWP between aerosol contact and non-contact scenarios, however, were statistically significant. The marked increase in the CWP/RWP ratio (nearly  $30 \text{ g m}^{-2}$  of CWP per unit of RWP) under stable regimes offers strong observational evidence of an increase in cloud lifetime. The reduction in RWP and precipitation rates from non-contact to contact scenarios in stable

regimes also offers some evidence (albeit inconclusive) that fine mode aerosols detected by the HSRL-2 have a measurable effect on precipitation rates.

3. Latent cooling from evaporating virga is greater than the latent cooling from evaporation by surface precipitation, given that virga occurs more frequently in these clouds.

Chapter 5 revealed, even though virga occurs more often than surface precipitation, latent cooling from surface precipitation is larger than the latent cooling from evaporating virga. While this hypothesis is technically rejected, the 2:1 ratio of latent cooling from virga to surface precipitation – which accounts for the broad scale of the StCu deck – still indicates that virga is an important contributor to the local latent heating budget. The latent cooling from evaporation implies that surface precipitation and virga each affect the vertical thermodynamic structure differently, likely leading to differences in vertical air motion and surface mixing.

## Acknowledgements

A portion of the work presented in this dissertation underwent several iterations of peer review or internal review by colleagues at UW-Madison and other institutions. Their contributions toward guiding and improving the quality of the data and science are greatly appreciated. I would like to properly acknowledge these persons.

The authors of the manuscript presented in Chapter 3 would like to thank Steve Durden, Elin McIlhattan, Greg Sadowy, Gregg Dobrowalski, William Chun, Raquel Rodriguez Monje, and Matt Lebsock for assisting with APR-3 data collection, hardware support and data processing. A portion of the research described in this paper was performed at the Jet Propulsion Laboratory, California Institute of Technology under contract with the National Aeronautics and Space Administration. The authors would also like to thank the ORACLES science team for multiple insightful discussions that led to the creation of the dataset described in this paper. Finally, the authors would like to thank Mikael Witte and two anonymous reviewers for their constructive and insightful comments that vastly improved the quality of the work presented in Chapter 3. All work presented in this dissertation was funded under NASA grant NNX15AF99G.

## Bibliography

- Abel, S. J. and Boutle, I. A., 2012: An improved representation of the raindrop size distribution for single-moment microphysics schemes. *Q.J.R. Meteorol. Soc.*, **138**, 2151–2162, doi:10.1002/qj.1949
- Abel, S. J. and Shipway, B. J., 2007: A comparison of cloud-resolving model simulations of trade wind cumulus with aircraft observations taken during RICO. *Q.J.R. Meteorol. Soc.*, **133**, 781-794. doi:10.1002/qj.55
- Adebiyi, A.A. and P. Zuidema, 2018: Low Cloud Cover Sensitivity to Biomass-Burning Aerosols and Meteorology over the Southeast Atlantic. *J. Climate*, **31**, 4329–4346, doi:10.1175/JCLI-D-17-0406.1
- Adebiyi, A.A. and Zuidema, P., 2016: The role of the southern African easterly jet in modifying the southeast Atlantic aerosol and cloud environments. *Q.J.R. Meteorol. Soc.*, **142**, 1574-1589. doi:10.1002/qj.2765
- Adebiyi, A.A., P. Zuidema, and S.J. Abel, 2015: The Convolution of Dynamics and Moisture with the Presence of Shortwave Absorbing Aerosols over the Southeast Atlantic. *J. Climate*, **28**, 1997–2024, doi:10.1175/JCLI-D-14-00352.1
- Agee, E.M. and K.E. Dowell, 1974: Observational Studies of Mesoscale Cellular Convection. *J. Appl. Meteor.*, **13**, 46–53, [https://doi.org/10.1175/1520-0450\(1974\)013<0046:OSOMCC>2.0.CO;2](https://doi.org/10.1175/1520-0450(1974)013<0046:OSOMCC>2.0.CO;2)
- Albrecht, B., V. Ghate, J. Mohrmann, R. Wood, P. Zuidema, C. Bretherton, C. Schwartz, E. Eloranta, S. Glienke, S. Donaher, M. Sarkar, J. McGibbon, A.D. Nugent, R.A. Shaw, J. Fugal, P. Minnis, R. Paliknoda, L. Lussier, J. Jensen, J. Vivekanandan, S. Ellis, P. Tsai, R. Rilling, J. Haggerty, T. Campos, M. Stell, M. Reeves, S. Beaton, J. Allison, G. Stossmeister, S. Hall, and S. Schmidt, 2018: Cloud System Evolution in the Trades—CSET Following the Evolution of Boundary Layer Cloud Systems with the NSF/NCAR GV. *Bull. Amer. Meteor. Soc.*, **100**, 93-121, doi:10.1175/BAMS-D-17-0180.1

- Albrecht, B.A., C.S. Bretherton, D. Johnson, W.H. Scubert, and A.S. Frisch, 1995: The Atlantic Stratocumulus Transition Experiment—ASTEX. *Bull. Amer. Meteor. Soc.*, **76**, 889–904, doi:10.1175/1520-0477(1995)076<0889:TASTE>2.0.CO;2
- Albrecht, B. A., Fairall, C. W., Thomson, D. W., White, A. B., Snider, J. B., and Schubert, W. H., 1990: Surface-based remote sensing of the observed and the adiabatic liquid water content of stratocumulus clouds. *Geophysical Research Letters*, **17**, 89-92, doi:10.1029/GL017i001p00089
- Albrecht, B. A., 1989: Aerosols, cloud microphysics, and fractional cloudiness. *Science*, **245**, 1227-1230, doi:10.1126/science.245.4923.1227
- Alexandrov, M. D., Cairns, B., Emde, C., Ackerman, A. S., and van Diedenhoven, B., 2012: Accuracy assessments of cloud droplet size retrievals from polarized reflectance measurements by the research scanning polarimeter. *Remote sensing of environment*, **125**, 92-111, doi: 10.1016/j.rse.2012.07.012
- Austin, P., Y. Wang, V. Kujala, and R. Pincus, 1995: Precipitation in Stratocumulus Clouds: Observational and Modeling Results. *J. Atmos. Sci.*, **52**, 2329–2352, doi:10.1175/1520-0469(1995)052<2329:PISCOA>2.0.CO;2
- Battaglia, A., Augustynek, T., Tanelli, S., and Kollias, P., 2011: Multiple scattering identification in spaceborne W-band radar measurements of deep convective cores, *J. Geophys. Res.*, **116**, D19201, doi:10.1029/2011JD016142
- Battaglia, A., and Simmer, C., 2008: How does multiple scattering affect the spaceborne W-band radar measurements at ranges close to and crossing the sea-surface range? *IEEE Transactions on Geoscience and Remote Sensing*, **46**, 1644-1651, doi:10.1109/TGRS.2008.916085
- Baumgartner, A., and Reichel, E., 1975: The world water balance: mean annual global, continental and maritime precipitation and run-off. *Elsevier*
- Beard, K. V., 1976: Terminal velocity and shape of cloud and precipitation drops aloft. *Journal of the Atmospheric Sciences*, **33**, 851-864, doi:10.1175/1520-0469(1976)033<0851:TVASOC>2.0.CO;2

- Bennartz, R., 2007: Global assessment of marine boundary layer cloud droplet number concentration from satellite, *J. Geophys. Res.*, **112**, D02201, doi:10.1029/2006JD007547
- Berg, W., T. L'Ecuyer, and J.M. Haynes, 2010: The Distribution of Rainfall over Oceans from Spaceborne Radars. *J. Appl. Meteor. Climatol.*, **49**, 535–543, doi:10.1175/2009JAMC2330.1
- Berg, W., T. L'Ecuyer, and C. Kummerow, 2006: Rainfall Climate Regimes: The Relationship of Regional TRMM Rainfall Biases to the Environment. *J. Appl. Meteor. Climatol.*, **45**, 434–454, doi:10.1175/JAM2331.1
- Bony, S., Schulz, H., Vial, J., and Stevens, B., 2020: Sugar, Gravel, Fish and Flowers: Dependence of Mesoscale Patterns of Trade-wind Clouds on Environmental Conditions. *Geophysical Research Letters*, **47**. doi:10.1029/2019GL085988
- Bony, S., and Dufresne, J.-L., 2005: Marine boundary layer clouds at the heart of tropical cloud feedback uncertainties in climate models, *Geophys. Res. Lett.*, **32**, L20806, doi:10.1029/2005GL023851
- Bretherton, C. S., Wood, R., George, R. C., Leon, D., Allen, G., and Zheng, X., 2010: Southeast Pacific stratocumulus clouds, precipitation and boundary layer structure sampled along 20° S during VOCALS-REx, *Atmos. Chem. Phys.*, **10**, 10639-10654, doi:10.5194/acp-10-10639-2010
- Bretherton, C.S., T. Uttal, C.W. Fairall, S.E. Yuter, R.A. Weller, D. Baumgardner, K. Comstock, R. Wood, and G.B. Raga, 2004: The Epic 2001 Stratocumulus Study. *Bull. Amer. Meteor. Soc.*, **85**, 967–978, doi:10.1175/BAMS-85-7-967
- Burton, S. P., Ferrare, R. A., Vaughan, M. A., Omar, A. H., Rogers, R. R., Hostetler, C. A., and Hair, J. W., 2013: Aerosol classification from airborne HSRL and comparisons with the CALIPSO vertical feature mask. *Atmospheric Measurement Techniques Discussions*, **6**, 1397-1412, doi:10.5194/amt-6-1397-2013
- Burton, S. P., Ferrare, R. A., Hostetler, C. A., Hair, J. W., Rogers, R. R., Obland, M. D., Butler, C. F., Cook, A. L., Harper, D. B., and Froyd, K. D., 2012: Aerosol classification using airborne High Spectral Resolution Lidar measurements – methodology and examples. *Atmos. Meas. Tech.*, **5**, 73–98, doi:10.5194/amt-5-73-2012

- Cairns, B., Russell, E. E., LaVeigne, J. D., and Tennant, P. M., 2003: Research scanning polarimeter and airborne usage for remote sensing of aerosols. *Proc. SPIE 5158, Polarization Science and Remote Sensing*, **5158**, 33-44, doi:10.1117/12.518320
- Chase, R. J., Finlon, J. A., Borque, P., McFarquhar, G. M., Nesbitt, S. W., Tanelli, S., et al., 2018: Evaluation of triple-frequency radar retrieval of snowfall properties using coincident airborne in situ observations during OLYMPEX. *Geophysical Research Letters*, **45**, 5752– 5760, doi:10.1029/2018GL077997
- Chowdhary, J., Cairns, B., Mishchenko, M., and Travis, L., 2001: Retrieval of aerosol properties over the ocean using multispectral and multiangle photopolarimetric measurements from the Research Scanning Polarimeter. *Geophysical research letters*, **28**, 243-246, doi:10.1029/2000GL011783
- Clothiaux, E. E., M. A. Miller, B. A. Albrecht, T. P. Ackerman, J. Verlinde, D. M. Babb, R. M. Peters, and W. J. Syrett, 1995: An evaluation of a 94-GHz radar for remote sensing of cloud properties. *J. Atmos. Oceanic Technol.*, **12**, 201–229, doi: 10.1175/1520-0426(1995)012<0201:AEOAGR>2.0.CO;2
- Comstock, K. K., Wood, R., Yuter, S. E. and Bretherton, C. S., 2004: Reflectivity and rain rate in and below drizzling stratocumulus. *Q.J.R. Meteorol. Soc.*, **130**, 2891-2918. doi:10.1256/qj.03.187
- Cox, S. K., McDougal, D. S., Randall, D. A., and Schiffer, R. A., 1987: FIRE—the first ISCCP regional experiment. *Bulletin of the American Meteorological Society*, **68**, 114-118
- Das, S., Harshvardhan, H., and Colarco, P. R., 2020: The influence of elevated smoke layers on stratocumulus clouds over the SE Atlantic in the NASA Goddard Earth Observing System (GEOS) model. *Journal of Geophysical Research: Atmospheres*, **125**, e2019JD031209, doi:10.1029/2019JD031209
- Deardorff, J.W., 1980: Cloud Top Entrainment Instability. *J. Atmos. Sci.*, **37**, 131 147, doi:10.1175/1520-0469(1980)037<0131:CTEI>2.0.CO;2

- Dee, D. P., Uppala, S. M., Simmons, A. J., Berrisford, P., Poli, P., Kobayashi, S., Andrae, U., Balmaseda, M. A., Balsamo, G., Bauer, P., Bechtold, P., Beljaars, A. C. M., van de Berg, L., Bidlot, J., Bormann, N., Delsol, C., Dragani, R., Fuentes, M., Geer, A. J., Haimberger, L., Healy, S. B., Hersbach, H., Hólm, E. V., Isaksen, L., Kållberg, P., Köhler, M., Matricardi, M., McNally, A. P., Monge-Sanz, B. M., Morcrette, J.-J., Park, B.-K., Peubey, C., de Rosnay, P., Tavolato, C., Thépaut, J.-N. and Vitart, F., 2011: The ERA-Interim reanalysis: configuration and performance of the data assimilation system. *Q.J.R. Meteorol. Soc.*, **137**, 553–597.  
doi:10.1002/qj.828
- Diamond, M. S., Dobracki, A., Freitag, S., Small Griswold, J. D., Heikkila, A., Howell, S. G., Kacarab, M. E., Podolske, J. R., Saide, P. E., and Wood, R., 2018: Time-dependent entrainment of smoke presents an observational challenge for assessing aerosol–cloud interactions over the southeast Atlantic Ocean, *Atmos. Chem. Phys.*, **18**, 14623–14636, doi:10.5194/acp-18-14623-2018
- Douglas, A. R. and L'Ecuyer, T., 2020: Observational evidence of aerosol-induced invigoration in warm, marine clouds, *in preparation*
- Douglas, A. R. and L'Ecuyer, T., 2019: Quantifying variations in shortwave aerosol cloud–radiation interactions using local meteorology and cloud state constraints, *Atmos. Chem. Phys.*, **19**, 6251–6268,  
<https://doi.org/10.5194/acp-19-6251-2019>
- Durden, S.L., Z.S. Haddad, A. Kitiyakara, and F.K. Li, 1998: Effects of Nonuniform Beam Filling on Rainfall Retrieval for the TRMM Precipitation Radar. *J. Atmos. Oceanic Technol.*, **15**, 635–646, doi:10.1175/1520-0426(1998)015<0635:EONBFO>2.0.CO;2
- Dzambo, A.M., T. L'Ecuyer, O.O. Sy, and S. Tanelli, 2019: The Observed Structure and Precipitation Characteristics of Southeast Atlantic Stratocumulus from Airborne Radar during ORACLES 2016–17. *J. Appl. Meteor. Climatol.*, **58**, 2197–2215, doi:10.1175/JAMC-D-19-0032.1
- Eastman, R., M. Lebsock, and R. Wood, 2019: Warm Rain Rates from AMSR-E 89-GHz Brightness Temperatures Trained Using CloudSat Rain-Rate Observations. *J. Atmos. Oceanic Technol.*, **36**, 1033–1051, doi:10.1175/JTECH-D-18-0185.1

- Elias, T. G., Cairns, B., and Chowdhary, J., 2004: Surface optical properties measured by the airborne research scanning polarimeter during the CLAMS experiment, *Proc. SPIE 5235, Remote Sensing of Clouds and the Atmosphere VIII*, **5235**, 595-606, doi:10.1117/12.514245
- Ellis, T. D., L'Ecuyer, T., Haynes, J. M., and Stephens, G. L., 2009: How often does it rain over the global oceans? The perspective from CloudSat. *Geophysical Research Letters*, **36**, L03815, doi:10.1029/2008GL036728
- Feingold, G., W.R. Cotton, B. Stevens, and A.S. Frisch, 1996a: The Relationship between Drop In-Cloud Residence Time and Drizzle Production in Numerically Simulated Stratocumulus Clouds. *J. Atmos. Sci.*, **53**, 1108–1122, doi:10.1175/1520-0469(1996)053<1108:TRBDIC>2.0.CO;2
- Feingold, G., Kreidenweis, S. M., Stevens, B., and Cotton, W. R., 1996b: Numerical simulations of stratocumulus processing of cloud condensation nuclei through collision-coalescence, *J. Geophys. Res.*, **101**, 21391– 21402, doi:10.1029/96JD01552
- Feingold, G., 1993: Parameterization of the evaporation of rainfall for use in general circulation models. *Journal of the atmospheric sciences*, **50**, 3454-3467, doi 10.1175/1520-0469(1993)050<3454:POTEOR>2.0.CO;2
- Fox, N.I. and A.J. Illingworth, 1997: The Potential of a Spaceborne Cloud Radar for the Detection of Stratocumulus Clouds. *J. Appl. Meteor.*, **36**, 676–687, doi:10.1175/1520-0450-36.6.676
- Gerber, H., 1996: Microphysics of Marine Stratocumulus Clouds with Two Drizzle Modes. *J. Atmos. Sci.*, **53**, 1649–1662, doi:10.1175/1520-0469(1996)053<1649:MOMSCW>2.0.CO;2
- Glienke, S., Kostinski, A., Fugal, J., Shaw, R. A., Borrmann, S., and Stith, J., 2017: Cloud droplets to drizzle: Contribution of transition drops to microphysical and optical properties of marine stratocumulus clouds, *Geophys. Res. Lett.*, **44**, 8002– 8010, doi:10.1002/2017GL074430
- Gunn, R., and G. D. Kinzer, 1949: The terminal velocity of fall for water droplets in stagnant air, *J. Atmos. Sci.*, **6**, 243–248

- Hair, J., Hostetler, C., Cook, A., Harper, D., Ferrare, R., Mack, T., Welch, W., Izquierdo, L., and F. Hovis, F., 2008: Airborne High Spectral Resolution Lidar for profiling aerosol optical properties, *Appl. Opt.*, **47**, 6734-6752, <https://doi.org/10.1364/AO.47.006734>
- Haynes, J. M., L'Ecuyer, T. S., Stephens, G. L., Miller, S. D., Mitrescu, C., Wood, N. B., and Tanelli, S., 2009: Rainfall retrieval over the ocean with spaceborne W band radar, *J. Geophys. Res.*, **114**, D00A22, doi:10.1029/2008JD009973
- Haywood, J. M., Osborne, S. R., Francis, P. N., Keil, A., Formenti, P., Andreae, M. O., and Kaye, P. H. 2003: The mean physical and optical properties of regional haze dominated by biomass burning aerosol measured from the C-130 aircraft during SAFARI 2000, *J. Geophys. Res.*, **108**, doi:10.1029/2002JD002226, D13
- Hilburn, K.A. and F.J. Wentz, 2008: Intercalibrated Passive Microwave Rain Products from the Unified Microwave Ocean Retrieval Algorithm (UMORA). *J. Appl. Meteor. Climatol.*, **47**, 778–794, doi:10.1175/2007JAMC1635.1
- Hitschfeld, W. and J. Borden, 1954: Errors inherent in the radar measurement of rainfall at attenuating wavelengths. *J. Meteor.*, **11**, 58–67, doi: 10.1175/1520-0469(1954)011<0058:EIITRM>2.0.CO;2
- Hogan, R.J. and A. Battaglia, 2008: Fast Lidar and Radar Multiple-Scattering Models. Part II: Wide-Angle Scattering Using the Time-Dependent Two-Stream Approximation. *J. Atmos. Sci.*, **65**, 3636–3651, doi:10.1175/2008JAS2643.1.
- Hou, P., Wu, S., McCarty, J. L., and Gao, Y., 2018: Sensitivity of atmospheric aerosol scavenging to precipitation intensity and frequency in the context of global climate change. *Atmospheric Chemistry and Physics*, **18**, 8173-8182, doi: 10.5194/acp-18-8173-2018
- Houze, R.A., L.A. McMurdie, W.A. Petersen, M.R. Schwaller, W. Baccus, J.D. Lundquist, C.F. Mass, B. Nijssen, S.A. Rutledge, D.R. Hudak, S. Tanelli, G.G. Mace, M.R. Poellot, D.P. Lettenmaier, J.P. Zagrodnik, A.K. Rowe, J.C. DeHart, L.E. Madaus, H.C. Barnes, and V. Chandrasekar, 2017: The Olympic Mountains Experiment (OLYMPEX). *Bull. Amer. Meteor. Soc.*, **98**, 2167–2188, doi:10.1175/BAMS-D-16-0182.1

- Houze, R.A., S.G. Geotis, F.D. Marks, D.D. Churchill, and P.H. Herzegh, 1981: Comparison of Airborne and Land-Based Radar Measurements of Precipitation during Winter MONEX. *J. Appl. Meteor.*, **20**, 772–783, doi:10.1175/1520-0450(1981)020<0772:COAALB>2.0.CO;2
- IPCC, 2014: Fifth Assessment Report. *Cambridge: Cambridge University Press*
- Jing, X., Suzuki, K., Guo, H., Goto, D., Ogura, T., Koshiro, T., & Mülmenstädt, J., 2017: A multimodel study on warm precipitation biases in global models compared to satellite observations. *Journal of Geophysical Research: Atmospheres*, **122**, 11,806–11,824, doi:10.1002/2017JD027310
- Kalmus, P., and Lebsock, M., 2017: Correcting biased evaporation in CloudSat warm rain. *IEEE Transactions on Geoscience and Remote Sensing*, **55**, 6207-6217, doi: 10.1109/TGRS.2017.2722469
- Kay, J. E., L'Ecuyer, T., Pendergrass, A., Chepfer, H., Guzman, R., and Yettella, V., 2018: Scale-aware and definition-aware evaluation of modeled near-surface precipitation frequency using CloudSat observations. *Journal of Geophysical Research: Atmospheres*, **123**, 4294–4309, doi:10.1002/2017JD028213
- Kazil, J., Yamaguchi, T., and Feingold, G., 2017: Mesoscale organization, entrainment, and the properties of a closed - cell stratocumulus cloud, *J. Adv. Model. Earth Syst.*, **9**, 2214-2229, doi:10.1002/2017MS001072
- Kiemle, C., Ehret, G., Kawa, S. R., and Browell, E. V., 2015: The global distribution of cloud gaps in CALIPSO data. *Journal of Quantitative Spectroscopy and Radiative Transfer*, **153**, 95-101, doi:10.1016/j.jqsrt.2014.12.001
- Klein, S.A. and D.L. Hartmann, 1993: The Seasonal Cycle of Low Stratiform Clouds. *J. Climate*, **6**, 1587–1606, [https://doi.org/10.1175/1520-0442\(1993\)006<1587:TSCOLS>2.0.CO;2](https://doi.org/10.1175/1520-0442(1993)006<1587:TSCOLS>2.0.CO;2)
- Kollias, P., Tselioudis, G., and Albrecht, B. A., 2007: Cloud climatology at the Southern Great Plains and the layer structure, drizzle, and atmospheric modes of continental stratus, *J. Geophys. Res.*, **112**, D09116, doi:10.1029/2006JD007307

- Koren, I., Dagan, G., and Altaratz, O. 2014: From aerosol-limited to invigoration of warm convective clouds. *science*, **344**, 1143-1146, doi:10.1126/science.1252595
- Lamb, D., and Verlinde, J., 2011: Physics and chemistry of clouds. *Cambridge University Press*, doi:10.1017/CBO9780511976377
- Lebsock, M.D., T.S. L'Ecuyer, and G.L. Stephens, 2011: Detecting the Ratio of Rain and Cloud Water in Low-Latitude Shallow Marine Clouds. *J. Appl. Meteor. Climatol.*, **50**, 419–432, doi:10.1175/2010JAMC2494.1
- Lebsock, M. D. and T. S. L'Ecuyer, 2011: The Retrieval of Warm Rain from CloudSat. *J. Geophys. Res.*, **116**, D20209, doi:10.1029/2011JD016076
- Lebsock, M. D., 2011: Level 2C RAIN-PROFILE Product Process Description and Interface Control Document, Algorithm version 0.0, *Retrieved online from* [http://www.cloudsat.cira.colostate.edu/sites/default/files/products/files/2C-RAIN-PROFILE-PDICD.P\\_R04.20110620.pdf](http://www.cloudsat.cira.colostate.edu/sites/default/files/products/files/2C-RAIN-PROFILE-PDICD.P_R04.20110620.pdf)
- Lebsock, M. D., G. L. Stephens, and C. Kummerow, 2008: Multisensor satellite observations of aerosol effects on warm clouds, *J. Geophys. Res.*, **113**, D15205, doi:10.1029/2008JD009876
- L'Ecuyer, T. S., W. Berg, J. Haynes, M. Lebsock, and T. Takemura, 2009: Global Observations of Aerosol Impacts on Precipitation Occurrence in Warm Maritime Clouds. *J. Geophys. Res.*, **114**, doi:10.1029/2008JD011273
- L'Ecuyer, T. S., and Stephens, G. L., 2002: An estimation-based precipitation retrieval algorithm for attenuating radars. *Journal of applied meteorology*, **41**, 272-285, doi:10.1175/1520-0450(2002)041<0272:AEBPRA>2.0.CO;2
- Leinonen, J., Lebsock, M. D., Tanelli, S., Sy, O. O., Dolan, B., Chase, R. J., Finlon, J. A., von Lerber, A., and Moisseev, D., 2018: Retrieval of snowflake microphysical properties from multifrequency radar observations. *Atmospheric Measurement Techniques*, **11**, 5471-5488, doi:10.5194/amt-11-5471-2018

- Lenschow, D. H., Paluch, I. R., Bandy, A. R., Pearson Jr, R., Kawa, S. R., Weaver, C. J., Huebert, B. J., Kay, J. G., Thornton, D. C., and Driedger III, A. R., 1988: Dynamics and chemistry of marine stratocumulus (DYCOMS) experiment. *Bulletin of the American Meteorological Society*, **69**, 1058-1067, doi:10.1175/BAMS-84-5-579
- Li, X. and R.C. Srivastava, 2001: An Analytical Solution for Raindrop Evaporation and Its Application to Radar Rainfall Measurements. *J. Appl. Meteor.*, **40**, 1607–1616, doi:10.1175/1520-0450(2001)040<1607:AASFRE>2.0.CO;2
- Liu, D., Liu, Q., and Zhou, L., 2015: Underestimation of oceanic warm cloud occurrences by the Cloud Profiling Radar aboard CloudSat. *Journal of Meteorological Research*, **29**, 576-593, doi:10.1007/s13351-015-5027-5
- Liu, Y., Geerts, B., Miller, M., Daum, P., and McGraw, R., 2008: Threshold radar reflectivity for drizzling clouds, *Geophys. Res. Lett.*, **35**, L03807, doi:10.1029/2007GL031201
- Lohmann, U., and Lesins, G., 2002: Stronger constraints on the anthropogenic indirect aerosol effect. *Science*, **298**, 1012-1015, <https://doi.org/10.1126/science.1075405>
- Lolli, S., P. Di Girolamo, B. Demoz, X. Li, and E.J. Welton, 2017: Rain Evaporation Rate Estimates from Dual-Wavelength Lidar Measurements and Intercomparison against a Model Analytical Solution. *J. Atmos. Oceanic Technol.*, **34**, 829–839, doi:10.1175/JTECH-D-16-0146.1
- Mace, G. G., and Abernathy, A. C. 2016: Observational evidence for aerosol invigoration in shallow cumulus downstream of Mount Kilauea, *Geophys. Res. Lett.*, **43**, 2981– 2988, doi:10.1002/2016GL067830
- Mace, G. G., Avey, S., Cooper, S., Lebsock, M., Tanelli, S., and Dobrowalski, G., 2016: Retrieving co-occurring cloud and precipitation properties of warm marine boundary layer clouds with A-Train data, *J. Geophys. Res. Atmos.*, **121**, 4008– 4033, doi:10.1002/2015JD023681
- Mace, G. G., and Sassen, K., 2000: A constrained algorithm for retrieval of stratocumulus cloud properties using solar radiation, microwave radiometer, and millimeter cloud radar data, *J. Geophys. Res.*, **105**, 29099–29108, doi:10.1029/2000JD900403

- Marchand, R., G.G. Mace, T. Ackerman, and G. Stephens, 2008: Hydrometeor Detection Using Cloudsat—An Earth-Orbiting 94-GHz Cloud Radar. *J. Atmos. Oceanic Technol.*, **25**, 519–533, doi:10.1175/2007JTECHA1006.1
- Marshall, J. S., and Palmer, W. M. K., 1948: The distribution of raindrops with size. *Journal of meteorology*, **5**, 165-166, doi:10.1175/15200469(1948)005<0165:TDORWS>2.0.CO;2
- Matheou, G., 2018: Turbulence structure in a stratocumulus cloud. *Atmosphere*, **9**, 392, doi:10.3390/atmos9100392
- Matrosov, S. Y., Uttal, T., and Hazen, D. A., 2004: Evaluation of radar reflectivity based estimates of water content in stratiform marine clouds. *Journal of Applied Meteorology*, **43**, 405-419, doi:10.1175/1520-0450(2004)043<0405:EOREO>2.0.CO;2
- Matus, A., T. S. L'Ecuyer, J. E. Kay, J.-F. Lamarque, and C. Hannay, 2015: The Role of Clouds in Modulating Global Aerosol Direct Radiative Effects in Spaceborne Active Observations and the Community Earth System Model. *J. Climate*, **28**, 2986-3003, doi:10.1175/JCLI-D-14-00426.1
- Merk, D., Deneke, H., Pospichal, B., and Seifert, P., 2016: Investigation of the adiabatic assumption for estimating cloud micro-and macrophysical properties from satellite and ground observations. *Atmos. Chem. Phys.*, **16**, 933-952, doi:10.5194/acp-16-933-2016
- Meyer, K., S. Platnick, and Z. Zhang, 2015: Simultaneously inferring above-cloud absorbing aerosol optical thickness and underlying liquid phase cloud optical and microphysical properties using MODIS. *J. Geophys. Res.*, **120**, 5524-5547, doi:10.1002/2015JD023128
- Mitrescu, C., S. D. Miller, J. M. Haynes, T. L'Ecuyer, and F. J. Turk, 2010: Toward a CloudSat Precipitation Profiling Algorithm - Model Description. *J. Appl. Meteor. And Climatol.*, **49**, 991-1003, doi:10.1175/2009JAMC2181.1
- Mohrmann, J., C.S. Bretherton, I.L. McCoy, J. McGibbon, R. Wood, V. Ghate, B. Albrecht, M. Sarkar, P. Zuidema, and R. Palikonda, 2019: Lagrangian Evolution of the Northeast Pacific Marine Boundary Layer Structure and Cloud during CSET. *Mon. Wea. Rev.*, **147**, 4681–4700, <https://doi.org/10.1175/MWR-D-190053.1>

- Mohrmann, J., Wood, R., McGibbon, J., Eastman, R., and Luke, E., 2018: Drivers of seasonal variability in marine boundary layer aerosol number concentration investigated using a steady state approach. *Journal of Geophysical Research: Atmospheres*, **123**, 1097–1112. doi:10.1002/2017JD027443
- Morrison, H., G. Thompson, and V. Tatarskii, 2009: Impact of Cloud Microphysics on the Development of Trailing Stratiform Precipitation in a Simulated Squall Line: Comparison of One- and Two-Moment Schemes. *Mon. Wea. Rev.*, **137**, 991–1007, doi:10.1175/2008MWR2556.1
- Mülmenstädt, J., and Feingold, G., 2018: The radiative forcing of aerosol–cloud interactions in liquid clouds: wrestling and embracing uncertainty. *Current Climate Change Reports*, **4**, 23-40, <https://doi.org/10.1007/s40641-018-0089-y>
- Munchak, S.J. and A. Tokay, 2008: Retrieval of Raindrop Size Distribution from Simulated Dual-Frequency Radar Measurements. *J. Appl. Meteor. Climatol.*, **47**, 223–239, doi:10.1175/2007JAMC1524.1
- Nakajima, T. and M.D. King, 1990: Determination of the Optical Thickness and Effective Particle Radius of Clouds from Reflected Solar Radiation Measurements. Part I: Theory. *J. Atmos. Sci.*, **47**, 1878–1893, doi:10.1175/1520-0469(1990)047<1878:DOTOTA>2.0.CO;2
- Nelson, E. L., and L'Ecuyer, T. S., 2018: Global character of latent heat release in oceanic warm rain systems. *Journal of Geophysical Research: Atmospheres*, **123**, 4797-4817, doi:10.1175/JTECH-D-15-0205.1
- Nelson, E.L., T.S. L'Ecuyer, S.M. Saleeby, W. Berg, S.R. Herbener, and S.C. van den Heever, 2016: Toward an Algorithm for Estimating Latent Heat Release in Warm Rain Systems. *J. Atmos. Oceanic Technol.*, **33**, 1309–1329, doi:10.1175/JTECH-D-15-0205.1
- Nuijens L., Emanuel K., Masunaga H., and L'Ecuyer T., 2017: Implications of Warm Rain in Shallow Cumulus and Congestus Clouds for Large-Scale Circulations. In: Pincus R., Winker D., Bony S., Stevens B. (eds) *Shallow Clouds, Water Vapor, Circulation, and Climate Sensitivity. Space Sciences Series of ISSI*, **65**, Springer, Cham, doi:10.1007/978-3-319-77273-8\_5

- Oreopoulos, L., Cho, N., and Lee, D. 2020: A global survey of apparent aerosol-cloud interaction signals. *Journal of Geophysical Research: Atmospheres*, **125**, doi:10.1029/2019JD031287
- Pennypacker, S., Diamond, M., and Wood, R., 2019: Ultra-clean and smoky marine boundary layers frequently occur in the same season over the southeast Atlantic, *Atmos. Chem. Phys. Discuss.*, doi:10.5194/acp-2019-628
- Peers, F., N. Bellouin, F. Waquet, F. Ducos, P. Goloub, J. Mollard, G. Myhre, R. B. Skeie, T. Takemura, D. Tanré, F. Thieuleux, and K. Zhang, 2016: Comparison of aerosol optical properties above clouds between POLDER and AeroCom models over the South East Atlantic Ocean during the fire season, *Geophys. Res. Lett.*, **43**, 3991-4000, doi:10.1002/2016GL068222
- Pincus, R., M.B. Baker, and C.S. Bretherton, 1997: What Controls Stratocumulus Radiative Properties? Lagrangian Observations of Cloud Evolution. *J. Atmos. Sci.*, **54**, 2215–2236, doi:10.1175/1520-0469(1997)054<2215:WCSRPL>2.0.CO;2
- Radke, L.F., P.V. Hobbs, and M.W. Eltgroth, 1980: Scavenging of Aerosol Particles by Precipitation. *J. Appl. Meteor.*, **19**, 715–722, doi:10.1175/1520-0450(1980)019<0715:SOAPBP>2.0.CO;2
- Ragette, G., and Wotawa, G., 1998: The evaporation of precipitation and its geographical distribution. *Physics and Chemistry of the Earth*, **23**, 393-397, doi:10.1016/S0079-1946(98)00043-3
- Ramanujam, S., Radhakrishnan, C., Subramani, D., and Chakravarthy, B., 2012: On the effect of non-raining parameters in retrieval of surface rain rate using TRMM PR and TMI measurements. *IEEE Journal of Selected Topics in Applied Earth Observations and Remote Sensing*, **5**, 735-743, doi:10.1109/JSTARS.2012.2189557

- Rauber, R.M., B. Stevens, H.T. Ochs, C. Knight, B.A. Albrecht, A.M. Blyth, C.W. Fairall, J.B. Jensen, S.G. Lasher-Trapp, O.L. Mayol-Bracero, G. Vali, J.R. Anderson, B.A. Baker, A.R. Bandy, E. Burnet, J. Brenguier, W.A. Brewer, P.R. Brown, R. Chuang, W.R. Cotton, L. Di Girolamo, B. Geerts, H. Gerber, S. Göke, L. Gomes, B.G. Heikes, J.G. Hudson, P. Kollias, R.R. Lawson, S.K. Krueger, D.H. Lenschow, L. Nuijens, D.W. O'Sullivan, R.A. Rilling, D.C. Rogers, A.P. Siebesma, E. Snodgrass, J.L. Stith, D.C. Thornton, S. Tucker, C.H. Twohy, and P. Zuidema, 2007: Rain in Shallow Cumulus Over the Ocean: The RICO Campaign. *Bull. Amer. Meteor. Soc.*, **88**, 1912–1928, doi:10.1175/BAMS-88-12-1912
- Redemann, J., and coauthors, 2020: An overview of the ORACLES (ObseRVations of Aerosols above CLouds and their intEractionS) project: aerosol-cloud radiation interactions in the Southeast Atlantic basin, *in preparation*
- Rodgers, C. D., 1976: Retrieval of atmospheric temperature and composition from remote measurements of thermal radiation, *Rev. Geophys.*, **14**, 609– 624, doi:10.1029/RG014i004p00609
- Salio, P., Hobouchian, M. P., Skabar, Y. G., and Vila, D. 2015: Evaluation of high resolution satellite precipitation estimates over southern South America using a dense rain gauge network. *Atmospheric Research*, **163**, 146-161, doi: 10.1016/j.atmosres.2014.11.017
- Sandu, I. and B. Stevens, 2011: On the Factors Modulating the Stratocumulus to Cumulus Transitions. *J. Atmos. Sci.*, **68**, 1865–1881, <https://doi.org/10.1175/2011JAS3614.1>
- Sarkar, M., P. Zuidema, B. Albrecht, V. Ghate, J. Jensen, J. Mohrmann, and R. Wood, 2020: Observations Pertaining to Precipitation within the Northeast Pacific Stratocumulus-to-Cumulus Transition. *Mon. Wea. Rev.*, **148**, 1251–1273, <https://doi.org/10.1175/MWR-D-19-0235.1>
- Sayer, A. M., N. C. Hsu, C. Bettenhausen, J. Lee, J. Redemann, B. Schmid, and Y. Shinozuka, 2016: Extending “Deep Blue” aerosol retrieval coverage to cases of absorbing aerosols above clouds: Sensitivity analysis and first case studies, *J. Geophys. Res. Atmos.*, **121**, 4830-4854, doi:10.1002/2015JD024729

- Schumacher, C. and R.A. Houze, 2003: Stratiform Rain in the Tropics as Seen by the TRMM Precipitation Radar. *J. Climate*, **16**, 1739–1756, doi:10.1175/1520-0442(2003)016<1739:SRITTA>2.0.CO;2
- Small, J. D., Chuang, P. Y., Feingold, G., and Jiang, H., 2009: Can aerosol decrease cloud lifetime? *Geophys. Res. Lett.*, **36**, L16806, doi:10.1029/2009GL038888
- Sorooshian, A., Feingold, G., Lebsock, M. D., Jiang, H., and Stephens, G. L. 2010: Deconstructing the precipitation susceptibility construct: Improving methodology for aerosol-cloud precipitation studies, *J. Geophys. Res.*, **115**, D17201, doi:10.1029/2009JD013426
- Sorooshian, A., G. Feingold, M. D. Lebsock, H. Jiang, and G. L. Stephens, 2009: On the precipitation susceptibility of clouds to aerosol perturbations, *Geophys. Res. Lett.*, **36**, L13803, doi:10.1029/2009GL038993
- Starr, D.O., 1987: A Cirrus-Cloud Experiment: Intensive Field Observations Planned for FIRE. *Bull. Amer. Meteor. Soc.*, **68**, 119–124, doi:10.1175/1520-0477(1987)068<0119:ACCEIF>2.0.CO;2
- Stenz, R., X. Dong, B. Xi, Z. Feng, and R.J. Kuligowski, 2016: Improving Satellite Quantitative Precipitation Estimation Using GOES-Retrieved Cloud Optical Depth. *J. Hydrometeor.* **17**, 557–570, doi:10.1175/JHM-D-15-0057.1
- Stephens, G., and coauthors, 2012: An update on Earth's energy balance in light of the latest global observations. *Nature Geosci*, **5**, 691–696, doi:10.1038/ngeo1580
- Stephens, G. L., T. L'Ecuyer, R. Forbes, A. Gettelmen, J.-C. Golaz, A. Bodas-Salcedo, K. Suzuki, P. Gabriel, and J. Haynes, 2010: Dreary state of precipitation in global models, *J. Geophys. Res.*, **115**, D24211, doi:10.1029/2010JD014532
- Stevens, B., and Feingold, G., 2009: Untangling aerosol effects on clouds and precipitation in a buffered system. *Nature*, **461**, 607, doi:10.1038/nature08281

- Stevens, B., D.H. Lenschow, G. Vali, H. Gerber, A. Bandy, B. Blomquist, J.-. Brenguier, C.S. Bretherton, F. Burnet, T. Campos, S. Chai, I. Faloona, D. Friesen, S. Haimov, K. Laursen, D.K. Lilly, S.M. Loehrer, S.P. Malinowski, B. Morley, M.D. Petters, D.C. Rogers, L. Russell, V. Savic-Jovcic, J.R. Snider, D. Straub, M.J. Szumowski, H. Takagi, D.C. Thornton, M. Tschudi, C. Twohy, M. Wetzel, and M.C. van Zanten, 2003: Dynamics and Chemistry of Marine Stratocumulus—DYCOMS-II. *Bull. Amer. Meteor. Soc.*, **84**, 579–594, doi:10.1175/BAMS-84-5-579
- Tanelli, S., Durden, S. L., Im, E., Pak, K. S., Reinke, D. G., Partain, P., Haynes, J. M., and Marchand, R. T., 2008: CloudSat's cloud profiling radar after two years in orbit: Performance, calibration, and processing. *IEEE Transactions on Geoscience and Remote Sensing*, **46**, 3560-3573, doi:10.1109/TGRS.2008.2002030
- Tanelli, S., Durden, S. L., and Im, E., 2006: Simultaneous measurements of Ku-and Ka band sea surface cross sections by an airborne radar. *IEEE Geoscience and remote sensing letters*, **3**, 359-363, doi:10.1109/LGRS.2006.872929
- Tanelli, S., E. Im, S.L. Durden, L. Facheris, D. Giuli, and E.A. Smith, 2004: Rainfall Doppler Velocity Measurements from Spaceborne Radar: Overcoming Nonuniform Beam-Filling Effects. *J. Atmos. Oceanic Technol.*, **21**, 27–44, doi:10.1175/1520-0426(2004)021<0027:RDVMFS>2.0.CO;2
- Travis, L. D., 1992: Remote sensing of aerosols with the earth-observing scanning polarimeter. *Proc. SPIE 5158, Polarization Science and Remote Sensing*, **1747**, 154-164, doi:10.1117/12.138823
- Trenberth, K. E., 2011: Changes in precipitation with climate change. *Climate Research*, **47**, 123-138, doi:10.3354/cr00953
- Twomey, S., 1977: The influence of pollution on the short wave albedo of clouds, *J. Atmos. Sci.*, **34**, 1149–1152, 1977
- vanZanten, M. C., et al., 2011: Controls on precipitation and cloudiness in simulations of trade-wind cumulus as observed during RICO, *J. Adv. Model. Earth Syst.*, **3**, M06001, doi:10.1029/2011MS000056
- Vaughan, W.W. and D.L. Johnson, 1994: Meteorological Satellites—The Very Early Years, Prior to Launch of TIROS-1. *Bull. Amer. Meteor. Soc.*, **75**, 2295–2302, doi:10.1175/1520-0477(1994)075<2295:MSVEYP>2.0.CO;2

- Wang, Y., You, Y., and Kulie, M., 2018: Global virga precipitation distribution derived from three spaceborne radars and its contribution to the false radiometer precipitation detection. *Geophysical Research Letters*, **45**, 4446–4455, doi:10.1029/2018GL077891
- Wang, H., Feingold, G., Wood, R., and Kazil, J., 2010: Modelling microphysical and meteorological controls on precipitation and cloud cellular structures in Southeast Pacific stratocumulus. *Atmospheric Chemistry and Physics*, **10**, 6347–6362, doi:10.5194/acp-10-6347-2010
- Wang, J., and Geerts, B., 2003: Identifying drizzle within marine stratus with W-band radar reflectivity. *Atmospheric research* **69**, 1–27, doi:10.1016/j.atmosres.2003.08.001
- Warren, S.G., R.M. Eastman, and C.J. Hahn, 2007: A Survey of Changes in Cloud Cover and Cloud Types over Land from Surface Observations, 1971–96. *J. Climate*, **20**, 717–738, doi:10.1175/JCLI4031.1
- Weinman, J.A., R. Meneghini, and K. Nakamura, 1990: Retrieval of Precipitation Profiles from Airborne Radar and Passive Radiometer Measurements: Comparison with Dual-Frequency Radar Measurements. *J. Appl. Meteor.*, **29**, 981–993, doi:10.1175/1520-0450(1990)029<0981:ROPPFA>2.0.CO;2
- Widger, W.K. and C.N. Touart, 1957: Utilization of Satellite Observations in Weather Analysis and Forecasting. *Bull. Amer. Meteor. Soc.*, **38**, 521–533, doi:10.1175/1520-0477-38.9.521
- Witte, M.K., H. Morrison, J.B. Jensen, A. Bansemer, and A. Gettelman, 2019: On the Covariability of Cloud and Rain Water as a Function of Length Scale. *J. Atmos. Sci.*, **76**, 2295–2308, doi:10.1175/JAS-D-19-0048.1
- Witte, M.K., Ayala, O., Wang, L.-P., Bott, A. and Chuang, P.Y., 2017: Estimating collision–coalescence rates from *in situ* observations of marine stratocumulus. *Q.J.R. Meteorol. Soc.*, **143**, 2755–2763. doi:10.1002/qj.3124

- Wood, R., O. K. T., Bretherton, C. S., Mohrmann, J., Albrecht, B. A., Zuidema, P., Ghate, V., Eloranta, E., Glienke, S., Shaw, R. A., Fugal, J., and Minnis, P., 2018: Ultraclean Layers and Optically Thin Clouds in the Stratocumulus-to-Cumulus Transition. Part I: Observations. *Journal of the Atmospheric Sciences*, **75**, 1631-1652, doi:10.1175/JAS-D-17-0213.1
- Wood, R., M. Wyant, C.S. Bretherton, J. Rémillard, P. Kollias, J. Fletcher, J. Stemmler, S. de Szoeki, S. Yuter, M. Miller, D. Mechem, G. Tselioudis, J.C. Chiu, J.A. Mann, E.J. O'Connor, R.J. Hogan, X. Dong, M. Miller, V. Ghate, A. Jefferson, Q. Min, P. Minnis, R. Palikonda, B. Albrecht, E. Luke, C. Hannay, and Y. Lin, 2015: Clouds, Aerosols, and Precipitation in the Marine Boundary Layer: An Arm Mobile Facility Deployment. *Bull. Amer. Meteor. Soc.*, **96**, 419–440, doi:10.1175/BAMS-D-13-00180.1
- Wood, R., 2012: Stratocumulus Clouds. *Mon. Wea. Rev.*, **140**, 2373-2423, <https://doi.org/10.1175/MWR-D-11-00121.1>
- Wood, R., Mechoso, C. R., Bretherton, C. S., Weller, R. A., Huebert, B., Straneo, F., Albrecht, B. A., Coe, H., Allen, G., Vaughan, G., Daum, P., Fairall, C., Chand, D., Gallardo Klenner, L., Garreaud, R., Grados, C., Covert, D. S., Bates, T. S., Krejci, R., Russell, L. M., de Szoeki, S., Brewer, A., Yuter, S. E., Springston, S. R., Chaigneau, A., Toniazzo, T., Minnis, P., Palikonda, R., Abel, S. J., Brown, W. O. J., Williams, S., Fochesatto, J., Brioude, J., and Bower, K. N., 2011: The VAMOS Ocean-Cloud-Atmosphere-Land Study Regional Experiment (VOCALS-REx): goals, platforms, and field operations, *Atmos. Chem. Phys.*, **11**, 627-654, doi:10.5194/acp-11-627-2011
- Wood, R., 2007: Cancellation of Aerosol Indirect Effects in Marine Stratocumulus through Cloud Thinning. *J. Atmos. Sci.*, **64**, 2657–2669, <https://doi.org/10.1175/JAS3942.1>
- Wood, R., 2006: Rate of loss of cloud droplets by coalescence in warm clouds, *J. Geophys. Res.*, **111**, D21205, doi:10.1029/2006JD007553
- Wood, R. and C.S. Bretherton, 2006: On the Relationship between Stratiform Low Cloud Cover and Lower-Tropospheric Stability. *J. Climate*, **19**, 6425–6432, doi:10.1175/JCLI3988.1

- Wood, R. and D.L. Hartmann, 2006: Spatial Variability of Liquid Water Path in Marine Low Cloud: The Importance of Mesoscale Cellular Convection. *J. Climate*, **19**, 1748–1764, doi:10.1175/JCLI3702.1
- Wood, R., C. S. Bretherton, and D. L. Hartmann, 2002: Diurnal cycle of liquid water path over the subtropical and tropical oceans, *Geophys. Res. Lett.*, **29**, 2092, doi:10.1029/2002GL015371
- Xue, H., G. Feingold, and B. Stevens, 2008: Aerosol Effects on Clouds, Precipitation, and the Organization of Shallow Cumulus Convection. *J. Atmos. Sci.*, **65**, 392–406, doi:10.1175/2007JAS2428.1
- Yamaguchi, T., G. Feingold, J. Kazil, and A. McComiskey, 2015: Stratocumulus to cumulus transition in the presence of elevated smoke layers, *Geophys. Res. Lett.*, **42**, 10,478–10,485, doi:10.1002/2015GL066544
- Yang, F., Luke, E. P., Kollias, P., Kostinski, A. B., and Vogelmann, A. M., 2018: Scaling of drizzle virga depth with cloud thickness for marine stratocumulus clouds. *Geophysical Research Letters*, **45**, 3746– 3753, doi:10.1029/2018GL077145
- Zhang, S., Wang, M., Ghan, S. J., Ding, A., Wang, H., Zhang, K., Neubauer, D., Lohmann, U., Ferrachat, S., Takeamura, T., Gettelman, A., Morrison, H., Lee, Y., Shindell, D. T., Partridge, D. G., Stier, P., Kipling, Z., and Fu, C.: On the characteristics of aerosol indirect effect based on dynamic regimes in global climate models, *Atmos. Chem. Phys.*, **16**, 2765–2783, doi:10.5194/acp-16-2765-2016, 2016
- Zhang, L., Michelangeli, D. V., and Taylor, P. A., 2004: Numerical studies of aerosol scavenging by low-level, warm stratiform clouds and precipitation. *Atmospheric Environment*, **38**, 4653–4665, doi:10.1016/j.atmosenv.2004.05.042
- Zhou, X., and Bretherton, C. S., 2019: The correlation of mesoscale humidity anomalies with mesoscale organization of marine stratocumulus from observations over the ARM Eastern North Atlantic site. *Journal of Geophysical Research: Atmospheres*, **124**, doi: 10.1029/2019JD031056

Zhou, X., Ackerman, A. S., Fridlind, A. M., Wood, R., and Kollias, P., 2017: Impacts of solar absorbing aerosol layers on the transition of stratocumulus to trade cumulus clouds, *Atmos. Chem. Phys.*, **17**, 12725–12742, doi:10.5194/acp-17-12725-2017, 2017

Zuidema, P., J. Redemann, J. Haywood, R. Wood, S. Piketh, M. Hipondoka, and P. Formenti, 2016: Smoke and Clouds above the Southeast Atlantic: Upcoming Field Campaigns Probe Absorbing Aerosol's Impact on Climate. *Bull. Amer. Meteor. Soc.*, **97**, 1131–1135, doi:10.1175/BAMS-D-15-00082.1